Development of 3D *in vitro* Interaction Models for the Evaluation and Treatment of Brain Metastases

Shannon Sherwin Moreino

This thesis is submitted in partial fulfilment of the requirements for the degree of Master in Biomedical Sciences

Department of Biomedicine

University of Bergen

Spring 2021

Acknowledgements

Cardinally, I would like to express how grateful I am to God Almighty for keeping me and my loved ones in good health and giving me the strength to stay on course with my ambitions through all hardships. It is with His blessings and mercy that I am able to have come this far today.

I would like to express my immense gratitude to my supervisor Professor Frits Alan Thorsen for giving me the opportunity to join his research group and broadening my paradigms on the joys of being a scientific researcher. The realization and outcome of this paper would not have been possible without your unerring guidance and support. Thank you for always making the time to answer my questions and reminding me of the eloquence of brevity in thought and writing. Your vast intellect and insight has always intrigued me and I hope to get the chance to continue working with you in the future.

I would like to express my deep gratitude to my research group at Thorsen Lab, a group I consider myself very lucky to be part of. First and foremost, thank you Emma – your research guidance, encouragement and advice was crucial in my experiment planning and execution. Our little conversations on hectic lab days helped me more than you will ever know. Thank you also to Erlend, Tobias and Trond Are for the delightful conversations and scientific discussions in and out of the lab.

I would like to thank Halala and Aurea of the Translational Cancer Research group, who have been so helpful, supportive and caring to me through the year. My appreciation also goes to all the core facility personnel who helped me with instrumental experiments. Thank you to Endy Spriet and Hege Avsnes Dale for help with the Incucyte and the Dragonfly, and for dealing with the plethora of questions I sent your way.

I would like to thank my fellow colleagues and senior researchers from all around the world for providing me their excellent scientific insight and suggestions throughout the manifestation of this thesis. A special thanks to Edoardo Mandolini, Ivan Rios Mondragon, Muntequa Ishtiaq Siraji and Aishwariya Pavithram for their support and advice.

Lastly, I would like to thank my family and my amazing friends in Bergen who have helped me stay motivated through various stages of my thesis. Their love has constantly reminded me that, in the words of the poet Robert Frost:

"The woods are lovely, dark and deep
But I have promises to keep
And miles to go before I sleep."

Bergen, May 2021

Shannon Sherwin Moreino

Table of contents

List of Abbreviations

Abbreviation	Full Name
2D	Two dimensional
3D	Three dimensional
AKT	Protein kinase B
APC	Adenomatous polyposis coli
BBB	Blood brain barrier
BM	Brain metastases
BME	Brain microenvironment
BRAF	B-Raf proto-oncogene, a serine/threonine kinase
BTB	Blood tumor barrier
CK1	Casein kinase 1
c-MYC	Cellular myelocytomatosis
CNS	Central nervous system
CSD	Cumulative sun damage
CTLA-4	Cytotoxic T lymphocyte-associated protein 4
DNA	Deoxyribonucleic acid
DVL	Dishvelled
ECM	Extracellular matrix
EMT	Epithelial to mesenchymal transition
ERK	Extracellular signal-regulated kinases
EV	Extracellular vesicle
FAK	Focal adhesion kinase
FAP	Fibroblast activation protein
FDA	Food and Drug Administration
FITC	Fluorescein isothiocyanate
FOXO1	Forkhead box protein O1
FRP	Frizzled
GDP	Guanosine diphosphate
GFP	Green fluorescent protein
GSK3β	Glycogen synthase kinase 3 beta
GTP	Guanosine-5'-triphosphate
HPSE1	Heparanase 1
LRP	Low density lipoprotein receptor–related protein
LST1	Leukocyte specific transcript 1
MAPK	Mitogen-activated protein kinase
MBM	Melanoma brain metastases
MEK	Mitogen-activated protein kinase kinase
miRNA	Micro ribonucleic acid
MMP	Matrix metalloproteinase
mRNA	Messenger ribonucleic acid
mTORC1	Mammalian target of rapamycin complex 1
mTORC2	Mammalian target of rapamycin complex 2
NCBI	National Center for Biotechnology Information
NF1	Neurofibromin 1

NHA	Normal human astrocytes
NRAS	Neuroblastoma Ras viral oncogene homolog
ORR	Overall response rate
OS	Overall survival
p53	Tumor protein p53
PC12	Pheochromocytoma
PD1	Programmed cell death 1
PDQ	Physician Data Query
PFA	Paraformaldehyde
PFS	Progression free survival
PI3K	Phosphatidylinositol-3-kinase
PIP2	Phosphatidylinositol 4,5-bisphosphate
PIP3	Phosphatidylinositol (3,4,5)-trisphosphate
PTEN	Phosphatase and tensin homolog
RAF	Rapidly accelerated fibrosarcoma protein
RAS	Rat sarcoma
RFP	Red fluorescent protein
RNA	Ribonucleic acid
ROS	Reactive oxygen species
RTK	Receptor tyrosine kinase
SEM	Scanning electron microscopy
SRS	Stereotactic radiosurgery
TEER	Transepithelial electric resistance
TMs	Tumor microtubes
TNM	Tumor node-metastasis
TNTs	Tunneling nanotubules
TSC1/2	Tuberous sclerosis complex 1/2
UVR	Ultraviolet radiation
VEGF	Vascular-endothelial growth factor
WBRT	Whole brain radiotherapy
WHO	World Health Organization
WNT	Wingless/Integrated
ZEB1	Zinc finger E-box-binding homeobox 1
ZO1	Zonula occludens protein 1

Summary

Norway possesses the highest melanoma mortality rates in Europe, with the country experiencing a rapid increase in incidence rates since the turn of the century. Melanoma occurs due to a malignant transformation of melanin synthesizing cells known as melanocytes, and is the deadliest form of skin cancer. Malignant melanoma displays one of the highest propensities to metastasize to the brain, and the resulting melanoma brain metastases (MBM) has a staggeringly poor prognosis, regardless of contemporary treatment strategies.

Novel treatment design is strongly focused on integrating information of brain microenvironment directed influence on MBM development, in association with that of the melanoma metastatic cascade process. The emergence of 3D *in vitro* models which incorporate patient derived tissues/cells and enable longitudinal measurements have provided great promise in catalyzing this integration process while reducing the dependence on animal experimentation. The discovery of nanotube-mediated membrane continuity, termed as tunneling nanotubules (TNTs), by the late Hans-Hermann Gerdes (may he RIP) has shifted the paradigm of conventional cellular crosstalk and has opened the floodgates on research investigating how these structures mediate tumor progression and survival. Furthermore, the existence of the blood brain barrier (BBB) represents a major obstacle for the delivery of anticancer drugs to treat BM in the central nervous system (CNS) and may even contribute to tumor invasiveness and migration. The main aim of this thesis was to develop *in vitro* 3D model systems to be used for studying interactions between MBM and the brain metastatic niche.

In this thesis, we reported, for the first time, visual evidence and characterization of TNT interactions between MBM and normal human astrocytes (NHA) of the brain microenvironment. We achieved this through our establishment of an *in vitro* 3D TNT interaction model that can be used ideally from 8 to 32h to study TNT interactions between MBM and NHA. Our findings also indicated the use of TNT interactions by MBM cell lines to promote treatment resistance and cell survival. Furthermore, we established an *in vitro* 3D BBB model that can be used ideally for a period of 72h to assess BBB migration of MBM at a cell seeding density range of 5×10^3 -5×10^4 cells.

1. Introduction

1.1 Understanding Melanoma

Melanoma is a potentially fatal skin cancer that arises in melanocytes, which are specialized skin cells responsible for producing the protective skin pigment melanin **(Figure 1.1)**. The patient prognosis is very good at the early localized stages but a sharp decrease in survival rate is seen once patients get diagnosed with advanced or metastatic state of the disease [1]. It is holistically distinguished based on the site of its presentation as cutaneous or non-cutaneous melanoma. Cutaneous melanoma is subclassified depending on its clinical and histological presentation [2]. Although not as common, the development of melanoma can also occur at non cutaneous regions of the body, including genitourinary, gastrointestinal, nasopharyngeal and ocular sites. While melanoma accounts for only 1 percent of all skin cancers, the disease is responsible for around 73% of all skin cancer related deaths [3].

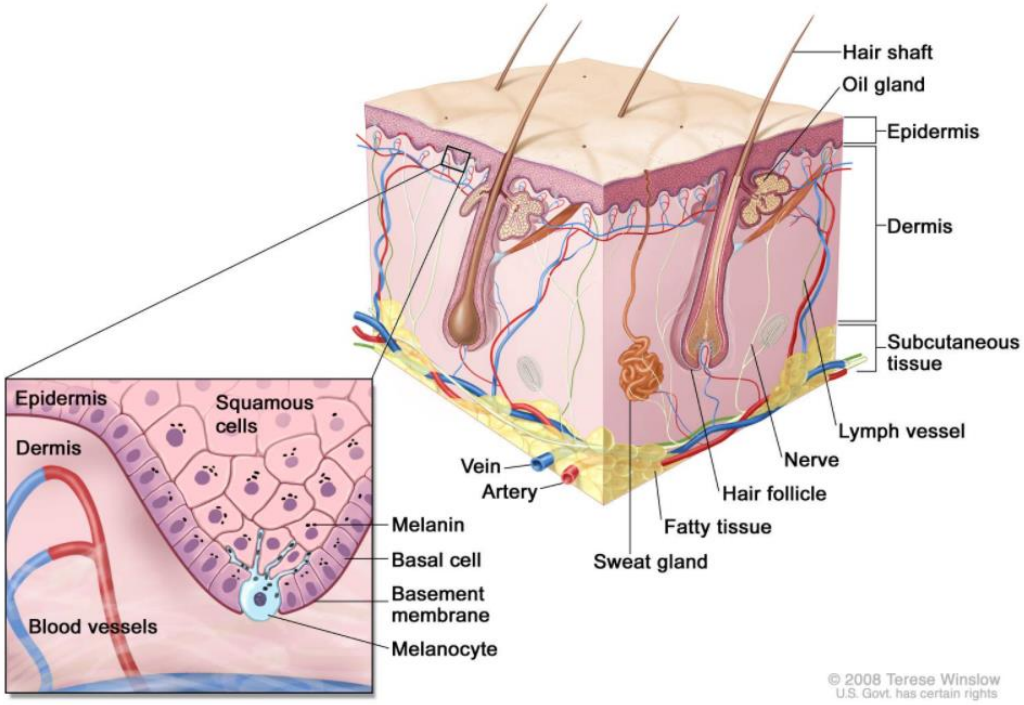

Figure 1.1 Composition of normal layers of the skin, location of major structures and cells. Figure taken from PDQ Cancer Information Summaries - NCBI [4]

1.2 Epidemiology, Incidence and Survival

The incidence of melanoma has risen at a faster rate than almost any other cancer during the last 50 years [5–7]. According to the 2020 Melanoma Skin Cancer Report by the Global Coalition for

Melanoma Patient Advocacy, Norway possesses the second highest incidence rate per capita globally (1 in 1983 per capita squared)[8], and remains as the highest in Europe (29.6 cases per 100,000 people)[9]. The risk of getting melanoma increases with age. It is very rare for someone to get this cancer before puberty, but melanoma is the second most common cancer in the age group 25-49 years, both among men and women. There were 32 women and 12 men who were diagnosed with melanoma before the age of 30 in 2019.

This trend has been reflected in the increase of skin melanoma rates in both genders (16.9% in men and 12.9% in women) within the last 6 years [10]. Furthermore, incidence rates are most pronounced in the oldest age groups (70 years and above) and speculated to be prevalent in populations of higher socioeconomic status and adverse suntanning tendencies[10]. Melanomas possess high propensities to metastasize to the brain [11] and remain one of the most recurrent intracranial tumors in adults [12]. Brain metastases (BM) are a common complication in patients with cutaneous melanoma. If BM is left untreated, the median overall survival (OS) rate is less than 6 months [13]. **Figure 1.2** shows the incidence rates of skin melanoma cases in males and females of Norway in the period of 1990-2020**.**

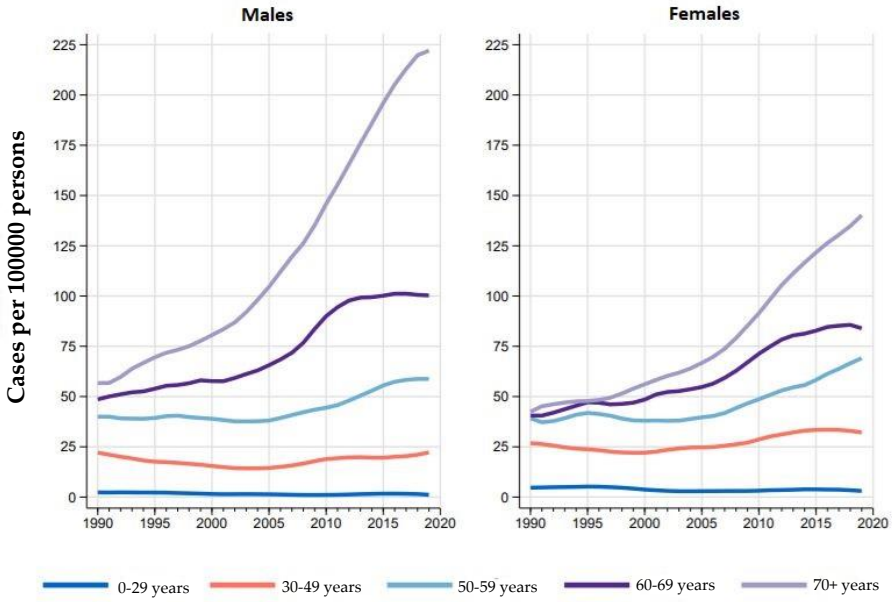

Figure 1.2 – Incidence rates of melanoma of the skin: Data shown are from Norway in the period of 1990 – 2020. Incidence graphs correspond to the left y-axis (rates per 100 000). Graphs are from the Cancer Registry of Norway 2020 [10]

1.3 Etiology and Risk Factors

Melanoma is regarded as a multifactorial cancer, owing to the variety of risk factors implicating it. The rise in melanoma incidence has been linked to the increase in use of tanning beds, increase in sun exposure and deterioration of the protective ozone layer [3,14]. The major risk factors of melanoma are either exogenous (externally or environmentally related) or endogenous (internally or genetically related) factors. Exogenous factors are easier to modify through changes in lifestyle, while endogenous factors are inherent patient characteristics, and therefore less modifiable **(Table 1.1)**.

Table 1.1 Summary of exogenous and endogenous risk factors of melanoma

Risk factors	
Exogenous	**Endogenous**
Indoor tanning [15–17]	Genetics [18–20]
Ultraviolet exposure [21–23]	Family history [24,25]
Medications [26,27]	Socioeconomic status [28–30]
Welding [31–33]	Nevi [34–36]
Smoking [37–39]	Ethnicity [40–42]
	Age [43–45]
	Gender [46–48]
	Site of presentation [49–51]
	Immunosuppression [52–54]

Ultraviolet (UV) radiation transmitted at various wavelengths exhibit a range of transmission into the skin layers [55]. UVC (200-290 nm in wavelength) is incapable of penetrating past the superficial skin layer, UVB (290-320 nm in wavelength) reaches the basal layer of the skin epidermis and UVA (320-380 nm in wavelength) exhibits the greatest degree of transmission through penetration of the dermis layer. Among these three types, UVB demonstrates high carcinogenicity and promotes the metabolization of specific photoproducts such as cyclobutane pyrimidine dimers and pyrimidine pyrimidone photoproducts [56]. Up to 65% of melanoma cases are linked with exposure to sunlight [57]. A history of sunburn, especially from an early age, has also been indicated to increase the risk of the disease [58]. Studies have also shown a correlation between melanoma and non-accustomed exposure to sun. This may provide an explanation for the high number of cases in countries with pale skinned populace and less sunlight, such as in Norway and Sweden [59,60].

Other risk factors for developing melanoma include skin paleness, red or blond pigmentation in hair, the tendency to tan poorly and the amount of freckles [61]. The acquiring of nevi (colloquially known as moles) has also been recognized as a risk factor, in individuals possessing a) more than 50 acquired nevi b) over five dysplastic nevi c) nevi > 6 mm or d) large congenital nevi. The formation of nevi can also occur as a result of sun exposure and serves as an indicator of the effect of UV radiation [57,62]. 8 – 12% of melanomas occur as a result of inherited genetics, 41% of which cases are due to mutations in the genes for cell cycle regulation, particularly in the p16 pathway [63]. Less frequent risk factors include immunosuppression, scar formation, exposure to chemicals and Marjolin's ulcer [64].

1.4 Classification, Grading and Staging

Melanoma was recently classified by WHO into three classes based on the mutagenic changes that arise in their formation – a) melanomas etiologically related to cumulative sun damage (CSD), b) melanomas caused by other factors and c) melanomas of a nodular nature [65]. Melanomas associated with CSD include those which are spreading superficially, desmoplastic melanomas and lentigo maligna. Among these subtypes, superficially spreading melanoma is the most recognized for its early radial growth followed by vertical growth and subsequent entry into the dermis [66]. Melanomas not caused by CSD are also subclassified into acral, mucosal, uveal, spitzoid and melanomas originating from congenital and blue nevi. Nodular melanoma is characterized by its early proliferation vertically downwards into the skin [66].

Grading is used to describe the morphological characteristics of the melanoma cells and the degree of abnormality. **Table 1.2** below provides a general grading system for melanoma.

Table 1.2 General grading system for melanoma [67]

Grading	**Description**
G1	Well differentiated, look like normal cells. Low grade
G2	Moderately differentiated, look partially abnormal. Moderate grade.
G3	Poorly differentiated and are abnormal. High grade.
G4	Undifferentiated, extremely abnormal. High grade.

Staging represents the size of the primary tumor as well as the degree of spread within the body of the patient [68]. The staging of melanoma is determined by the degree of thickness, ulceration and spread of the disease to lymph nodes and distal regions of the body [69]. This information plays a major role in determining a patient's prognosis upon time of diagnosis. It has been reported that survival rates are negatively affected by progression in tumor thickness and disease stage [70,71]. The general staging of cutaneous melanoma is illustrated in **Figure 1.3** below.

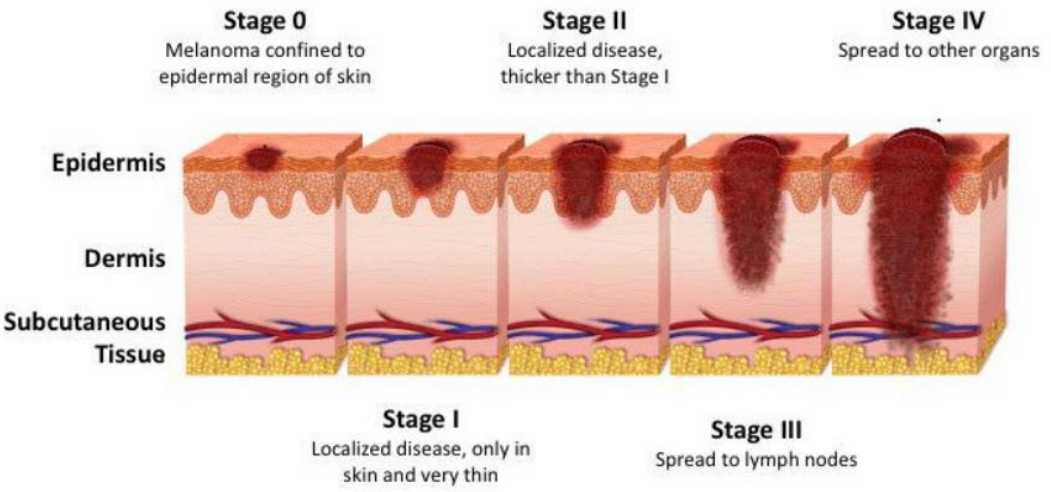

Figure 1.3 Stages of cutaneous melanoma and corresponding degree of carcinogenesis [72]

Melanoma staging utilizes a tumor node-metastasis (TNM) system which differentiates tumors based on tumor thickness within the skin, number of distant metastases and frequency of metastatic nodes (**Table 1.3**). Stage 4 melanoma is the most lethal, with metastatic spread to multiple organs of the body (including the brain, liver and lungs) [73].

Table 1.3 Melanoma staging and corresponding 5 year survival [74]**.**

Stage	**Description**	**5 Year Survival**
Stage 0	Melanoma *in situ*. Abnormal neoplasm confined to epidermis.	-
Stage I	Melanoma confined to the skin. Thickness of <1 mm^2. Can be ulcerated (skin covering is broken open) or not.	92-97%.
Stage II	Melanoma is ulcerated, but not spreading. Thickness is from 1.01 mm to 4.0 mm.	53-81%.
Stage III	Melanoma has metastasized to either one or more lymph	40-78%.

	nodes, or nearby skin.	
Stage IV	Melanoma has spread to internal organs, distant lymph nodes, or distant skin.	15-20%.

1.5 Biological Characteristics

Melanocytic neoplasms usually range from benign lesions (melanocytic nevi) to their malignant counterparts (melanoma). They are primary situated in the epidermal-dermal junction of the skin and produce melanin. Mammalian melanin is distinguished into two groups based on color – eumelanin (brown black) and pheomelanin (yellow red) [75]. Melanin (predominantly eumelanin) shields the skin from UVR by absorbing and redistributing UV energy and protecting genetic material present in the nuclei [76]. Around 50-75% of UVR is absorbed by melanin [76], which reduces damage on the skin caused by sunburn [77], prevents abnormal thermoregulation [78] and minimizes tissue injury caused by reactive oxygen species (ROS) [79].

1.6 Molecular Characteristics

At the cellular level, cancer cells possess various "hallmarks" which enable them to, among others, evade apoptosis, grow limitlessly without growth factors, promote angiogenesis and metastasize [80]. These specific molecular advantages are critical to understand for the development of more targeted, personalized and robust therapies and consequentially, improved patient prognoses [81]. Genetic mutations termed as "driver mutations" play a major role in inducing advantageous mutations which promote cellular proliferation and survival. Driver mutations act on tumor suppressor genes (responsible for regulating cell replication and division) and proto-oncogenes (contributes to cell growth) to promote genetic instability. This sets off a chaotic cascade promoting further mutations, unregulated cell growth and sustained tumorigenesis. Melanoma possesses the highest mutation frequency among all recorded cancers [82,83], and its pathophysiology incorporates several gene signaling pathways which promote disease growth and proliferation. The following subsections expound the three most crucial oncogenic signaling pathways implicated in the pathogenesis of melanoma **(Figure 1.4)**.

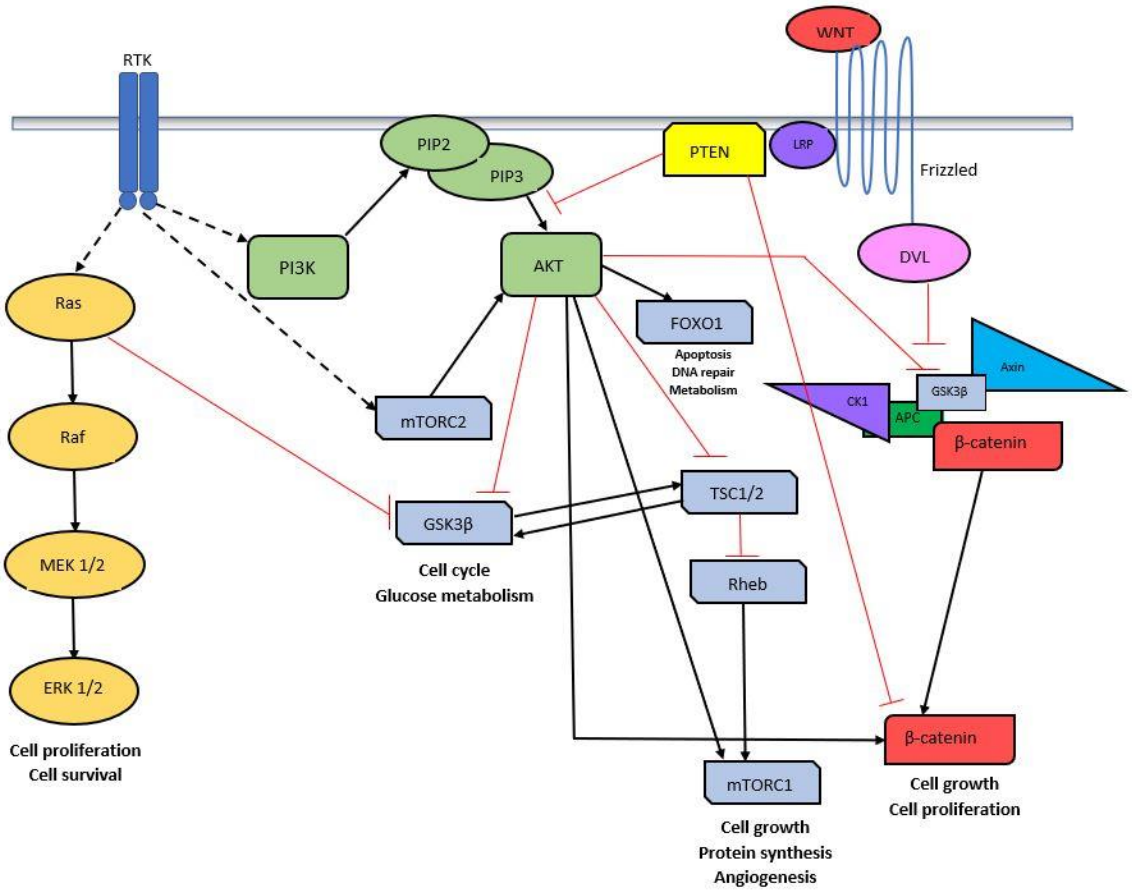

Figure 1.4 Overview of the three major pathways exploited by the melanoma metastatic process - Ras/MAPK, PI3K/AKT and WNT signaling pathways, as well as crosstalk between pathways. *Ras/MAPK pathway*: Ligand binding activation of receptor tyrosine kinase (RTK) promotes the activation of small GTPase Ras which then promotes the signal across the MAPK proteins (Raf, MEK 1/2 and ERK 1/2) which results in nuclear transcription of cell proliferation and survival genes. *PI3K/Akt pathway*: Activation of the AKT pathway through RTK ligand binding initiates PI3K proteins to promote the conversion of PIP2 to PIP3, which enables phosphorylation of protein kinase B (Akt). AKT signaling regulates numerous pathways, namely GSK3β production in cell cycle and glucose metabolism processes, mTORC1 in cell growth, protein synthesis and angiogenesis and FOXO1 proteins in apoptosis, DNA repair processes and cell metabolism. The ligand activated release of mTORC2 further promotes PI3K pathway activation. AKT regulation of the tuberous sclerosis complexes (TSC 1/2) allows for the regulation of Ras homolog enriched in brain (Rheb) proteins which influence mTORC1 activation. GSK3β and TSC 1/2 signaling coordinate with each other to regulate cell development mechanisms. *WNT pathway*: WNT proteins bind to its specific receptor Frizzled (FRP) and LRP proteins which form a complex that recruit Dishvelled (DVL) proteins which inhibits β-catenin phosphorylation in the β-catenin

complex and thus ensuing β-catenin stabilization. Release of stable β-catenin activates nuclear processes for cell growth and proliferation. β-catenin complex consists of the proteins Axin, GSK3β, Casein kinase 1 (CK1), adenomatous polyposis coli (APC) and β-catenin. The MAPK pathway crosstalks with the PI3K pathway through GSK3β regulation by Ras proteins. The PI3K pathway crosstalks with WNT pathway through AKT regulation of GSK3β in the β-catenin complex, which further dictates the release of stable β-catenin. Activated PTEN proteins inhibit both the formation of AKT and β-catenin.

1.6.1 The MAPK signaling pathway

Studies show that melanomas commonly possess mutations in proteins in the mitogen-activated protein kinase (MAPK) signaling pathway. This pathway is activated either by receptor tyrosine kinase (RTK) binding to site specific ligands or integrin adhesion of the cell membrane and extracellular matrix [84]. Transmission of signals along this pathway utilizes Rat sarcoma (Ras) GTPase, with highest level of activity occurring in the inner leaflet of the plasma membrane [85]. The most common somatic mutations in the MAPK pathway are activating point mutations found in the b-Raf murine sarcoma viral oncogene homolog (BRAF, around 50% of melanomas) [86]. Being a member of the RAF protein family, BRAF plays a major role in regulating cell growth and proliferation in response to growth factor signaling [87]. 97% of BRAF mutations occur in codon 600 of the gene, where an amino acid substitution in the activation segment within the kinase domain forms a constitutively active form of the protein. A large majority of these mutations (90%) are compromised of the V600E missense mutation, that converts valine to glutamic acid, and contributes to around half of all metastatic melanoma cases [88,89]. The V600K is the second most common mutation, with the conversion of valine to lysine. Intriguingly, BRAF V600E mutations are also exhibited in 68% of benign nevi, but due to the stability of their formation, it is suspected that these mutations might not contribute to melanoma carcinogenesis [90]. The signaling cascade results in the phosphorylation of MEK1/2 dual-specificity protein kinases and subsequent activation of ERK1 and ERK2 MAPKs, which are capable of translocating into the nucleus to regulate a range of transcription factors [91,92]. 60 – 70% of vertically growing lesions and metastatic melanoma possess BRAF mutations, indicating the effect of this oncogenic mutation on the cancer progression process [93]. Several therapies targeting mutated BRAF have been developed in recent years.

1.6.1.1 NRAS

The second most prevalent mutations occurring in melanoma cases involve the neuroblastoma Ras viral oncogene homolog (NRAS). Mutations have been reported in 15-20% of melanoma cases, with 98% of activating mutations detected in the Q60/61 and G12/13 codons (Ras isoforms) [94,95]. NRAS is an important constituent of the MAPK pathway, and is a member of the Ras protein class responsible for modulating Raf protein activity [89,96]. Although this means that both these oncogenes operate within the same pathway, concurrent mutations in both oncogenes are rarely reported in the same patient. This suggests that BRAF and NRAS mutations may operate mutually exclusive of each other [97–99]. Patients possessing NRAS mutations show manifestations of thick vertical growth tumors, most likely owing to the increased cell proliferation rates instigated by the mutation process [94]. Furthermore, NRAS driven activations affect both the phosphoinositide 3-kinase (PI3K) and MAPK signaling pathways, making the design of effective NRAS inhibitors challenging in the development of targeted therapies.

1.6.2 The PI3K signaling pathway

Mutations in the phosphatidylinositol-3-kinase (PI3K) signaling pathway are often found during the course of melanoma progression [100,101]. This pathway is strongly involved in cell proliferation and survival and also promotes cell viability through inhibition of apoptosis [102]. Oncogenic Ras is involved in MAPK signaling and also acts as a positive upstream regulator of the PI3K pathway [103]. The most frequent mutation observed is an inactivation mutation in the phosphatase and tensin homolog (PTEN) tumor suppressor gene. PTEN is a critical negative regulator of protein kinase B (AKT) by preventing its phosphorylation, with subsequent inhibition of the PI3K pathway. Furthermore, it also plays a role in targeting and dephosphorylating proteins such as focal adhesion kinase (FAK), which results in the inhibition of focal adhesion development and a reduction in cellular migration [104]. A mutation in PTEN leads to a competitive growth advantage that promotes tumor growth and metastasis. Mutational changes in PTEN account for 10% of primary melanomas [105,106]. While former analyses of melanoma tumor samples have identified a rate of around 3% PI3K missense mutations [107,108], there are multiple avenues for the PI3K pathway to be hyperactivated (including NRAS activation) [109]. Furthermore, PTEN mutations are frequently associated with BRAF mutations, causing simultaneous upregulation in both the PI3K and the MAPK pathways [110]. Therefore, hyperactivation of this pathway often results in disease resistance to chemotherapy and radiation treatment [102]. Studies have shown high rates of both BRAF and PTEN mutations occurring concomitantly in cases of melanoma, with NRAS mutations (described

in **1.5.4.1**) occurring mutually exclusive to both former mutations [111].

1.6.3 The WNT signaling pathway

The WNT signaling pathway plays a major role in regulating crucial cellular processes, including cell proliferation, migration and fate determination [112]. The complexity of this pathway is emphasized by the numerous cell-signaling cascades activated upon ligand binding [113]. The primarily well recognized pathway is adherens junction molecule β-catenin dependent, and is involved in the accumulation and translocation of β-catenin into the nucleus to initiate WNT target gene expression (including upregulation of c-MYC, ZEB-1 and cyclin D1 genes) [114,115]. These genes promote cell proliferation and cell cycle progression, as well as act in the inhibition of E-cadherin expression in a wide range of cancers including melanoma [116–118]. Abnormalities in WNT pathway activation is regarded as one of the major instigators of melanoma development, with aberrant signaling speculated to affect different stages of tumor progression [119]. β-catenin dependent WNT signaling has been seen to operate synergistically with the MAPK signaling cascade, cumulatively contributing to melanoma formation and pathogenesis [120]. Studies have also provided evidence of tumor metastasis promotion during the activation of non-canonical WNT signaling pathways [121–123]. The impact of WNT signaling in melanoma is highly complex and involves the coordinated expression and distinctive activation of several intracellular molecules and interacting pathways through progressive stages of the disease. As such, the precise functions of the WNT pathways in melanoma remain to be completely elucidated.

1.6.4 Other mutations and processes

1.6.4.1 NF 1

The tumor suppressor gene Neurofibromin (NF1) undergoes inactivating mutations in about 15% of cutaneous melanomas and are associated with 50% of BRAF/NRAS wild type tumors [124–126]. NF1 is a GTPase activating protein which functions as a negative regulator within the MAPK pathway to promote the hydrolysis of RAS-bound GTP to inactive GDP-bound RAS [127–129].

1.6.4.2 p53

The tumor suppressor gene p53 regulates DNA repair and apoptosis and is implicated in several human malignancies, including prostate, colorectal, breast and lung cancer (36.1% of all cancers) [130–133]. It is activated during DNA damage or cell stress and induces cell death. While its role is disputed, there is a varying prevalence of p53 mutations in immunohistochemical analyses of

melanoma, reporting altered expression rates from as low as 11% to as high as 85% [134–136]. Regardless of this fluctuating range, melanoma cells which express resistance to gamma radiation and chemotherapy often indicate an improper functioning of p53.

1.6.4.3 Exosomes and vesicular trafficking

Studies have provided increasing evidence of altered vesicular trafficking in cases of melanoma [137,138]. This includes the release of exosomes, a class of cell derived extracellular vesicles originating from endosomes and serving as carriers of 40-150 nm size biomolecules between virtually every cell type within the body and the extracellular environment [139,140]. The primary role of exosomes is intercellular communication, and they possess a wide range of cellular constituents including lipids, proteins, DNA, mRNA and miRNA [141]. The role of exosomes has been identified in immune regulation, intercellular protein and gene exchange, therapy response regulation and melanoma progression [142]. Non canonical WNT signaling has been heavily linked with pro-angiogenic and immunosuppressive responses via exosome release processes in malignant melanoma cells [143,144]. Furthermore, the transfer of miRNAs and proteins via exosomes to a wide range of cell types including endothelial cells, bone marrow progenitor cells and fibroblasts indicate their involvement in the crosstalk between melanoma cells and the microenvironment [145]. Further investigation in this area could provide vital information of exosome contribution in the promotion of melanoma proliferation and invasiveness.

1.7 The Brain Metastasis Process

Around 50% of melanoma patients with metastatic disease exhibit spread to the brain, a number that rises to 73-90% at autopsy [146–148]. Metastasis to the brain occurs in a series of steps termed the "metastatic cascade", the successful completion of which results in the formation of metastatic lesions within the brain **(Figure 1.5)**. The process is initiated by the primary tumor, which promotes angiogenetic factors to establish a blood supply in the host organ for the transfer of oxygen and metabolic components for tumor growth. This is followed by the invasion and cellular migration across the basement membrane and intravasation into surrounding blood vasculature, survival in the circulation system, extravasation from the vasculature into the brain parenchyma and finally, colonization and formation of solid tumors in the brain [149]. The mechanism of local invasion of tumor cells heavily relies on the epithelial to mesenchymal transition (EMT) process, in which cells readapt themselves to obtain improved migration and invasive properties [150,151]. Epithelial tumor cells initiate the EMT process by acquiring motility and breaking down the

underlying basement membrane and extracellular matrix (ECM) proteins, permitting their entry into the blood or lymphatic circulation. This transition is mediated by a variety of factors, including cytokines, hypoxia or the release of growth factors [152]. However, the survival rate of tumor cells in the circulation cells is low, owing to the action of the immune system, the shear forces applied on the cells as well as the lack of adhesion signaling systems [153]. Melanoma cells with the potential for brain colonization develop mechanisms which allow them to survive in the circulation and reach the brain, where they attach to endothelial cells in the microvasculature and extravasate through the BBB [154]. These tumor cells proceed to interact with the brain microenvironment (BME) to promote neoangiogenesis, vessel co-option (migration of tumor cells along the pre-existing vasculature to obtain higher access to nutrients) [155] and perivascular proliferation [156]. The steps in the process culminate in metastatic colonization and steady transition from micro- to macrometastases. It is now recognized that tumor cells from different primary cancers possess a tropism to specific tissue, enabling them to "home" to various secondary organs [157]. This reflects the "seed and soil" therapy of Paget [158], who first visualized the metastatic process as a non-random process involving specific tumor cell clones (the "seed") which possess specific affinity for a particular microenvironment existing in target organs (the "soil"). The mechanisms directing brain metastasis remain to be fully elucidated, especially with regard of the association of the brain vasculature with the metastatic process.

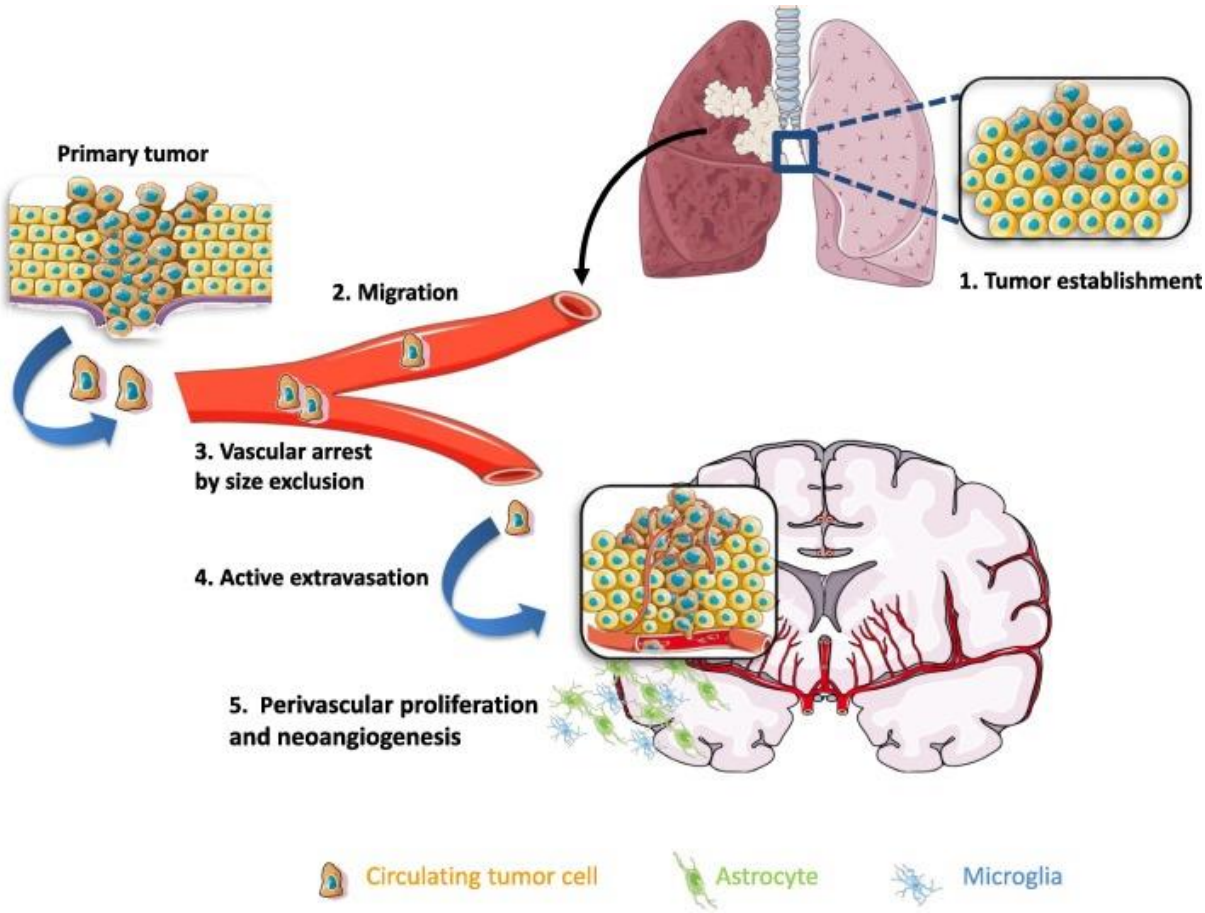

Figure 1.5 Steps in the "metastatic cascade" during tumor metastasis to the brain. 1. Tumor establishment – Formation of the primary tumor in the primary organ. 2. Migration – Invasion of primary tumor cells across the basement membrane and intravasation into surrounding blood vasculature. 3. Vascular arrest by size exclusion – Survival of tumor cells in the circulation is determined by their size (relative to blood vessels) and resistance to shear forces in the bloodstream. 4. Active extravasation – Movement of surviving tumor cells into the brain parenchyma. 5. Perivascular proliferation and neoangiogenesis – Interaction of tumor cells with the BME to promote formation of new blood supply and proliferation of secondary tumor in the metastatic niche. Figure adapted from El Rassy, E.; Botticella, A.; Kattan, J.; Le Péchoux, C.; Besse, B.; Hendriks, L. Non-Small Cell Lung Cancer Brain Metastases and the Immune System: From Brain Metastases Development to Treatment. *Cancer Treatment Reviews*. W.B. Saunders Ltd July 1, 2018, pp 69–79. https://doi.org/10.1016/j.ctrv.2018.05.015.

1.8 Transformation of the Brain Microenvironment

The brain microenvironment is a mosaic possessing extracellular matrix components and a number of specialized cell types, namely astrocytes, endothelial cells, neurons, microglia,

oligodendrocytes and pericytes [159]. Astrocytes are specialized glial cells which out populate neurons in the BME around fivefold. They are characterized by their contiguous spread across the CNS and respond to injury and pathogenesis via a process called reactive astrogliosis, now a pathological hallmark detected in structural lesions present in the CNS [160].

Endothelial cells possess tight junctions and are highly prevalent across the BBB, forming the perimeter in the network of blood capillaries spread across the brain [161]. While mechanisms of metastatic cell binding to endothelial cells are poorly understood, the process is speculated to be regulated by interactions between tumor cells and endothelial cell adhesion molecules [162,163]. The components in the brain microenvironment regulate physiological homeostasis and strategizes the feedback to pathological, including metastatic, dysregulations. Intercellular communication plays a major role in directing the heterotypic and homotypic interactions within the BME. Studies have shown that tumor cells induce cell reprogramming in the BME, allowing the formation of hospitable "pre metastatic niches" which promote metastatic growth [164,165]. Primary tumors release a multitude of growth factors, soluble factors, extracellular vesicles (exosomes), cytokines, proteases and miRNAs to stimulate angiogenesis and tumor proliferation in the premetastatic niche [166–168]. However, it is still unclear as to how these microenvironment changes promote metastatic seeding and tumor proliferation.

Astrocytes (50% of brain cell population) and microglia (10 – 15% of brain cell population) have been recognized to express inflammatory cytokines and growth factors associated with promoting brain metastases [169]. The CNS is considered a distinctive organ for BM due to its lacking of lymphatic vessels and its enclosure by the BBB [170]. Recent research has identified the existence of meningeal lymphatic vessels which mediate communication between the brain and the immune system [171]. Metastasizing cells arrive by the arterial blood supply and attach to the endothelial tissue around blood capillaries, preceding the invasion of the BBB [172]. Metastatic colonization in the pre metastatic niche concludes the formation of the brain metastatic niche (the "prepared" brain microenvironment).

1.9 The Blood-Brain Barrier (BBB)

The BBB is composed of specialized endothelial cells lined by the basal lamina, astrocytic endfeet processes which interact with the capillary bed, pericytes and microglia [173]. It restricts the free migration of substances such as solutes and cellular elements between the systemic circulation into

the neuronal tissue [174]. The selective entry of the BBB permits the passage of a small group of substances, including lipid soluble molecules (such as oxygen, carbon-dioxide), compounds consisting of less than 8 to 10 hydrogen bonds and smaller than 400-500 Da. This greatly narrows down the entry of large molecule drugs (such as antibodies) and also the majority (98%) of small molecule drugs [175,176]. Several studies have already indicated the involvement of the BBB in the pathogenesis of several CNS disorders [177,178].

The physiological architecture of the BBB is coordinated by several transport, physical and metabolic properties possessed by the endothelial cells, which in turn are regulated by interactions with various neural cells, immune perivascular macrophages and vascular cells. The function of the barrier depends on tight junction proteins (such as claudins, occludins and junctional adhesion molecules), which cooperate with each other to limit the passive diffusion of solutes (small ions and drug molecules) into the extracellular region of the CNS [179–181]. Animal studies have provided evidence of the cooperation between endothelial cells and cells of the parenchyma, particularly astrocytes, to maintain the formation of the BBB. This implies that the BBB integrity is not intrinsically regulated by endothelial cells alone but also in association with cellular elements of the brain microenvironment [182]. Astrocyte perivascular endfeet are situated in close proximity to cerebral microvessels, facilitating signaling crosstalk between astrocytes and endothelial cells and inducing tighter junction formation in the BBB [180]. The BBB and its individual components are illustrated in the figure below **(Figure 1.6)**.

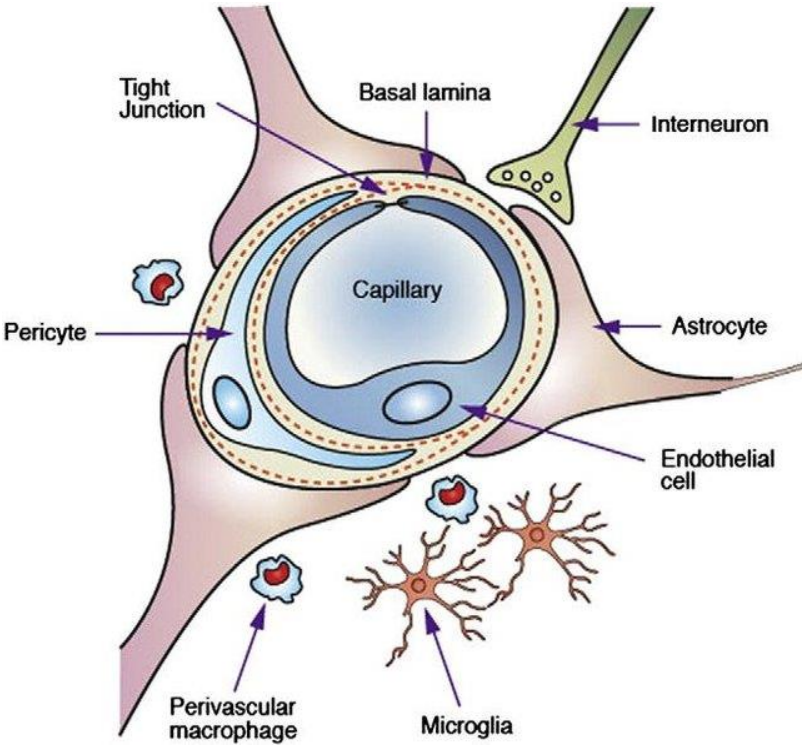

Figure 1.6 The physiological architecture of the blood-brain barrier (BBB) and its constituents (endothelial cells, astrocytes, basal lamina and pericytes), as well as surrounding coordinating cells (microglia, perivascular macrophages and interneurons). Figure taken from A Review on Novel Techniques for Drug Delivery to the Brain https://www.researchgate.net/publication/282332393_A_Review_on_Novel_Techniques_for_Drug_Delivery_to_the_Brain

During the course of tumor progression, there is a disruption of the BBB, resulting in the formation of the blood tumor barrier (BTB) [183,184]. Several studies have indicated an intervention by melanoma cells to adhere and impede brain endothelial cell interactions via the disruption of adherence junction proteins (claudin 5 and ZO-1) [185]. This interference facilitates the transmigration of melanoma cells across the BBB. Furthermore, the release of proteolytic enzymes such as seprase (Fibroblast Activation Protein Alpha; FAP) and heparanase (HPSE1) aid in the infiltration of metastatic cells into the brain extracellular space [186,187]. Treatment strategies have already been developed with the aim of temporary disruption of the BBB to facilitate improved drug delivery [188–191]. These include hyperosmotic openings, radiotherapy, focused ultrasound incorporated with microbubble contrast agents, surface protein modulation, convection enhanced delivery, polymer wafers, carrier molecules and viral mediated delivery. However such strategies have expressed limited success, each with their own strengths and weaknesses, calling for more

effective model breakthroughs [192,193].

1.10 Tunneling Nanotubules (TNTs)

Tunneling nanotubes (TNTs) is a dynamic and novel route for inter- and intracellular communication. TNTs operate using mechanisms distinct from the secretion of signaling molecules or the transmission of signals across adjacent cells via gap junctions [194]. Reported initially in the rat pheochromocytoma (PC12) cell line [195,196], TNTs are long range cytoplasmic channels utilized in direct cell to cell communication. By definition, they are recognized by three phenotypic criteria – they bridge a minimum of two cells, they possess F-actin and they do not come into contact with the substrate [197,198]. Structurally, TNTs exhibit a variation of widths between 50 nm to 1000 nm, and they are less than 100 µm in length [199–201]. Furthermore, they demonstrate membrane continuity via open ended or close ended (interposed gap junction) TNTs [194,202,203].

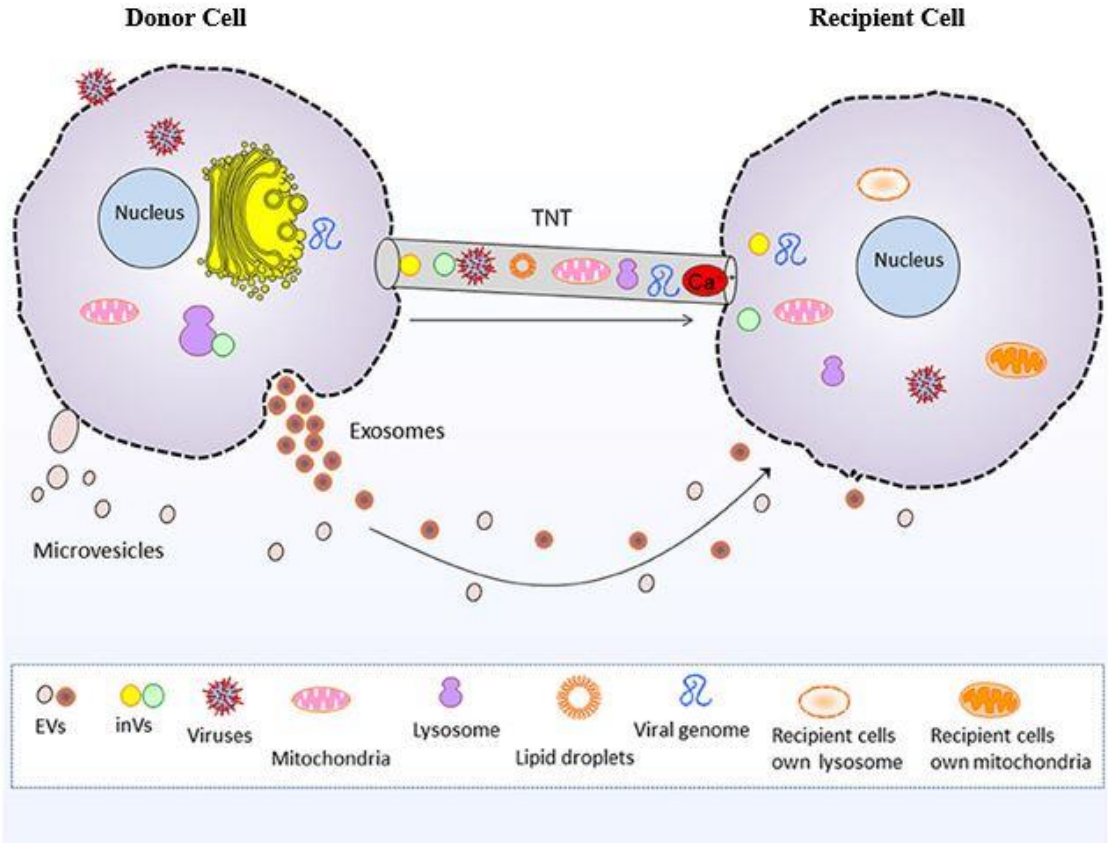

Figure 1.7 TNT and extracellular vesicle (EV) mediated intercellular communication and cargo transfer between donor and recipient cell. TNT cargo includes mitochondria, intracellular vesicles (inVs), lysosomes, viruses and viral genomes, lipid droplets and Ca^{2+} ions. EVs, namely exosomes and microvesicles, transfer nucleic acids, proteins and lipids between cells. Figure adapted from

Nawaz, M.; Fatima, F. Extracellular Vesicles, Tunneling Nanotubes, and Cellular Interplay: Synergies and Missing Links. *Frontiers in Molecular Biosciences*. Frontiers Media S.A. July 18, 2017, p 50. https://doi.org/10.3389/fmolb.2017.00050

The TNTs enable a rapid transfer of cellular cargo among a wide range of non-adjacent cells [202,204–206] **(Figure 1.7)**, and are found in several organisms and tissue types [199,207–214]. TNTs are known to be involved in the transfer of several cytoplasmic molecules, including lysosomes, pathogens, proteins, miRNAs and mitochondria [215]. Furthermore, they are implicated in cancer progression and metastasis, later stages of neurodegeneration, routes of spread for pathogenic agents and stem cell mediated regeneration and homeostasis [216,217]. The earliest detection of TNTs in human primary cancel cells and solid tumors *in vitro* [199] were succeeded by the observation of thin tumor-originating membrane tubes *in vivo*. The latter, termed as tumor microtubes (TMs), exhibited a greater length and diameter compared to TNTs observed *in vitro* [218]. Intercellular communication by TNTs are speculated to contribute to tumor survival and progression, acting as spatial and specific communication conduits between signal directing and signal receiving cell membranes [219,220].

The presence of TNTs in cancer cells is well documented, and they have been reported in cell populations of glioblastoma, squamous cell carcinoma, prostate cancer, ovarian cancer, adenocarcinoma and osteosarcoma, among others. Furthermore, TNTs have also been detected in distinct tumor types from patient explants [221–224]. Cancer cells coordinate TNTs to form a network of communication between malignant cells (homotypic interactions) and TME cells (heterotypic interactions) [217]. The potential role of TNTs in BM has however not been reported. Two models of TNT formation via cell-cell interactions in different cell types are currently recognized. The first model is termed the “cell dislodgement” model and proposes the presence of TNT formation between two adjacent cells as they move apart [225,226]. The second model is termed as the “filopodia interplay” model and interprets TNT generation from active cellular protrusions initiating direct contact between neighbouring cells [227,228].

1.11 Treatment Strategies of Melanoma

In recent years, there have been advancements in both local and systemic therapy of melanoma. The complexity of the disease and the myriad of treatment options calls for melanoma BM patients to be evaluated within a multidisciplinary setting to enable personalized treatment. Such appraisal

requires an assessment of several factors including the molecular classification of the disease, BM frequency and size, patient performance status and information on prognostic groups. Improved treatment outcomes have pushed for effective treatment strategies which maintain patient quality of life while minimizing neurological toxicity.

1.11.1 Standard treatment strategies

Traditionally, the treatment of BM relies on surgery or radiotherapy in combination with chemotherapy. Surgical resection is commonly used in cases where the patients have solitary or a few metastasis, often localized adjacent to critical brain structures [229,230].

Whole brain radiotherapy (WBRT) in combination with corticosteroids has also been considered a typical initial treatment for BM, with the flexibility of administration alone or post-surgery [231]. However, the use of radiation treatment often results in neurocognitive decline [232].

Stereotactic radiosurgery (SRS) involves the delivery of a focused single high dose of radiation by x-ray or gamma radiation. SRS has provided positive results, demonstrating a statistically similar outcome in overall patient survival to WBRT [233].

1.11.2 Novel treatment strategies

1.11.2.1 Immunotherapy

Immunotherapy has emerged as a promising treatment of melanoma, which is highly immunogenic in nature and sometimes exhibit immune mediated spontaneous regression [234]. The monoclonal antibody Ipilimumab is a cytotoxic T lymphocyte-associated protein 4 (CTLA-4) inhibitor which promotes cellular immunity and decreases tolerance to tumor associated antigens [235]. As a result, this strengthens the immune response against metastatic melanoma tumors. Pembrolizumab and nivolumab (programmed cell death 1 [PD-1] inhibitors) are also monoclonal antibodies which have shown promise in treatment of asymptomatic melanoma BM and capable of initiating programmed cell death [236,237]. However, while immunotherapy has demonstrated encouraging results, it is speculated that patients on steroids may not be responding to the therapy, and that they are at risk of developing extensive neurological symptoms [238].

1.11.2.2 Inhibitors of proteins in the MAPK pathway

1.11.2.2.1 MEK inhibitors

Trametinib received approval by the US FDA in 2013 for BRAFV600E or BRAFV600K positive unresectable or metastatic melanomas. Its mechanism emphasizes on the inhibition of MEK signaling pathways downstream of BRAF. However, a significant decrease in disease response has been reported in trametinib treatment against BRAF wild type melanomas and in patients who had already undergone BRAF inhibitor therapy [239].

1.11.2.2.2 BRAF inhibitors

The discovery of BRAF mutations in melanoma has paved the way for new avenues of therapy, using small molecule BRAF inhibitors (such as vemurafenib and dabrafenib). These drugs target the BRAF protein and clinical trials have shown increased survival. The implication of BRAF inhibitors in the MAPK pathway is highly characterized, as illustrated in the figure below **(Figure 1.8)**.

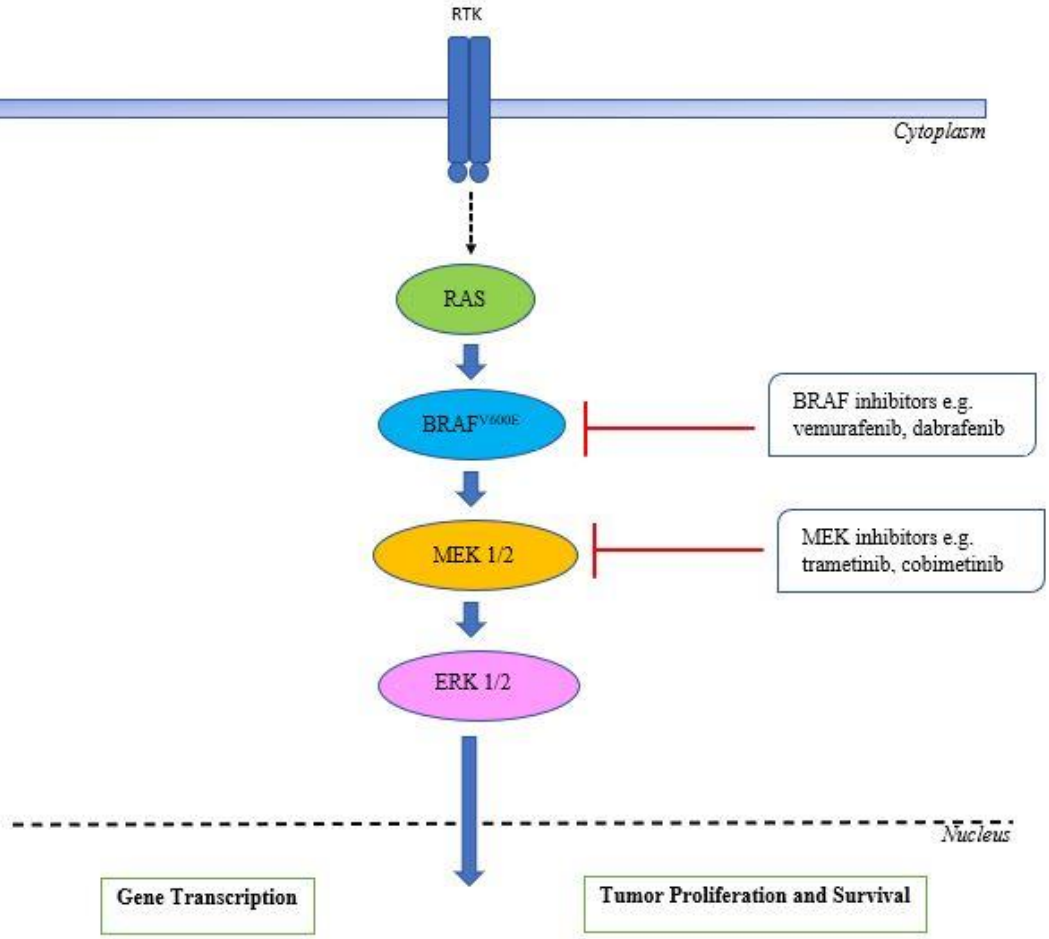

Figure 1.8 BRAF and MEK inhibitor activity in the MAPK pathway (activated by RTK ligands). BRAF inhibitors act on mutated BRAF^{V600E} to inhibit signal transduction to MEK 1/2. MEK inhibitors act lower down the pathway, and act on MEK 1/2 to inhibit signal transduction to ERK

1/2 proteins.

The oral serine-threonine kinase inhibitor vemurafenib (PLX4032, RG7204) was one of the first mutant-specific inhibitors of BRAF, and it has been shown that cell lines possessing the $BRAF^{V600E}$ mutation are sensitive to the drug [240]. The drug was approved by the U.S Food & Drug Administration (FDA) in 2011 for use in therapy of advanced stage melanoma, due to inhibitory effects on cell cycle arrest and induction of apoptosis [241]. While research into BRAF specific inhibitors progresses [242], the antitumor activity of vemurafenib in melanoma BM models requires greater investigation and further clinical trial data than what has already established by *in vitro* [243] and *in vivo* models [244,245]. A concern in treatment is that the tumors develop resistance to vemurafenib, around six months after initiation of therapy [246–249]. Thus, current therapy strategies combine vemurafenib with other targeted therapies to provide more effective treatment. Currently, combined therapies using vemurafenib and immunotherapy agents atezolizumab and cobimetinib are being evaluated [250].

Dabrafenib (GSK2118436) is a selective inhibitor which has exhibited strong treatment outcomes as a single agent in patients possessing BRAF mutated advanced melanoma. However, resistance to this drug is also developed after about 6 months of treatment [251]. Combination therapy of dabrafenib with the MAPK/MEK inhibitor trametinib was approved by the US FDA in 2018 has shown more positive results [252–254] **(Table 1.4)**. Further, randomized phase 3 studies combining dabrafenib and vemurafenib yielded statistically significant treatment outcome in terms of overall survival (OS), progression-free survival (PFS) and overall response rate (ORR) in comparison with chemotherapy **(Table 1.4)**.

Primary and acquired treatment resistance is a significant challenge to the development of effective BRAF and MEK inhibitors **(Figure 1.8B)**. Besides combination therapy, treatment development strategies have also focused on other signaling proteins (CRAF, ARAF), mutational changes in other major effector proteins and activating tyrosine kinase receptors to stimulate survival pathways [255]. The paradoxical effect of BRAF inhibitors on BRAF-wild type cells was also an unexpected finding in the development of BRAF inhibitors [256].

A summary highlighting the treatment outcomes of selected targeted therapy trials in BRAF-mutant advanced melanoma is provided in the table below **(Table 1.4)**.

Table 1.4 Treatment outcomes of selected targeted therapy trials in BRAF-mutant advanced melanoma (Adapted from [257]).

Trial	**Drugs**	**Median OS (mo)**	**Median PFS (mo)**	**ORR**	**References**
BRIM-3	Vemurafenib	13.6	6.9	57%	[258,259]
	Dacarbazine	9.7	1.6	9%	
BREAK-3	Dabrafenib	18.2	6.7	53%	[260,261]
	Dacarbazine	15.6	2.9	6%	
Combi-D	Dabrafenib + trametinib	25.1	11	69%	[254]
	Dabrafenib	18.7	8.8	53%	
Combi-V	Dabrafenib + trametinib	26.1	12.1	68%	[262]
	Vemurafenib	17.8	7.3	50%	
CoBRIM	Vemiurafenib + Cometinib	22.3	12.6	70%	[263]
	Vemurafenib	17.4	7.2	50%	
COLUMBUS	Encorafenib + Binimetinib	33.6	14.9	64%	[264]
	Vemurafenib	16.9	7.3	41%	
	Encorafenib	23.5	9.6	52%	

**Abbreviations: OS, overall survival; PFS, progression-free survival; ORR, overall response rate; mo, months*

2. Aims

The main aim of this Master thesis was to develop *in vitro* 3D model systems to be used for studying interactions between MBM and the brain metastatic niche.

Six sub aims were defined for the work in this Master thesis:

1) To culture the human MBM cell line H1, hTERT-immortalized normal human astrocytes (NHA) and hCMEC/D3 cerebral endothelial cells followed by sorting of cell lines for high expression of fluorescent protein.
2) To optimize the cell number/ratio of the human MBM cell line H1 relative to hTERT-immortalized normal human astrocytes (NHA) to achieve an evenly distributed monolayer coculture.
3) To provide essential information in a “systems biology” approach, through the evaluation of possible TNT interactions between MBM and NHA using confocal microscopy.
4) To treat cells in co-culture with anti-cancer drug vemurafenib (PLX4032) and evaluate treatment effect on TNT interactions.
5) To establish an *in vitro* BBB model utilizing the Boyden Chamber technique.
6) To assess the migration of the H1 BM cell line using the *in vitro* BBB model.

3. Materials and Methods

3.1 Cell Lines

The human melanoma brain metastasis cell line H1 used in this work was established in our laboratory from a patient biopsy obtained after surgery at Haukeland University Hospital, Bergen, Norway. Written consent was obtained from the patient prior to the collection of tumor tissue material. The collection of tumor material, generation of cell lines and cell line work have been ethically approved (Regional Ethical Committee Approvals no 2013/720 and 2020/65185). The H1 cell line harbors the $BRAF^{V600E}$ mutation, as described previously [148]. BRAF mutation status of the H1 cell line was investigated via massive parallel sequencing of the tumor DNA, based on published protocols [265]. H1_DL2 cells were generated in the laboratory by transducing H1 melanoma cells with two lentiviral vectors encoding green fluorescent protein variant Dendra and Luciferase [266]. Flow cytometric isolation of cells by green fluorescent protein (GFP) expression was performed (BD FACS Aria, Becton Dickinson, Franklin Lakes, NJ, USA).

Both Normal Human astrocytes (NHA) and NHA dsRed were provided by Professor Per Øyvind Enger´s Research Group at The Department of Biomedicine, University of Bergen. NHA dsRed constitutes of human telomerase reverse transcriptase (hTERT)-immortalized human astrocytes (Applied Biological Materials Inc., Vancouver, Canada), transduced with red fluorescent protein (RFP) lentivirus gene expression vector (pLV[Exp]-Hygro-CMV>mCherry) expressing dsred [267]. Positive cells were selected by flow cytometry. hTERT is an enzyme responsible for the elongation and maintenance of telomere length to regulate cell life span and cell replication potential. Telomerase reactivation is a distinctive feature of human germ line and most cancer cells, and prolongs the time taken for cells to progress to the senescence or apoptosis stage [268].

Human blood-brain barrier cerebral endothelial cells (hCMEC/D3) were purchased from Merck Millipore (EMD Millipore, Temecula, USA) and have been extensively characterized for brain endothelial phenotype and is a model of human blood-brain barrier (BBB) function [269]. hBEC lucGFP was generated in our lab by transducing hCMEC/D3 cells with Firefly luciferase-GFP lentivirus (CMV, Puro) (PLV-10172, Cellomics Technology) according to standard laboratory procedure.

3.2 Cell Cultures

All cell lines were cultured in ALT-DMEM cell growth medium (**Table 3.1**). Heat inactivation of fetal calf serum was carried out by exposing the serum to a temperature of 56 ºC for 30 mins in a water bath. All cells were incubated in a standard tissue culture incubator at 37 °C, 100% humidity and 5% CO_2. Cell culture work was performed under sterile conditions inside a laminar airflow hood, with working surfaces and equipment disinfected with 70% ethanol. The cell lines were incubated in T75 culture flasks (Nunc, Roskilde, Denmark) and tested for mycoplasma every 2nd month during the laboratory work described in this thesis.

Table 3.1 Reagents in the ALT-DMEM cell growth medium

Reagent Name	**Company**
ALT-DMEM	
Dulbecco's Modified Eagle Medium	Sigma-Aldrich Inc., St. Louis, MO, USA
10% heat inactivated newborn calf serum	Thermo Fischer Scientific, Waltham, MA, USA
5 mg/mL Plasmocin	Invitrogen, Toulouse, France
2% L-glutamine	BioWhittaker, Verviers, Belgium
100 IU/mL penicillin	BioWhittaker
100 µL/mL streptomycin	BioWhittaker
1X PBS	
10x Dulbeccos phosphate-buffered saline	Sigma-Aldrich Inc.
Autoclaved MilliQ water	Merck Millipore, Molsheim, France
Trypsin – Versene Mixture (Trypsin EDTA)	BioWhittaker

3.2.1 Thawing of cells

The cell cryovial was removed from the nitrogen tank and thawed by rolling in warm hands or by placing in a water bath at 37 ºC. The cell suspension was then transferred using a pipette with filter tip to a 15 mL polypropylene centrifuge tube (Sarstedt, Nümbrecht, Germany) containing 5 mL cold cell growth medium and resuspended with gentle pipetting. After centrifuging the cells at 900 rpm for 4 min, the medium supernatant was removed, and the cells were resuspended in 5 mL cold cell growth medium. The cells were then pipetted into desired culture flask and additional

prewarmed growth medium was added.

3.2.2 Splitting of cells

Splitting of H1 cells were carried out using a protocol established in the laboratory. The cells were prepared in standard T75 culture flasks (Nunc) and the cultures were split upon reaching around approximately 80% of confluency. The old growth medium was first removed from the cell culture and the cells were washed with sterile phosphate buffered saline (1XPBS) solution. The PBS was removed, and 2 mL prewarmed Trypsin EDTA solution was added to the cells before incubating for 3-5 mins at 37 °C, 100% humidity and 5% CO_2. Cell detachment was evaluated through observation under light microscope after incubation. Growth medium (5-8 mL) was then added to the cell culture before centrifuging the cell suspension solution at 900 rpm for 5 min. The medium supernatant was then removed, and the cell pellet was gently resuspended in the desired volume of prewarmed ALT-DMEM. The cell suspension was then transferred back to T75 culture flask containing appropriate volume of prewarmed cell growth medium. Both H1_DL2 and hBEC lucGFP cell lines were used for a maximum of 10 passages before being replaced. NHA dsRed cell lines were used for a maximum of 5 passages before being replaced.

3.2.3 Freezing down of cells (Cryopreservation)

The freezing solution was prepared by mixing Solution 1 and 2 in a 1:1 (**Table 3.2**). The solution was stored in the fridge (4 ºC) until use.

Table 3.2 Reagents for Solution 1 and 2 in preparation of freezing solution

Solution 1 (20% serum)	Solution 2 (20% DMSO
9 mL (9v) ALT DMEM	8mL (4v) 1xPBS
1 mL (1v) Fetal Calf Serum	2mL (1v) 100% DMSO

Cells for freezing down were first washed, trypsinized and centrifuged as described in **3.2.2**. The medium supernatant was then removed, and the cell pellet was resuspended gently and thoroughly in a desired volume of freezing solution (1mL per 2 x 10^6 - 2.5 x 10^6 cells). 1 mL of cell suspension was then aliquoted per cryotube (Nunc) and cryotubes were appropriately labelled. The cells were kept in freezer (-80 ºC) for 24 hrs before being transferred to the nitrogen tank.

3.2.4 Cell counting for *in vitro* experiments

Cell counting was carried out using an automated cell counter (The Countess™, Invitrogen, Oregon, USA). 1 mL of the cell solution was moved into an eppendorf PCR tube (Sarstedt, Nümbrecht, Germany). 20 µL of cell solution was placed on a strip of parafilm paper before being stained with an equal volume of trypan blue. The cell solution was pipetted into both chambers of a cell counting chamber slide before the slide was placed in the cell counter for quantitative analysis. The mean number of cells/mL in the cell solution was calculated using the mean value of two individual counts of live cells/mL from the cell counter.

3.2.5 Preparation of two-dimensional cell cocultures

Two-dimensional (2D) cell cocultures of H1_DL2 and NHA dsRed cells were prepared in 24 well plates (Nunc, Roskilde, Denmark). Initially, both cells were seeded (in seeding densities and ratios described in 3.3.1) on the same day and observed using a Nikon TE2000 inverted light microscope (Nikon Instruments Inc., NY, USA) after 24 hrs of incubation. It was seen that confluency of astrocytes was much lower relative to that of melanoma cells. To account for this, NHA dsRed cells were seeded 24 hrs prior to the seeding of H1_DL2 cells to allow for earlier surface adherence of astrocytes and consequently greater confluency. Non-uniform distribution of cells was minimized by adding the cell suspension to the plate dropwise and shaking the plate in a cross like pattern (forward-backward and left-right) three or four times. Care was taken when putting the plate back into the incubator by preventing any swirling or spiraling motion.

3.3 Establishment of TNT Interaction Model

The initial idea behind establishing the TNT interaction model was to determine if TNT formations were present in BM models *in vitro*, and if so, determine interactions between H1_DL2 and NHA dsRed cells in monolayer cocultures. This was followed by quantification of all types of TNT interactions (both homotypic and heterotypic) between the two cell populations and evaluation of any trends after coculture treatment with anticancer drugs.

3.3.1 Determination of optimal cell seeding densities for confocal visualization

Cells were passaged and counted prior to seeding in 24 well plates (Nunc). The chosen cell densities and coculture ratios for H1_DL2 and NHA dsRed cells are shown in **Table 3.3**. Cells were seeded in duplicates in the desired cell densities.

Table 3.3 Cell seeding densities and corresponding ratios used in thesis

Number of H1_DL2 cells	Number of NHA dsRed cells	Coculture ratio
2.5 x 10^4	2.5 x 10^4	1:1
5 x 10^4	5 x 10^4	1:1
7.5 x 10^4	7.5 x 10^4	1:1
2.5 x 10^4	5 x 10^4	1:2
5 x 10^4	2.5 x 10^4	2:1

The cell plates were then incubated at 37 °C, 100% humidity and 5% CO_2 for 24 hrs before being transferred to the IncuCyte Live Cell Imaging System (Essen BioScience Ltd. Hertfordshire, UK) for live visualization.

3.3.2 Evaluation of coculture cell proliferation

Cell proliferation was evaluated under the 20x objective of the IncuCyte Live Cell Imaging System (Essen BioScience Ltd.). Images were taken every 30 mins for 72 hr of four regions in each well preset by the system and the images taken every 2 hrs were evaluated for the study. Subsequent analyses were performed using the Basic Analyzer software module (Essen BioScience Ltd.) of the system. Each experiment was repeated three times. Images obtained were used to visually determine optimal seeding density for the visualization of TNTs. This was done based on three factors – the degree of cell confluency within field of view, the uniform distribution of cells within the monolayer plane and the frequency of visible interactions during the period of evaluation. Visualization periods with well-spaced uniform growth distribution of cells were opted for on the premise of evidence from existing studies that TNTs displayed large variation in length, differing between cell lines [203,270–277]. Optimal confluency of cells was also a key parameter to achieve good conditions for TNT formation and existing studies have reported that high or low confluence of cells could impair TNT formations [278]. Frequency of visible interactions was also an important factor to consider, since TNTs could form via a "cell dislodgement" mechanism where two cells initially in contact disassociate from each other with the attachment of membrane that develops into a TNT with cytoplasmic continuity between the interconnected cells. Images obtained from the system were used to establish a suitable timepoint for confocal visualization of cocultures at a cell density of around 60-70% confluency, uniformly distributed without forming clumps or aggregates, while displaying visible interactions between the cells.

3.3.3 Hoechst staining of nuclei

Hoechst 33342 (Molecular Probes, Life Technologies) was prepared from stock solution by diluting stock concentration (10 mg/mL) to 4 µg/mL in prewarmed cell media to form Hoechst medium solution. All steps were carried out in the dark due to the photosensitivity of Hoechst dyes. Hoechst medium solution was stored wrapped in aluminum to prevent exposure of medium to light. Prior to confocal imaging, cells were seeded in µ-slide 4 well chambered coverslips (Ibidi, Gräfelfing, Munich) and the cell growth medium in wells was replaced with Hoechst medium solution and slide chambers were incubated for 1 hr at 37 °C, 100% humidity and 5% CO_2.

3.3.4 Imaging of TNT interactions

The µ-slide 4 well chambered coverslips (Ibidi) were mounted on the holder of Dragonfly 505 confocal spinning disk system (Andor Technologies, Inc., Belfast, Northern Ireland) equipped with a live-cell microscope incubation cage (Okolab, Pozzuoli, Italy) which maintained the coculture environment at 37 °C, 100% humidity and 5% CO_2. All images were captured with the iXon 888 Life EMCCD camera within the confocal system. Images were captured during the 8^{th}, 24^{th} and 33^{rd} hrs after introduction of H1_DL2 cells to coculture (based on the timepoint results obtained from the IncuCyte experiments). The cell density for each cell line were based on the results obtained from the IncuCyte experiments (Table 3.3), taking into account the differences in surface areas between µ-slide chamber wells and the well plates. The images were analyzed using the FUSION imaging software (Andor Technologies, Inc.). Objectives were chosen to facilitate the visualization of possible TNT interactions while also allowing for an appropriate visualization of areas between cell bodies in the field of view. For this study, 2x2 montages of 20x objective images were taken of each chamber. 4 40x images were then captured from each 20x objective image, using the montage as reference points. TNT interactions from H1_DL2 to NHA dsRed, H1_DL2 to H1_DL2, NHA dsRed to H1_DL2 and NHA dsRed to NHA dsRed in each 40x field of view were counted.

Cell fluorescence was visualized using preset filter protocols on the confocal system for green, red and blue fluorescence. H1_DL2 cells were imaged using a 488 nm laser line at 5% intensity, 50 ms exposure time, and a 525 nm filter. NHA dsRed cells were imaged using a 561 nm laser line at 5% intensity, 50 ms exposure time, and a 600 nm filter. Hoecsht stained cell nuclei were imaged using a 405 nm laser line at 5% intensity, 50 ms exposure time, and a 442 nm filter. TNTs were defined according to the parameters mentioned in **1.7.2**. They were distinguished from cytoplasmic bridges (cell protrusions which appear following cell division) by the absence of a midbody visible

by cytoplasmic staining. Confocal images were visualized in the 3rd dimension (X-Z plane) to evaluate TNT localization relative to the substratum. Z-stack images were taken at a step size of 1 µm. Cells were counted per chamber via visible Hoechst viable cell nuclei staining. All confocal images were processed using IMARIS 9 image analysis software (Oxford Instruments, Abington, UK), including length and width measurements of TNTs. Results were tabled and presented in graphs of relative percentage numbers using GraphPad Prism 8 (GraphPad software, Inc., La Jolla, CA, USA).

3.3.5 Evaluation of anticancer drug treatment in TNT interaction model

The drug vemurafenib was purchased from Chemietek (Indianapolis, IN, USA). Vemurafenib was dissolved in dimethylsulfoxide (DMSO) and stock concentrations of 50 mM were stored at −20 °C in aliquots prior to use. The final drug concentrations selected for evaluation of potential effects in the TNT interaction model were made in ALT DMEM (0.5, 0.8, 1 and 1.5 µM). Selection of vemurafenib drug concentrations was done based on monolayer viability drug assays previously conducted on the H1 cell line in our lab and also after consultation of scientific literature. Drug concentrations were added to the coculture systems of H1_DL2 and NHA dsRed 2 hrs prior to confocal visualization and drug effects on TNT interactions between both cell populations was quantitatively and qualitatively evaluated during the established timepoint results.

3.4 Establishment of BBB Model

The Boyden chamber technique, which is primarily employed for the study of cell migration and invasion, was used to develop our BBB model. Boyden chambers constitute of cylindrical cell culture inserts placed inside the wells of a 24 well plate. The inserts possess polycarbonate membrane bottoms, with defined pore sizes. The BBB model was designed with the focus of forming a contact coculture of hBEC lucGFP and NHA dsRed cells on opposing sides of transwell membranes within the Boyden chambers.

3.4.1 Preparation of transwell inserts for seeding of human astrocytes and endothelial cells

Two 24 well plates, each with 12 inserts (as marketed by Nunc, Roskilde, Denmark) were run and treated with the same conditions until the dye permeability assay. Inserts possessing 8 µm pore size membranes were used for the study, based on consultation with literature of *in vitro* BBB model experiments attempted in past studies [185,279].

3.4.2 Coating of transwells

The following reagents mentioned in **Table 3.4** were used for the transwell coating and seeding process.

Table 3.4 Materials for transwell coating and seeding

Reagent Name	**Company**
Coating	
Poly-D-Lysine 0.1 mg/mL	Life Technologies Ltd., NY, USA
Fibronectin 1 mg/mL	Sigma Aldrich, St. Louis, USA
Sterile distilled H_20	
Serum Free Media (DMEM)	(as described for ALT-DMEM in Table 3.1 excluding 10% heat inactivated newborn calf serum)
Seeding	
ALT-DMEM	(as described in Table 3.1)
1X PBS	(as described in Table 3.1)
Trypsin – Versene Mixture (Trypsin EDTA)	Biowhittaker, Walkersville, USA

Poly-D-Lysine solution (Life Technologies Ltd.) was diluted from 0.1 mg/mL stock concentration to 50 µg/mL working solution in 1XPBS prior to use. The basolateral side of the transwell inserts in the culture vessels **(Figure 3.1)** were coated with the working solution of Poly-D-Lysine (75 µL/well). The culture vessel was incubated at room temperature for 1 hr. The Poly-D-Lysine solution was then removed, and the culture surfaces rinsed thrice with sterile distilled water (150 µL/well). Care was taken to ensure the culture vessel was rinsed thoroughly since excess Poly-D-Lysine solution is toxic to cells. The inserts were completely dried prior to the next step.

Fibronectin solution (Sigma Aldrich) was diluted in serum-free growth medium from 1 mg/mL stock solution to 5 µg/cm^2 based on coating protocol for the surface area of the inserts [280], with serum-free growth medium. The apical side of the transwell inserts in the culture vessel were coated with working solution of fibronectin (75 µL/well). The inserts were dried completely under the fume hood overnight. After drying, the inserts were rinsed once with 1XPBS and then allowed to dry in the hood for 1 hr. The culture vessel was then sealed with paraffin film and the vessel stored at 4 ºC, ready for use. **Figure 3.1** illustrates the insert positions and corresponding coating.

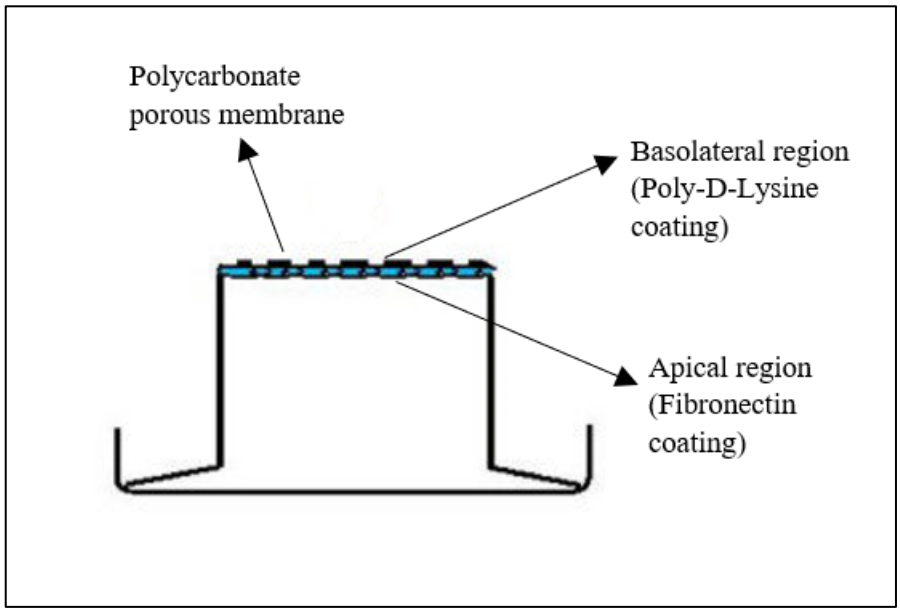

Figure 3.1 Coating of transwell insert membrane in basolateral and apical regions

3.4.3 Seeding of cells in transwell inserts

The inserts were inverted and placed upside down on their corresponding areas on the culture vessel lid. 80 µL of growth medium containing high and low concentrations of NHA dsRed cells **(Table 3.5)** was added to the basal side of the transwell inserts. The plate was placed overtop and the cells adhered for 4 hrs in the incubator at 37 °C, 100% humidity and 5% CO_2. Care was taken to check the inserts periodically and rehydrate with cell growth medium when necessary, to prevent the formation of bubbles when the transwells were flipped back over. After 4 hrs, 500 µL of fresh warm growth medium was introduced to the bottom of the wells. The inserts were carefully inverted right side up in the culture vessel, with the basal and apical regions in their correct positions **(Figure 3.2)**. 500 µL of cell growth medium with hBEC lucGFP cells were then seeded in the inserts. The inserts were incubated at 37 °C, 100% humidity and 5% CO_2. After 24 hrs, the transepithelial electric resistance (TEER) over the inserts were measured.

Table 3.5 Plate map of transwell plate

hBEC lucGFP + Low NHA	hBEC lucGFP + Low NHA	hBEC lucGFP + High NHA	hBEC lucGFP + High NHA	hBEC lucGFP only	hBEC lucGFP only

dsRed	dsRed	dsRed	dsRed		
x	x	x	x	x	x
Low NHA dsRed only	Low NHA dsRed only	High NHA dsRed only	High NHA dsRed only	Blank	Blank
x	x	x	x	x	x

***Cell seeding concentrations – hBEC lucGFP ($2.2x10^5$ cells/mL for $1.1x10^5$ endothelial cells) Low NHA dsRed ($4.4x10^4$ cells/mL for $3.5x10^3$ astrocytes) High NHA dsRed ($6.25x10^5$ cells/mL for $5.0x10^4$ astrocytes)*

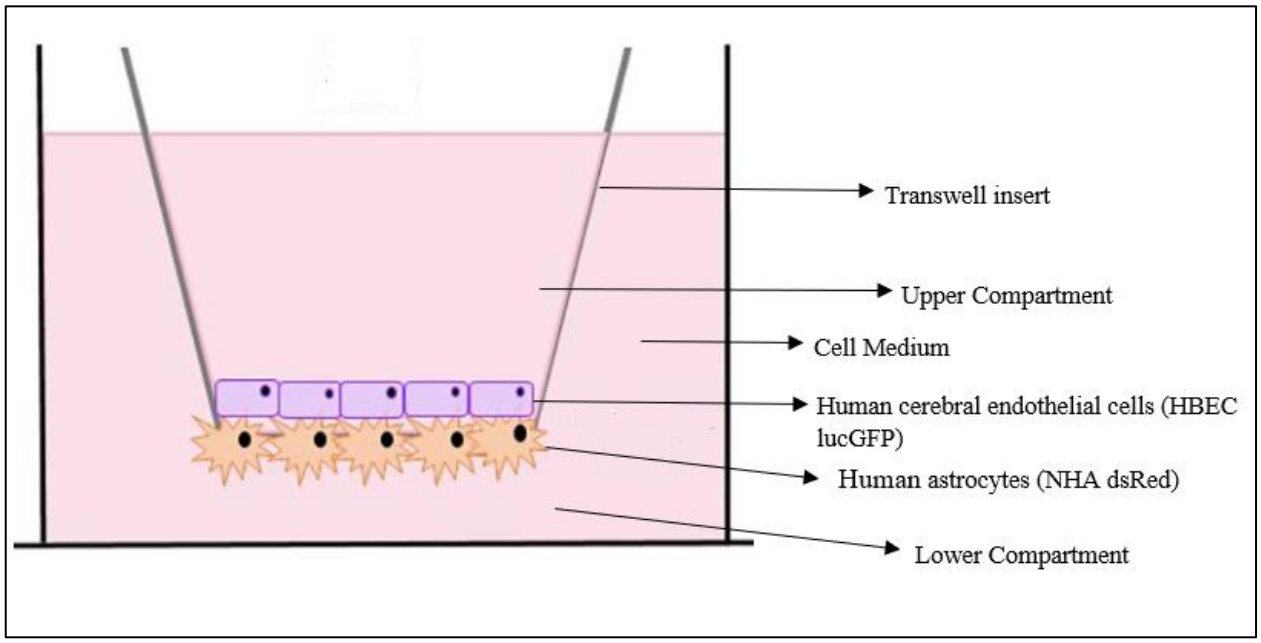

Figure 3.2 Cell seeding positions of hBEC lucGFP and NHA dsRed in transwell insert

3.4.4 Measurement of Transepithelial Electric Resistance (TEER)

Prior to taking TEER measurements, the inserts were transferred to a fresh 12 well plate (Nunc). The inserts were kept in the 12 well plates throughout the duration of the experiments until the dye permeation assay was performed. Measurements were recorded using the EVOM3 instrument (World Precision Instrument, Hertfordshire, UK). The TEER electrodes were first soaked in bleach for 15 mins prior to use. The electrodes were then transferred to sterile MilliQ water for 2 mins before being left to dry. After drying, the electrodes were soaked in 70% EtOH for 2 mins before being left to re-dry. The plate type and name were set in the EVOM3 instrument before each measurement was recorded. Prior to reading, 1 mL of prewarmed growth medium was added to each well in two 12 well plates and labelled appropriately. The cell growth medium in the top of

the inserts was removed and replaced with 500 µL of fresh prewarmed cell growth medium. The inserts were then carefully transferred to the corresponding wells in the 12 well plates (as previously mentioned). The electrodes were soaked for 1 min in cell growth medium before TEER measurement. Measurements were taken every 24 hrs until the barrier resistance values began to significantly decrease. Blank measurements were first taken to prevent unintentional cell transfer via electrodes. Three readings were taken from each well from different positions. After all readings were measured, the values were saved and stored in the EVOM3 system. The culture vessels were then returned to the incubator. Care was taken to ensure that culture plates were not outside the incubator for longer than 20 mins during each counting. Once the readings were taken, electrodes were soaked in MilliQ water and 70% EtOH (for 2 mins each and allowed to dry in between). The probe was then returned to its holder and the EVOM3 was shut down. TEER measurement results were tabled and presented in graphs using GraphPad Prism 8 (GraphPad software, Inc).

3.4.5 FITC dye permeability assay

The dye used for the assay was Fluorescein isothiocyanate (FITC)-dextran (Sigma Aldrich, St. Louis, USA) with molecular weight- 4kDa. The dye was selected upon consultation with literature of classic Transwell chamber FITC assays [281–283]. All steps of the process were carried out in the dark to account for dye photosensitivity. The dye permeability assay was performed on the 7th day of TEER measurement (Day 7) to offer time for barrier formation and repeated 7 days later (Day 14).

3.4.5.1 Preparation of standard curve and sample plate

The FITC-dextran stock solution (2 mg/mL) was diluted in growth medium to 100 µg/mL prior to use. To facilitate sample collection, 500 µL of cell growth medium was added to the bottom of a fresh 24 well plate before transferring the inserts to the plate. The growth medium from the upper chamber of each insert was then replaced with 150 µL of FITC solution (100 µg/mL) and incubated for 2 hr in the dark at 37 °C, 100% humidity and 5% CO_2. To the control plates, 150 µL of cell growth medium was added instead of FITC prior to incubation. Sufficient volumes of FITC dilutions (100 µg/mL, 33.3 µg/mL, 11.1 µg/mL, 3.7 µg/mL and 1.23 µg/mL) were prepared to allow for the generation of a standard curve for sample referencing. The standards were added to a 96 well plate in triplicates of 150 µL each. After incubation, triplicates of samples (150 µL each) were transferred from the lower chamber of each transwell insert to the 96 well plate. Dye

permeability assay results were tabled and presented in graphs using GraphPad Prism 8 (GraphPad software, Inc.).

3.4.5.2 Measurement of dye permeability

The 96 well plate was read at 485 nm excitation and 535 nm emission wavelengths by a plate reader (Victor^{TM} 1420 fluorescence microplate reader, Perkin-Elmer Wallance Inc.). The lamp power was set at 2100 and readings were taken after 1 sec for each sample. The FITC-dextran transmigration across the inserts was calculated as percentage of the total volume added in the upper well of the inserts. Care was taken to rinse the cells gently twice with cell growth medium to remove excess FITC, in cases of the dye assay being repeated.

3.4.6 Cell staining and fixing

Cells on both sides of the inserts were stained at the end of the experiment and fixed for confocal microscopy. Culture medium was first removed from the top and bottom chambers of the transwells and the membranes rinsed twice with sterile 1XPBS. 500 µL of 4% paraformaldehyde (PFA) was added to the top and bottom chambers of the wells and the cells were fixated for 30 mins at room temperature. PFA was then aspirated from both chambers and the inserts were rinsed twice with sterile 1XPBS. Sample plates were stored at 4 ºC with 500 µL 1XPBS in the top and bottom chambers until confocal microscopy was performed.

3.4.7 Confocal imaging of BBB model barriers

Prior to visualization, PBS was gently removed from both chambers and the insert membranes selected for confocal microscopy were carefully cut out using a sterile scalpel blade and placed within microscope coverslips for visualization. Coverslips were mounted on the holder of the Dragonfly 505 confocal spinning disk system (Andor Technologies, Inc.) equipped with a live-cell microscope incubation cage (Okolab) which maintained the observation environment at 37 °C, 100% humidity and 5% CO_2. All images were captured with the iXon 888 Life EMCCD camera within the confocal system. Confocal images were taken at 20x objective and in both X-Y and X-Z planes. NHA dsRed cells were imaged using a 561 nm laser line at 5% intensity, 50 ms exposure time, and a 600 nm filter. hBEC lucGFP cells were imaged using a 488 nm laser line at 5% intensity, 50 ms exposure time, and a 525 nm filter. Z-stack images were taken at a step size of 1 µm. All confocal images were processed using IMARIS 9 image analysis software (Oxford Instruments).

3.5 Transmigration of MBM cell line across BBB model

Prior to assessing the transmigratory capacity of H1_DL2 cells across the BBB model, the barrier possessing the highest resistance (based on TEER measurement results) was introduced into the membrane inserts of a fresh 24 well plate (Nunc). hCMEC/D3 cells were seeded in place of hBEC lucGFP cells to facilitate H1_DL2 cell counting at the end of the experiment. The insert membranes possessed the same pore size (8 μm) as used in the previous experiments to maintain the characteristics of the BBB model. Control membrane inserts were also included with absence of BBB model layer. H1_DL2 cells were starved with serum free ALT-DMEM for 12 hrs prior to seeding in the membrane inserts. During the timepoint of highest barrier resistance (as determined by the TEER experiment), 4 seeding densities of serum starved H1_DL2 cells (5×10^3, 1×10^4, 5×10^4 and 1×10^5 H1DL2 cells), each in 400 μL final volume, were seeded in the upper compartments of transwell inserts. 500 μL of ALT DMEM was added to the lower compartment of the inserts to serve as the chemoattractant. **Figure 3.3** illustrates the transmigration assay setup. The plate was incubated for 24 hrs to allow for H1_DL2 migration across the BBB model and control inserts. After 24 hrs, serum free ALT DMEM and ALT DMEM were removed from both compartments and the cells were fixed by 4% PFA for 15 mins at room temperature. The PFA was then gently aspirated and the transwell inserts were washed twice with sterile 1XPBS to remove PFA excess and non-attached cells. The cells were then stained by incubation of the transwell inserts with Hoechst medium solution (of final concentration 10 μg/mL) for 15 mins at room temperature, protected from light. Following this, the inserts were washed twice with sterile 1XPBS to avoid drying of membrane. Non-migrated H1_DL2 cells in the upper compartment of the insert membranes were carefully removed by gentle scrapping with cotton swabs. The membranes of each insert were then cut out using sterile scalpel blade and placed bottom facing up in microscope coverslips for confocal evaluation. The coverslips were mounted in the confocal microscope (Andor Technologies, Inc.) and the number of migrated H1_DL2 cells counted by evaluation of 10x images taken of the membrane. The results were calculated and presented in graphs of relative percentages.

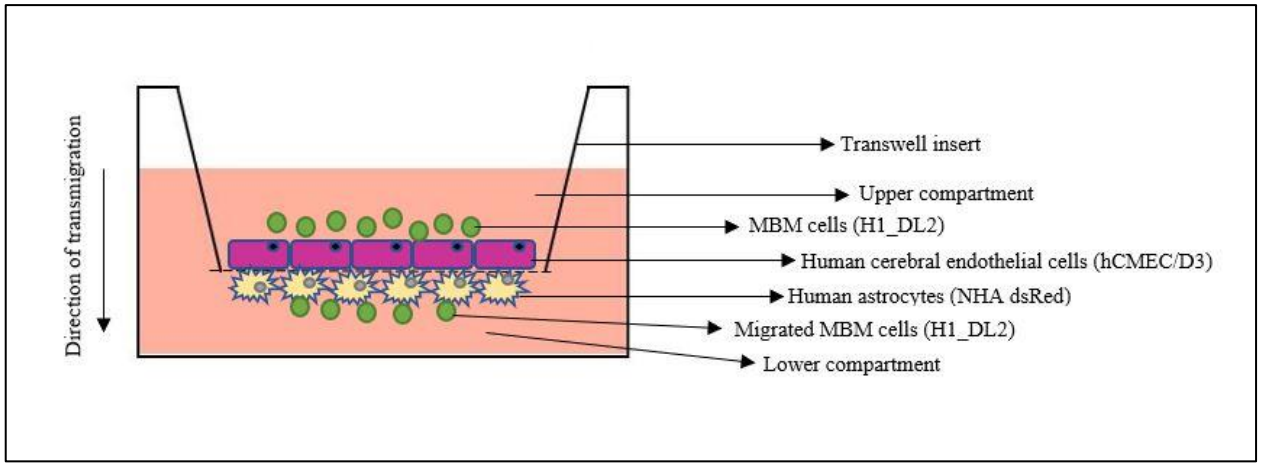

Figure 3.3 Transmigration assay setup using the established BBB model. The upper compartment possesses serum free ALT DMEM. The lower compartment possesses ALT DMEM as the chemoattractant

4. Results

4.1 All Cell Lines expressed Strong Fluorescent Protein Expression and Distinct Morphology

Cell lines were cultured in ALT-DMEM and live cell images of untreated cells for all three tagged cell lines was obtained. All the images were captured while using the 10X and 20x objectives **(Figure 4.1)**.

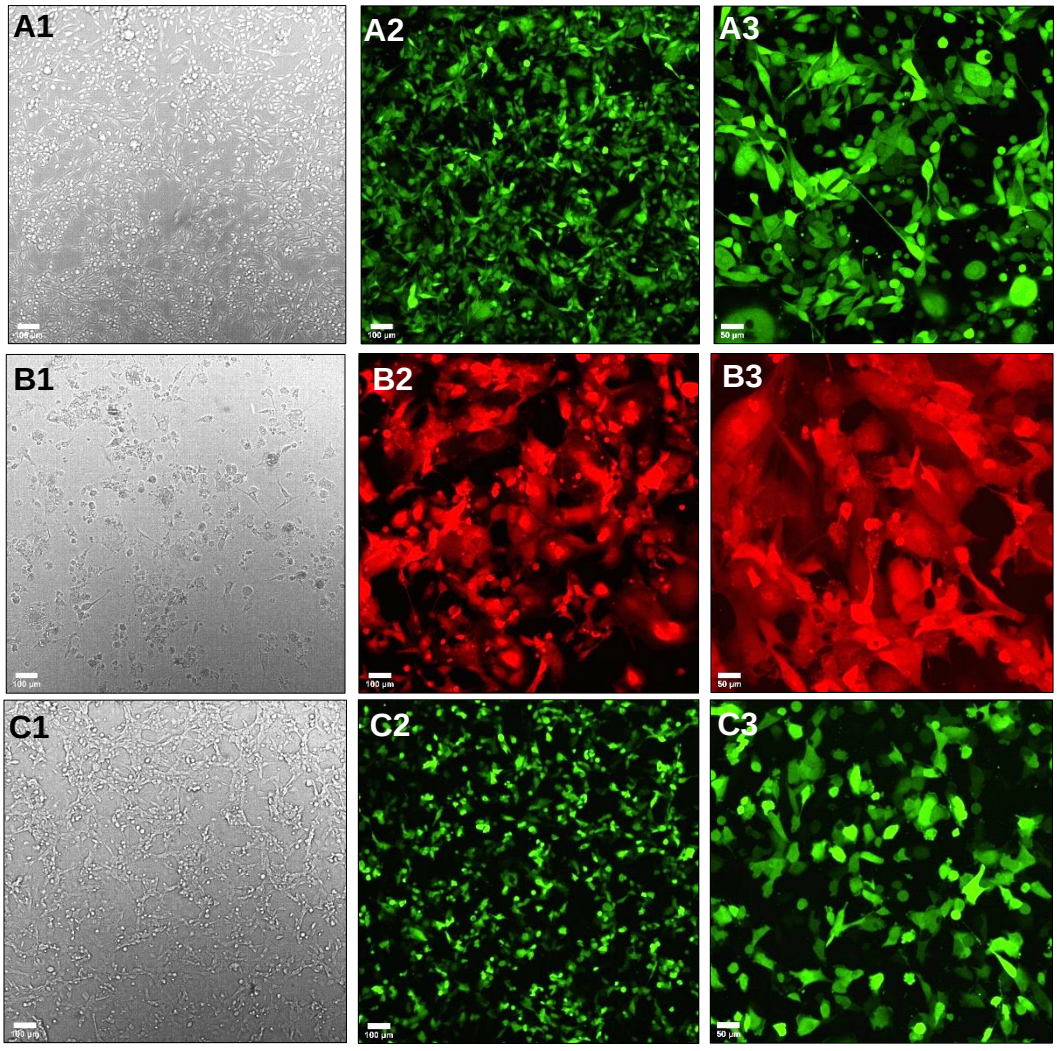

Figure 4.1 Confocal images of untreated cell lines H1_DL2 (A), NHA dsRed (B) and hBEC lucGFP (C) using brightfield 10x (A1, B1, C1), fluorescence microscopy 10x (A2, B2, C2) and fluorescence microscopy 20x (A3, B3, C3). All images taken at 60-70% cell culture confluency Scale bar: 100 µm (10x) 50µm (20x)

Confocal images of cell lines **(Figure 4.1)** showed that the green fluorescence protein was functioning well in staining of both the H1_DL2 and hBEC lucGFP cell lines. Similar pictures were taken for the NHA dsRed cell lines with red protein fluorescence, and confirmed that the red fluorescence protein functioned as expected. The strong fluorescence obtained from all three cell lines indicated successful cell sorting of high fluorescent protein expression.

Cell morphologically, the majority of H1_DL2 cells appeared triangular and elongated fusiform with cell bodies either independent or in attachment with neighboring cells. Some of the cells were more rounded, possibly indicating start of mitosis, while all cells tended to grow in monolayer adherent patches.

The cell morphology of NHA dsRed cells revealed dense multipolar epithelial morphology with low stratification. The majority of the cells proliferated in thick adherent clusters with thick cytoplasmic extensions between clusters, and were highly distributed in all regions of the surface of the chamber well.

Regarding the hBEC lucGFP cells, they showed spindle-shaped, elongated morphology characteristic of brain endothelial cells and non-overlapping cell growth upon formation of confluent monolayers.

4.2 Equivalent Ratio (1:1) of 5 x 10^4 H1_DL2 and NHA dsRed yields Well-spaced, Uniform Growth Distribution of Cells, optimal for 8-36 hrs of Confocal Visualization of TNTs

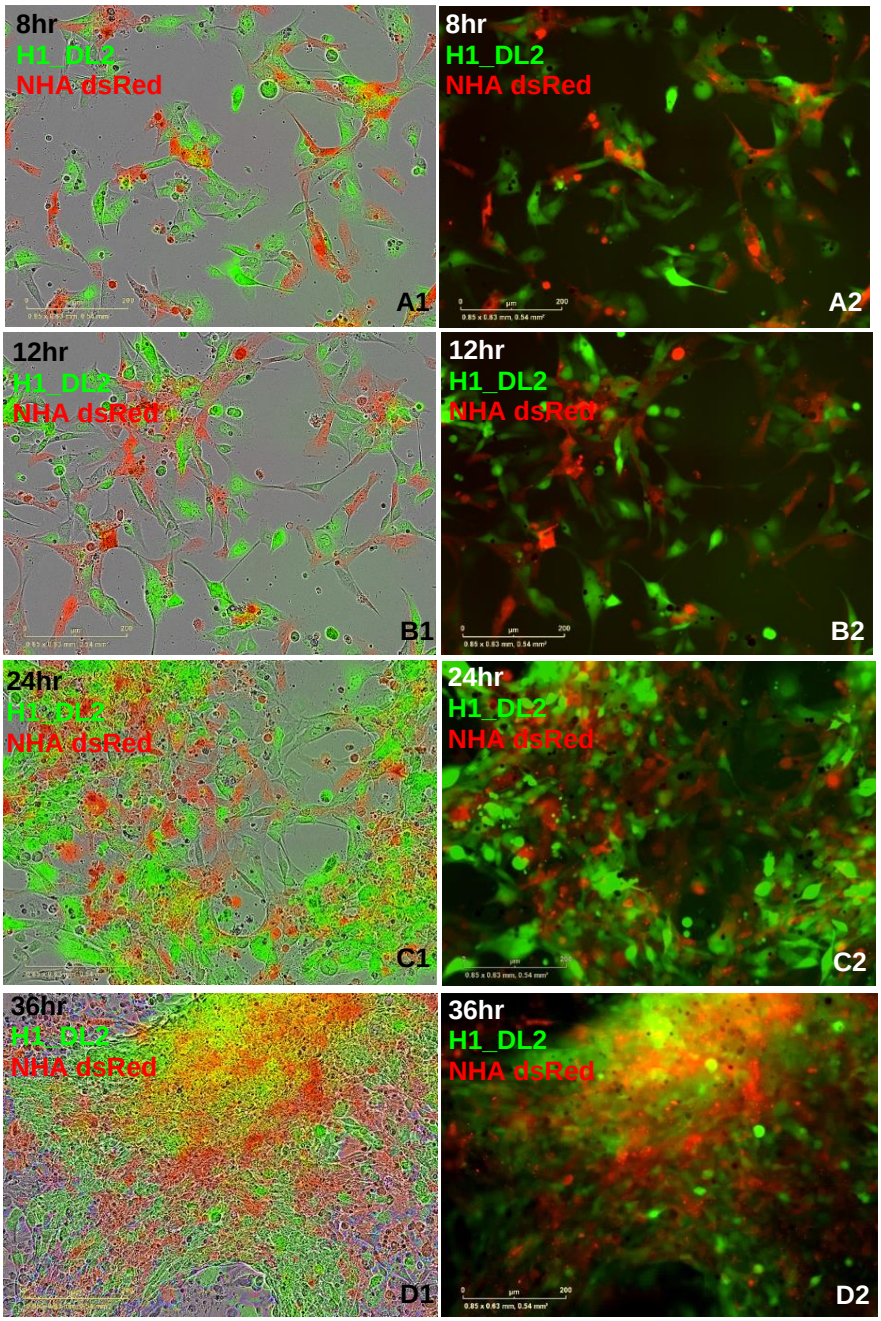

Figure 4.2 IncuCyte images of H1_DL2 and NHA dsRed cocultures (cell seeding densities of 5 x 10^4 in a 1:1 ratio) obtained across 4 timepoints (8 hr,12 hr,24 hr and 36 hr). Phase contrast images (A1, B1, C1, D1) and non-phase contrast images utilizing both green and red fluorescence channels (A2, B2, C2, D2). Phase contrast images were taken using 5% spectral unmixing (Basic Analyzer software module, Essen BioScience Ltd.) to better represent distribution of GFP and RFP fluorophores. Scale bar: 200 µm. The experiment was repeated 3 times with the most representative images presented.

IncuCyte evaluation revealed that a cell seeding density of 5 x 10^4 H1_DL2 and 5 x 10^4 NHA dsRed cells provided a suitable degree of cell confluency within the field of view, uniform distribution of cells within the coculture monolayer plane and optimal frequency of visible cellular interactions at an optimal timepoint range of 8-36 hrs. As observed in the images, both cell populations began to initiate visible cytoplasmic interactions at around 8 hrs post seeding (approximately 40% coculture confluency). At 12 hrs, there was a greater frequency of visible cytoplasmic interactions between both cell populations (approximately 50% coculture confluency), higher cell distribution and absence of clumping and aggregate formation. At 24 hrs, images revealed a time proportional rise in the number of cytoplasmic interactions and a greater uniformity of coculture distribution (approximately 80% coculture confluency). Furthermore, there was the detection of narrow cytoplasmic extensions between cell populations, especially in regions with lower cell distribution. A small degree of astrocyte clumping could also be visualized at this timepoint. At 36 hrs, images revealed high coculture confluency across the field of view, with reduced frequency of visible interactions between cell populations. There was a high degree of clumping and aggregate formation at this timepoint with high visibility of cell growth above the adherent coculture monolayer. This was also indicated by the increase in fluorescence.

4.3 H1_DL2 and NHA dsRed initiate Homotypic and Heterotypic TNT Interactions in Coculture

TNT interactions were first visualized on the 40x objective during the 8th hr of the experiment, and then progressively detected during the 24th and 33rd hrs time points **(Figures 4.3,4.4,4.5)**. Visualization was followed by quantification of TNTs (as described in **Section 3.3.4**) and the results were graphed **(Figure 4.6)**.

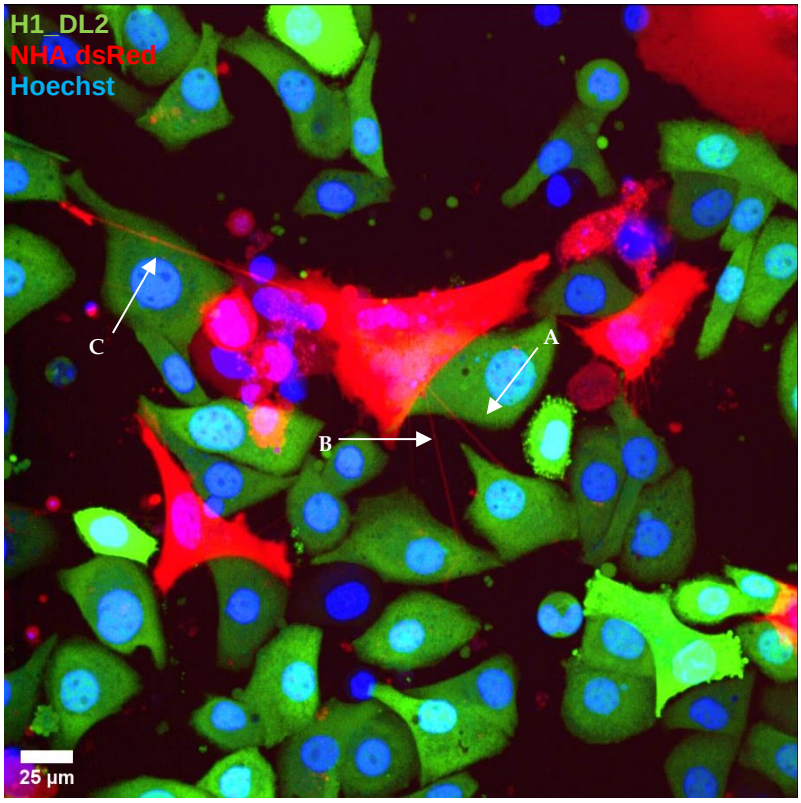

Figure 4.3 Visualization of TNT interactions between H1_DL2 and NHA dsRed at the 8th hr using the 40x objective. *A, B and C indicate 3 heterotypic TNT interactions between NHA dsRed cells (centre) and surrounding H1_DL2 cells.* Width measurements – A (0.437 µm), B (0.572 µm) and C (0.671 µm) Scale bar: 25 µm

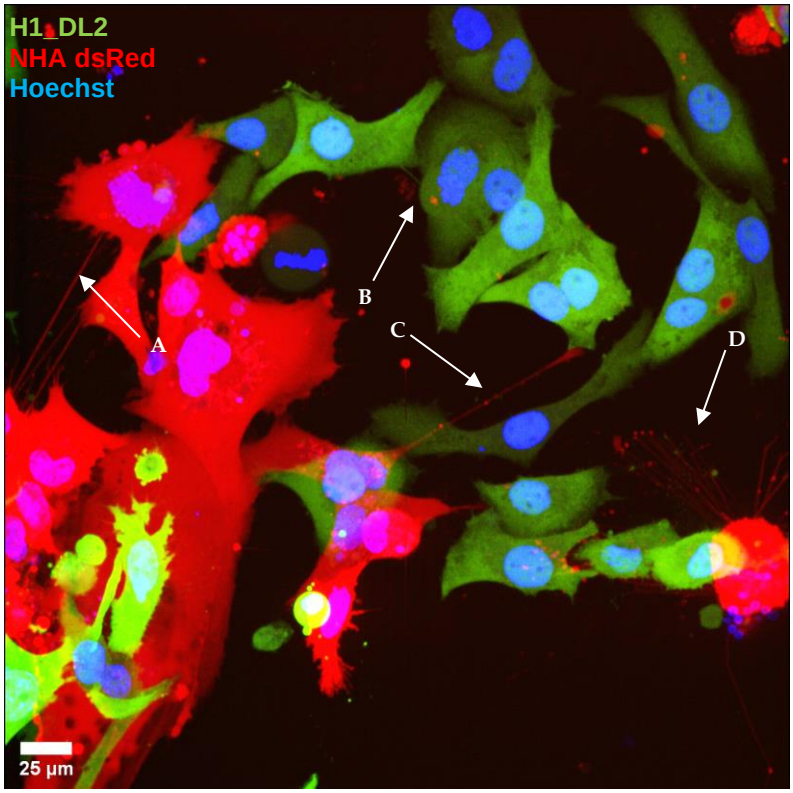

Figure 4.4 Visualization of TNT interactions between H1_DL2 and NHA dsRed at the 24th hr using the 40x objective. *A indicates homotypic TNT interactions between 2 groups of NHA dsRed cells. B indicates a homotypic TNT interaction between 2 H1_DL2 cells. C indicates a heterotypic TNT interaction between a NHA dsRed cell and an H1_DL2 cell. D indicates a cluster of TNTs released by a NHA dsRed cell* Scale bar: 25 µm

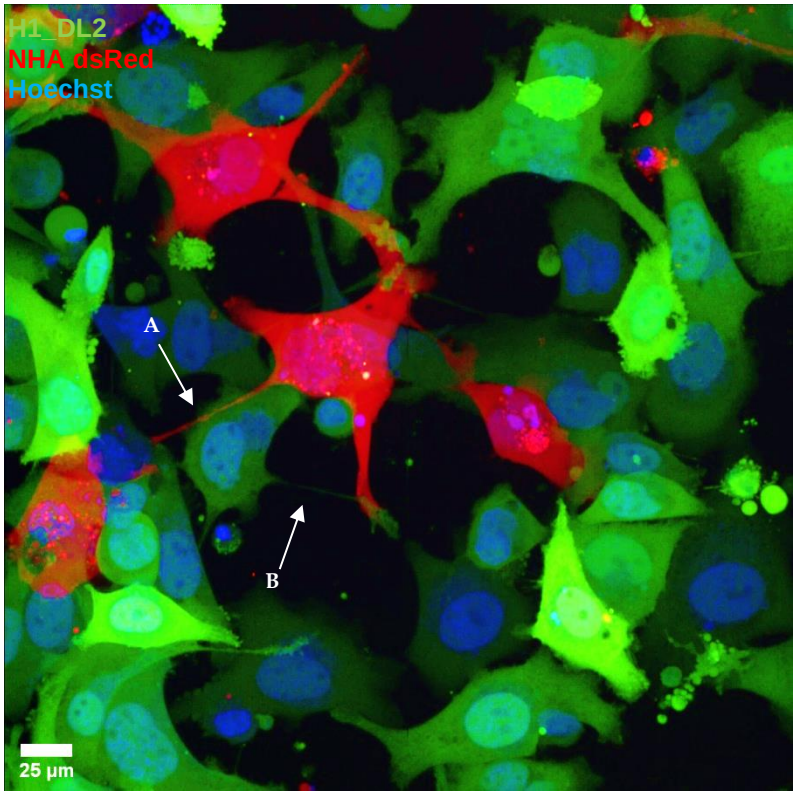

Figure 4.5 Visualization of TNT interactions between H1_DL2 and NHA dsRed at the 33rd hr using the 40x objective. *A indicates a heterotypic TNT interaction extending from a NHA dsRed to a H1_DL2 cell. B indicates a heterotypic TNT interaction extending from an H1_DL2 cell to a NHA dsRed cell.* Scale bar: 25 µm

Confocal visualization revealed both homotypic and heterotypic TNT interactions between H1_DL2 and NHA dsRed cells at the 8th hr of the study **(Figure 4.3)**. TNTs visualized were less than 1 µm, and were clearly seen to travel over the substratum of the coculture to connect with other cells. Development of TNTs were more frequent at the 24th hr (**Figure 4.4)**, with a higher frequency of TNTs from both H1_DL2 and NHA dsRed cells. Formation of TNT "clusters" were also detected during observation at this time point, emerging from both H1_DL2 and NHA dsRed cells but they were not included in the quantification process if they did not meet the TNT parameter of membrane continuity between two cells. The highest frequencies of homotypic and heterotypic TNT interactions were visualized at the 33rd hr **(Figure 4.5)** from both H1_DL2 and NHA dsRed cells. Slight alterations in cell morphologies were also detected at this timepoint, possibly indicating cell senescence. The majority of homotypic and heterotypic TNT interactions visualized at all 3 timepoints were seen to be initiated by NHA dsRed cells. This was later confirmed in the TNT quantification analyses (described in **Section 4.3.1**). Confocal visualization of the cocultures also confirmed successful Hoechst staining of cell nucleic acids, due to the clear detection of viable H1_DL2 and NHA dsRed cell nuclei which were visible as large blue dots in the images.

4.3.1 NHA dsRed initiates higher relative percentage of homotypic and heterotypic TNT interactions in untreated H1_DL2 and NHA dsRed cocultures

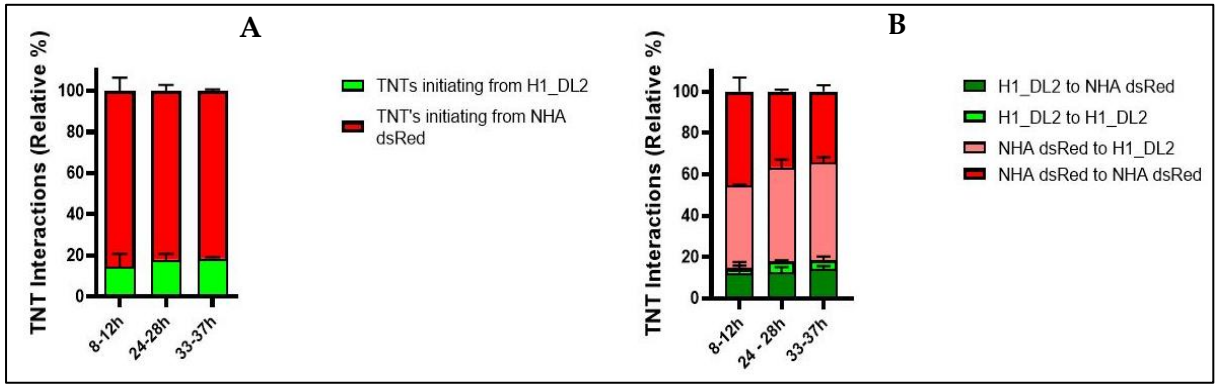

Figure 4.6 Quantification of TNT interactions between H1_DL2 and NHA dsRed during the 8 hr, 24 hr and 33 hr timepoints of the study. A) Illustration of relative percentages of TNTs initiating

from H1_DL2 and NHA dsRed cells over 3 time points of the study. B) Illustration of relative percentages of homotypic and heterotypic TNT interactions between H1_DL2 and NHA dsRed cells over 3 time points of the study. The experiment was carried out 2 times with the most representative results presented.

The quantification of TNT interactions between H1_DL2 and NHA d.sRed during the 8th, 24th and 33rd hrs of the study is shown in **Figure 4.6**. Quantification was carried out in two areas – the relative percentages of TNT interactions initiating from H1_DL2 and NHA dsRed cells over 3 time points of the study and the relative percentages of homotypic and heterotypic TNT interactions between H1_DL2 and NHA dsRed cells over 3 time points of the study. Quantification results revealed a higher percentage of TNT interactions initiating from NHA dsRed cells across all 3 timepoints of the study (81 – 85%), compared to H1_DL2. The relative percentage of TNTs initiated by H1_DL2 stayed relatively constant through all 3 time points of the study (15 – 18%). The relative percentage of heterotypic TNT interactions by NHA dsRed increased noticeably between the 8th and 24th hrs of the study (from 38 to 46%), opposed to homotypic TNT interactions by NHA dsRed during the same time period. Furthermore, H1_DL2 cells exhibited a slight increase in homotypic interactions between the 8th and 24th hrs (from 2 to 8%).

4.4 H1_DL2 initiates Higher Frequency of Homotypic and Heterotypic TNT Interactions at Increasing Vemurafenib Concentrations

Vemurafenib (0.5, 0.8, 1 and 1.5 μM) were added to the coculture systems of H1_DL2 and NHA dsRed 2 hrs prior to confocal visualization and drug effect on homotypic and heterotypic TNT interactions between both cell populations was quantitatively and qualitatively evaluated at the 8th, 24th and 33rd hrs. The confocal visualizations of the TNT model across all 4 drug concentrations during the 33rd hr timepoint is shown below **(Figures 4.7, 4.8,4.9,4.10).**

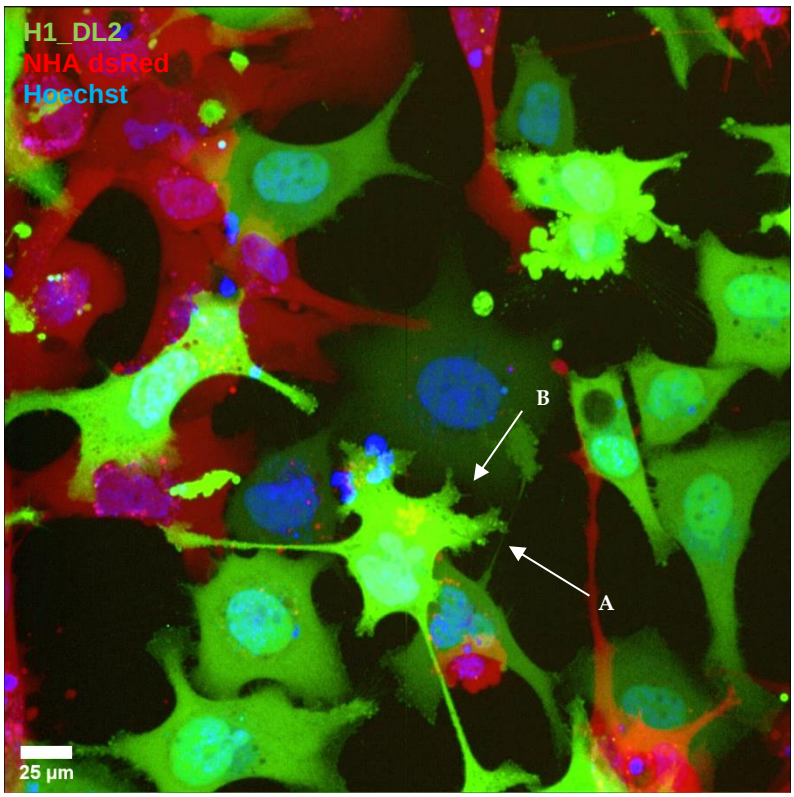

Figure 4.7 Visualization of TNT interactions between H1_DL2 and NHA dsRed at the 33rd hr in the presence of 0.5 µM vemurafenib. Images captured on 40x objective. *A indicates a homotypic TNT interaction extending from a H1_DL2 to a H1_DL2 cell. B indicates the slightly altered morphology of H1_DL2 cells from smooth to rough edged multipolar cells.* Scale bar: 25 µm

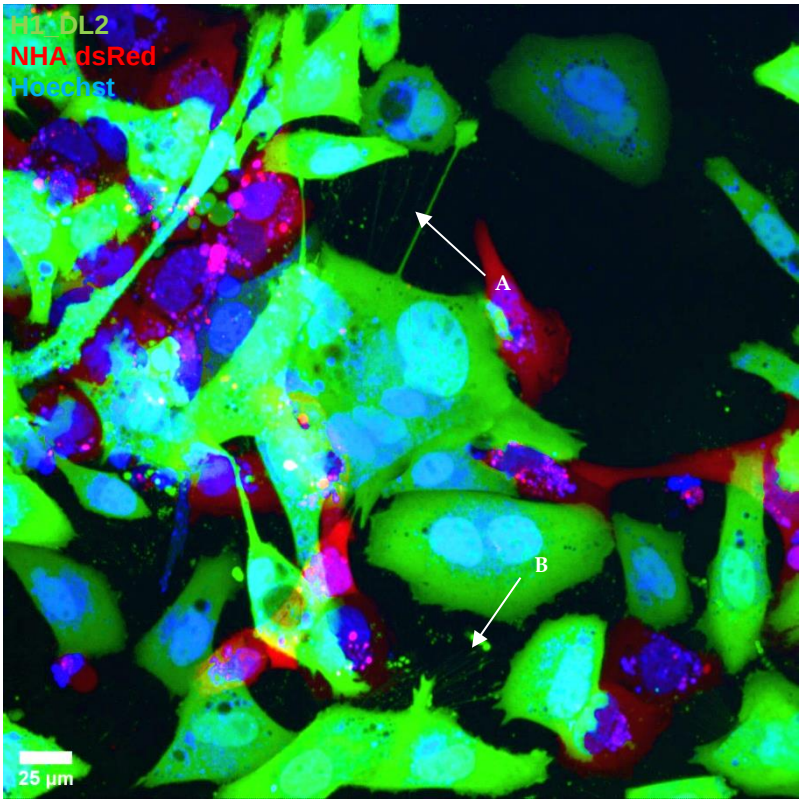

Figure 4.8 Visualization of TNT interactions between H1_DL2 and NHA dsRed at the 33rd hr in the presence of 0.8 µM vemurafenib. Images captured on 40x objective. *A indicates homotypic TNT interactions extending from a H1_DL2 to neighboring H1_DL2 cells. B indicates the presence of cell debris and TNT clusters being released from H1_DL2 cell.* Scale bar: 25 µm

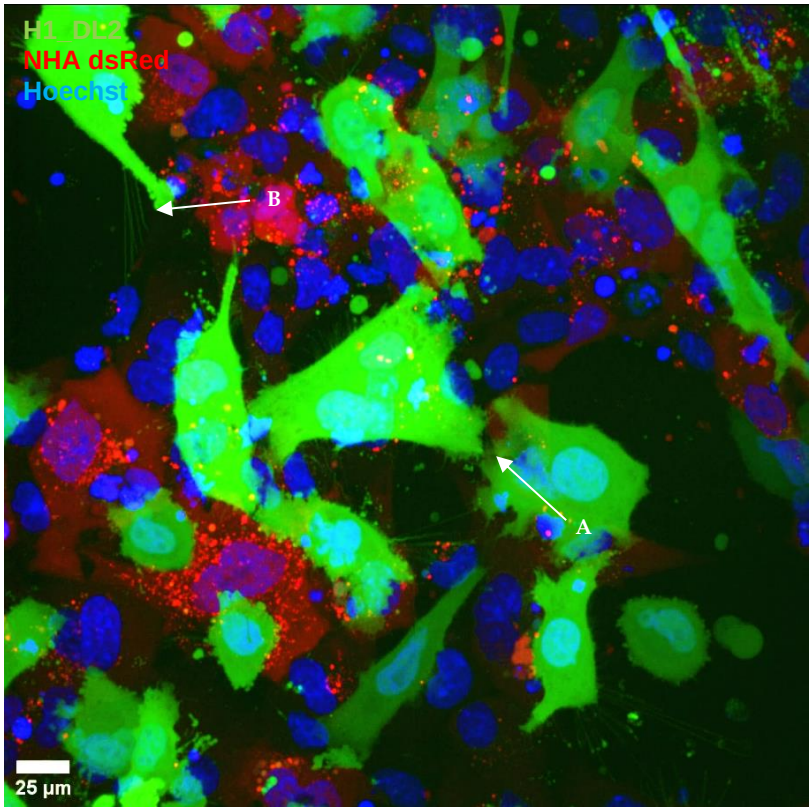

Figure 4.9 Visualization of TNT interactions between H1_DL2 and NHA dsRed at the 33rd hr in the presence of 1 µM vemurafenib. Images captured on 40x objective. *A indicates altered morphology of H1_DL2 cells with rough edges and granular membranes. B indicates extension of TNT clusters from H1_DL2 cell to NHA dsRed cells in the substratum.* Scale bar: 25 µm

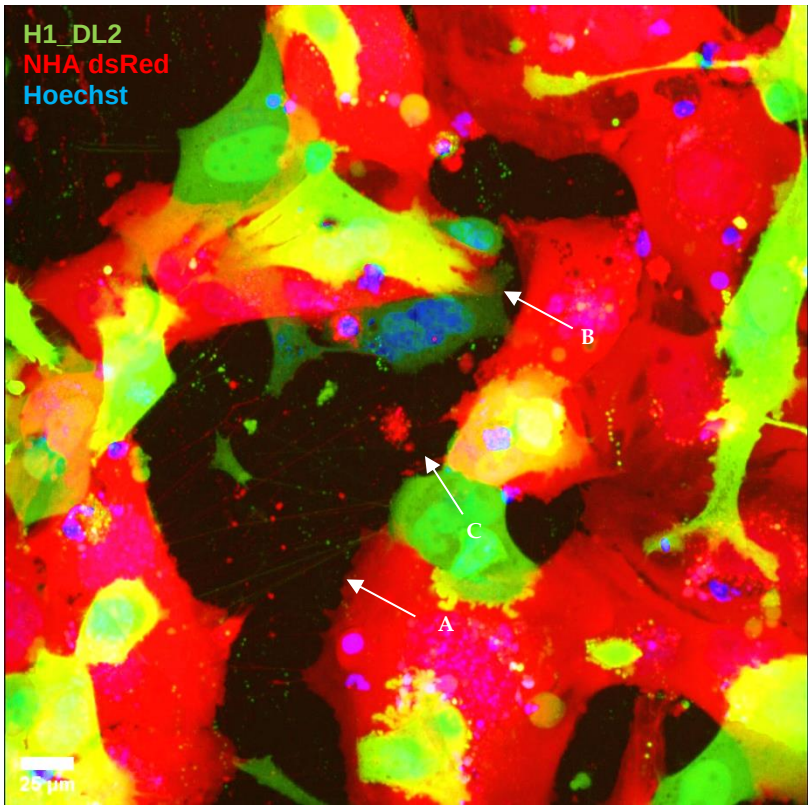

Figure 4.10 Visualization of TNT interactions between H1_DL2 and NHA dsRed at the 33rd hr in the presence of 1.5 µM vemurafenib. Images captured on 40x objective. *A indicates network of TNT interactions extending from both H1_DL2 and NHA dsRed cells. B indicates morphological alteration of H1_DL2 cells which now possess flattened granular membranes with lack of fusiform morphology. C indicates presence of cell debris from both cell types* Scale bar: 25 µm

Confocal visualization of the TNT model upon exposure to 0.5 µM vemurafenib **(Figure 4.7)** showed high frequency of homotypic and heterotypic TNT interactions between H1_DL2 and NHA dsRed cells. H1_DL2 cells exhibited slightly altered morphology from classic fusiform to flattened. Small amounts of nonadherent H1_DL2 cells and cell debris were also detected at this drug concentration. Confocal visualization of the TNT model upon exposure to 0.8 µM vemurafenib **(Figure 4.8)** showed larger amounts of floating non adherent cells, as well as increase in morphology alterations in larger populations of H1_DL2 cells, which exhibited flattened granular membranes. Morphological analyses of H1_DL2 cells also revealed distinct features of senescence induced by vemurafenib. A higher frequency of H1_DL2 initiated TNT interactions were also visible in the fields of view, as well as increased amounts of TNT clusters extending from H1_DL2 cells. Confocal visualization of the TNT model upon exposure to 1 µM vemurafenib

(Figure 4.9) showed reduced cell density of H1_DL2 cells and large amounts of floating cell debris. Higher number of TNT interactions by H1_DL2 cells compared to those of NHA dsRed cells were visualized in all fields of view. H1_DL2 cells also exhibited distinct shrinkage in cell morphology and non-adherence characteristic of apoptosis. High degree of senescence was also exhibited, with presence of distinct mechanotransducive stretching in several H1_DL2 cells. No alterations in cell morphology were detected in NHA dsRed cells, and cells maintained their multipolar epithelial morphology. Confocal visualization of the TNT model upon exposure to 1.5 µM vemurafenib **(Figure 4.10)** showed low density of H1_DL2 cells and large degree of H1_DL2 cell apoptosis. Adherent H1_DL2 cells were flat with granular membranes, with few visible spindle shaped appendages. High frequency of homotypic and heterotypic TNT initiations was detected from H1_DL2 cells. NHA dsRed cells exhibited slightly altered morphology, possibly due to initiation of cell senescence. Both cell populations exhibited emergence of TNT clusters on their cell surfaces. Large amounts of cell debris of both H1_DL2 and NHA dsRed cells were also apparent in all fields of view.

4.4.1 H1_DL2 initiates higher relative percentage of TNT interactions with increasing drug concentrations

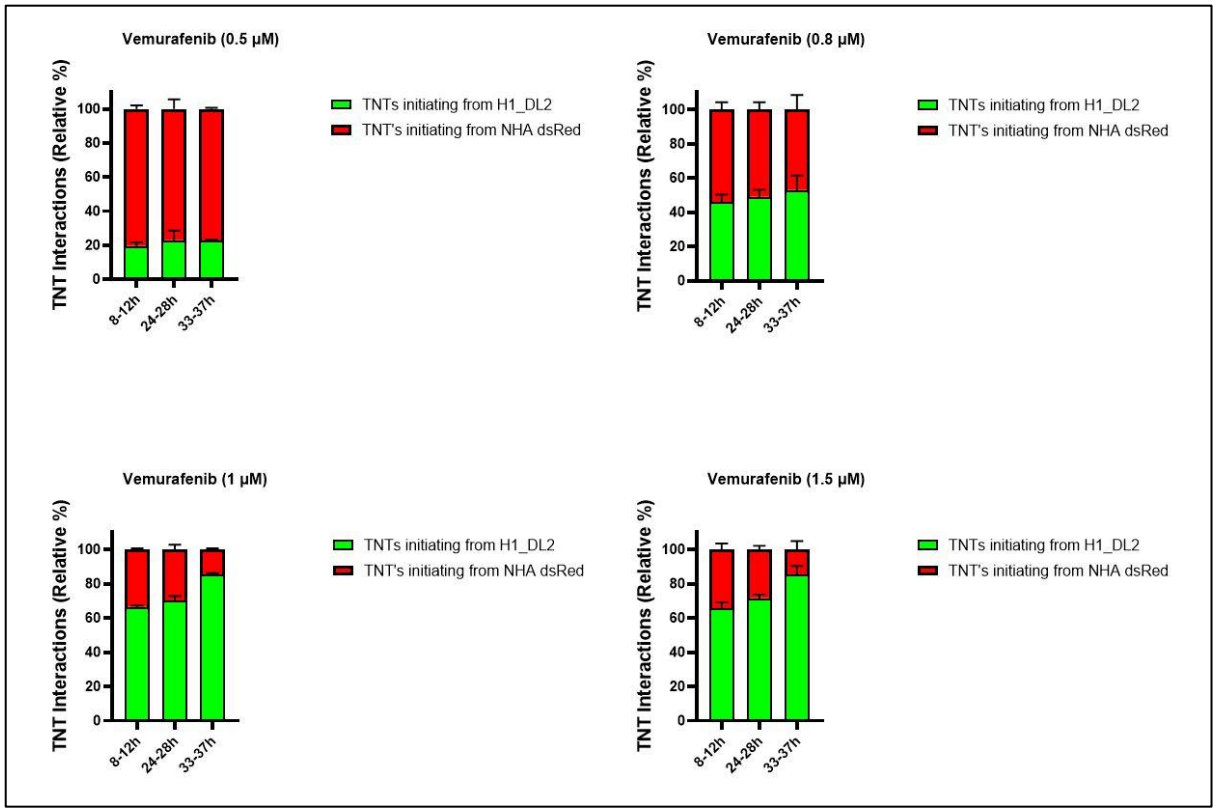

Figure 4.11 Quantification of TNT interactions between H1_DL2 and NHA dsRed during the 8

hr, 24 hr and 33 hr timepoints of the study across selected vemurafenib drug concentrations (0.5 μM, 0.8 μM, 1 μM and 1.5 μM). The experiment was carried out 2 times with the most representative results presented.

The quantification of TNT interactions between H1_DL2 and NHA dsRed across selected vemurafenib drug concentrations during the 8th, 24th and 33rd hrs of the study is shown in **Figure 4.11**. Quantification results of TNT interactions initiating from H1_DL2 and NHA dsRed revealed an increasing relative percentage of TNT interactions initiated by H1_DL2 across all 3 timepoints of the study with increasing drug concentrations. This increase was most pronounced across 0.5 – 1 μM vemurafenib drug exposure (from around 22-74%). The relative percentage of TNT interactions initiated by NHA dsRed decreased across increasing drug concentration exposure and stayed relatively constant across 1-1.5 μM vemurafenib drug exposure. The relative percentage of TNT interactions initiated by NHA dsRed was the highest (78%) at the lowest vemurafenib drug concentration (0.5 μM) across all 3 timepoints of the study.

4.4.2 H1_DL2 initiates increasing relative percentage of heterotypic TNT interactions with NHA dsRed at increasing drug concentrations across all 3 timepoints of the study.

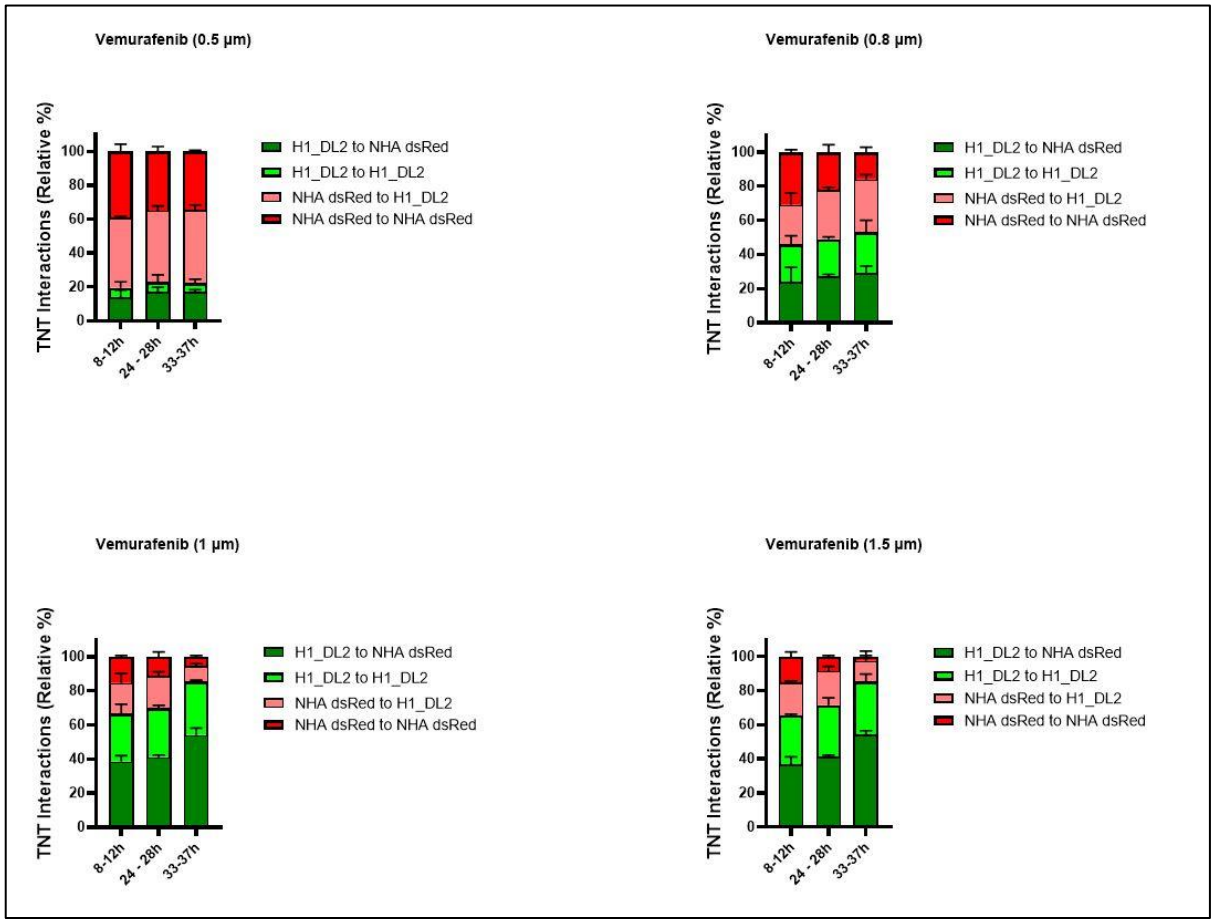

Figure 4.12 Quantification of homotypic and heterotypic TNT interactions between H1_DL2 and NHA dsRed during the 8 hr, 24 hr and 33 hr timepoints of the study across selected vemurafenib drug concentrations (0.5 µM, 0.8 µM, 1 µM and 1.5 µM). The experiment was carried out 2 times with the most representative results presented.

The quantification of homotypic and heterotypic TNT interactions between H1_DL2 and NHA dsRed across selected vemurafenib drug concentrations during the 8th, 24th and 33rd hrs of the study is shown in **Figure 4.12**. Quantification results showed an increase in the relative percentage of H1_DL2 initiated heterotypic TNT interactions (between H1_DL2 and NHA dsRed) with increasing drug concentrations (from around 16 – 44%). While the relative percentage of H1_DL2 initiated TNT interactions strongly increased with increasing drug concentrations, a higher majority of these interactions were found to be heterotypic, and most pronounced in the range of 0.8 – 1.5 µM vemurafenib drug exposure. The relative percentage of H1_DL2 initiated homotypic TNT interactions was also higher with increasing drug concentrations and across all 3 timepoints

of the study. There was a negligible difference in the relative percentage distribution of homotypic and heterotypic TNT interactions between H1_DL2 and NHA dsRed across 1-1.5 μM vemurafenib drug exposure.

4.5 hBEC luc GFP and High Seeding Density of NHA dsRed forms Acceptable BBB Model for a period of 48 hrs

hBEC lucGFP and concentrations of NHA dsRed were seeded in transwell inserts (as described in Section 3.4) and the TEER and FITC dye permeability of the resulting barrier formations were evaluated over a period of 14 days. The results are tabled and presented as graphs **(Figures 4.13A, 4.13B, 4.14)**.

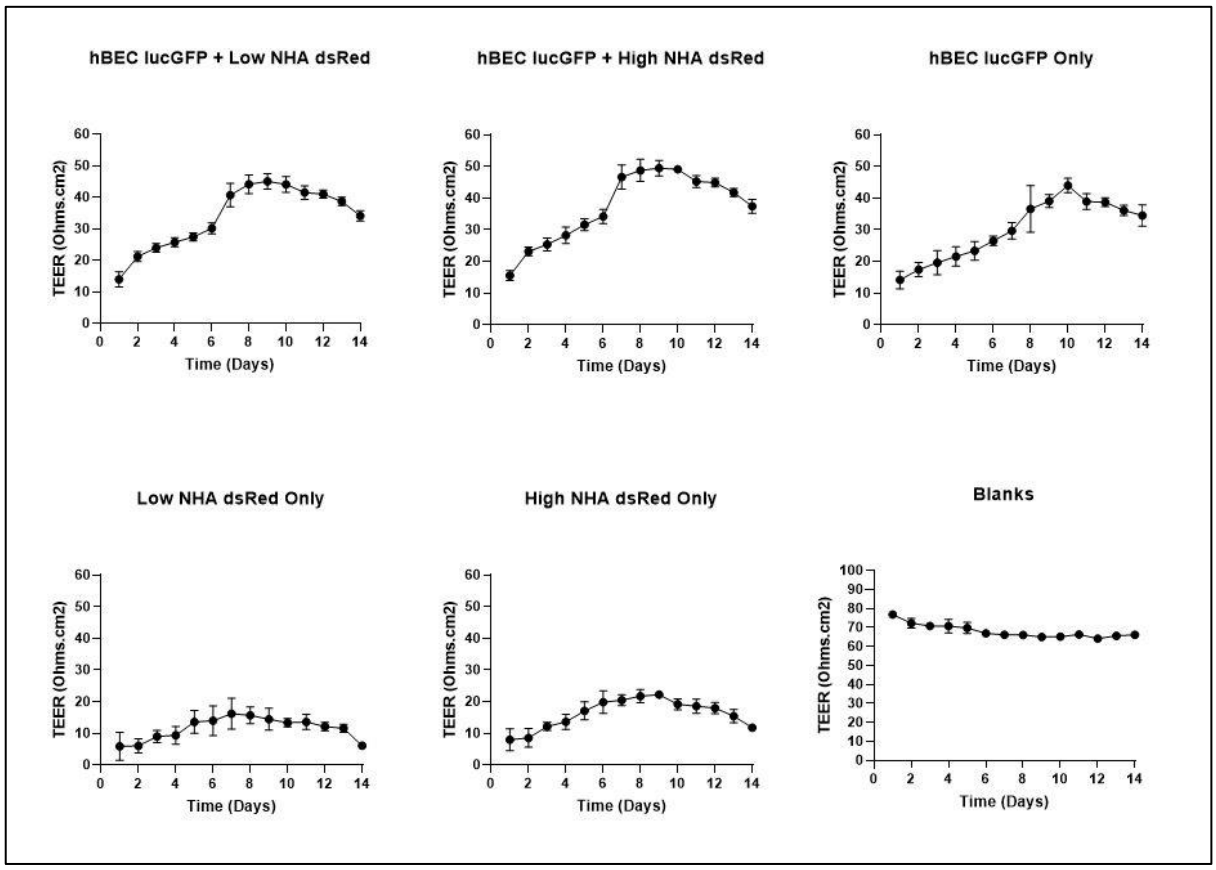

Figure 4.13A TEER measurements of individual BBB model barriers over 14 days.

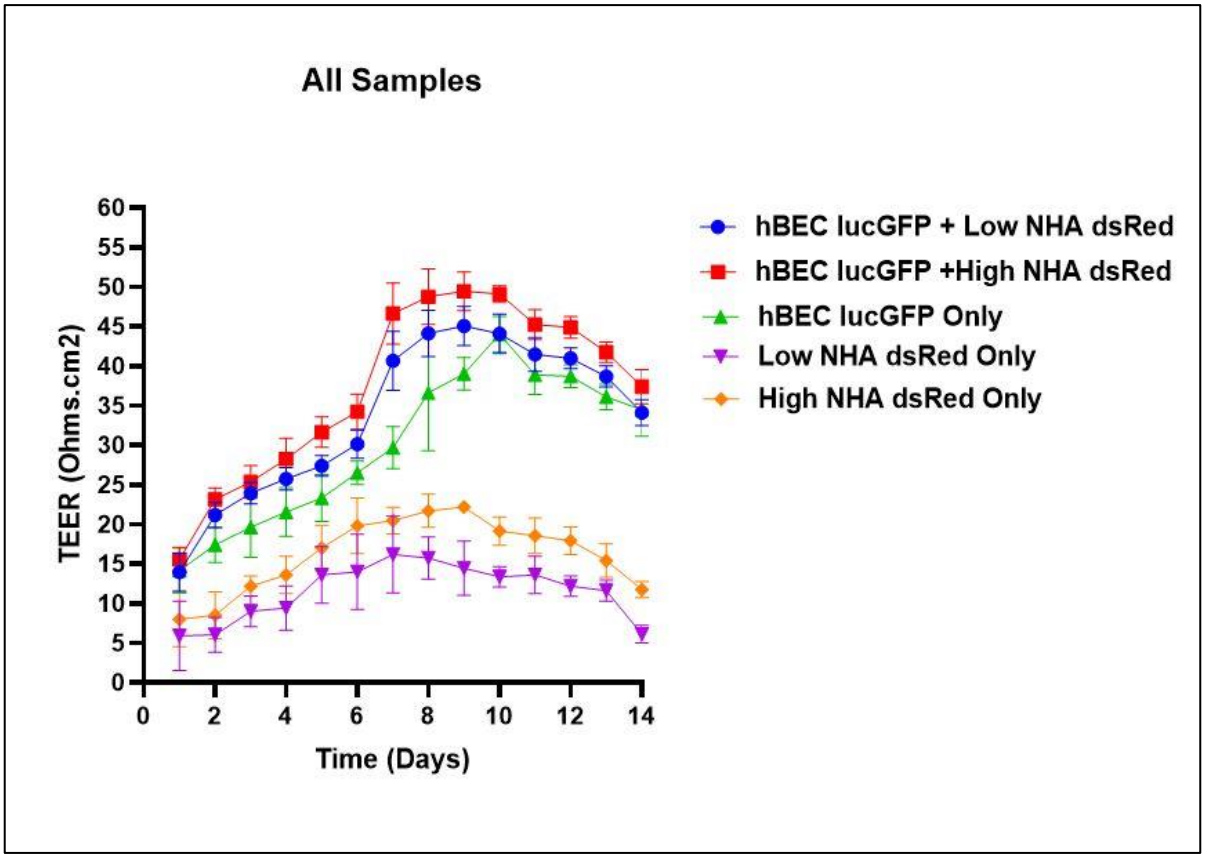

Figure 4.13B Comparison of TEER measurements in all BBB model barriers over 14 days

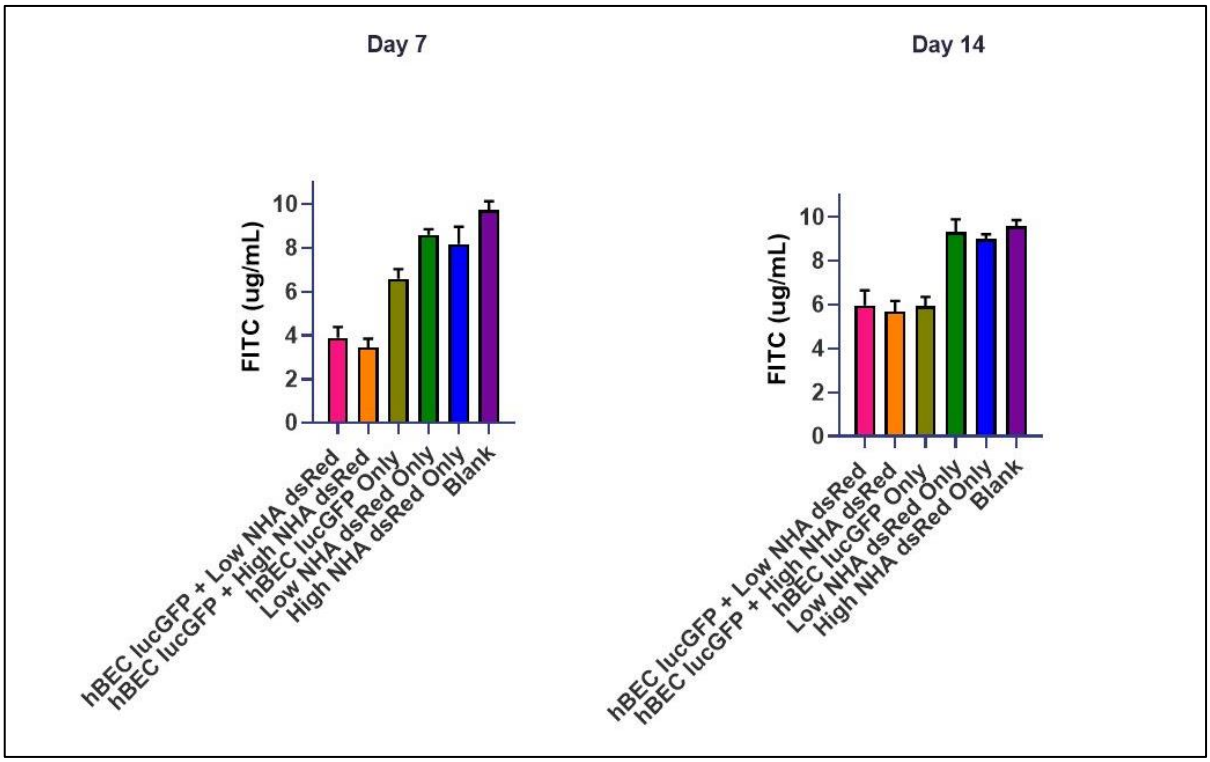

Figure 4.14 Results of FITC dye permeability assays conducted on Day 7 and Day 14 of the study

TEER measurements were taken every 24 hrs until the barrier resistance values began to decrease significantly. As seen in **Figures 4.13A** and **4.14B**, the barrier composed of hBEC lucGFP and high NHA dsRed exhibited the highest TEER values (about 50 Ohms.cm^2) over the period of 14 days. The TEER of the barrier remained relatively consistent from Day 8 to Day 10 of the study, which indicated its optimal use as an acceptable BBB model for 48 hrs. The barrier composed of hBEC lucGFP and low NHA dsRed exhibited the 2nd highest TEER values (about 45 Ohms.cm^2) over the period of the study, and indicated a positive correlation between the seeding densities of NHA dsRed in association with hBEC lucGFP and barrier strength. The barrier composed of hBEC lucGFP only exhibited TEER values at a maximum of 42 Ohms.cm^2. In contrast, the barriers composed of high NHA dsRed only and low NHA dsRed only exhibited maximum TEER values of 20 and 15 Ohms.cm^2. This indicated that majority of the resistance provided by the hBEC lucGFP and high NHA dsRed barrier were due to hBEC lucGFP proliferation on the transwell membranes. None of the barrier models exhibited potential of recovering barrier strength after Day 11. TEER values of blank transwell membranes were relatively consistent over the period of the study. The TEER values of the barrier models were backed by the results of the FITC dye permeability assay **(Figure 4.14)**. The dye permeability assay was performed on the 7th day of TEER measurement (Day 7) to offer time for barrier formation and repeated 7 days later (Day 14). The barrier composed of hBEC lucGFP and high NHA dsRed exhibited the lowest FITC permeability on both days, which supported the previously reported TEER values. The barrier exhibited a permeability of about 4 µg/mL on Day 7, which was 24 hrs prior to its highest exhibited TEER value. The barrier composed of hBEC lucGFP and low NHA dsRed exhibited the 2nd lowest FITC permeability on both days, while barriers composed of high NHA dsRed only and low NHA dsRed only exhibited high FITC permeability on both days. It's important to note that the barrier composed of hBEC lucGFP only was the only barrier model out of the 5 models which exhibited a higher FITC permeability on Day 7 than Day 14, owing to its slightly higher barrier strength on Day 14. Blank transwell membranes exhibited negligible differences in their FITC permeability values on both Day 7 and Day 14.

4.5.1 hBEC lucGFP and NHA dsRed form confluent monolayers on apical and basal regions of the transwell membrane

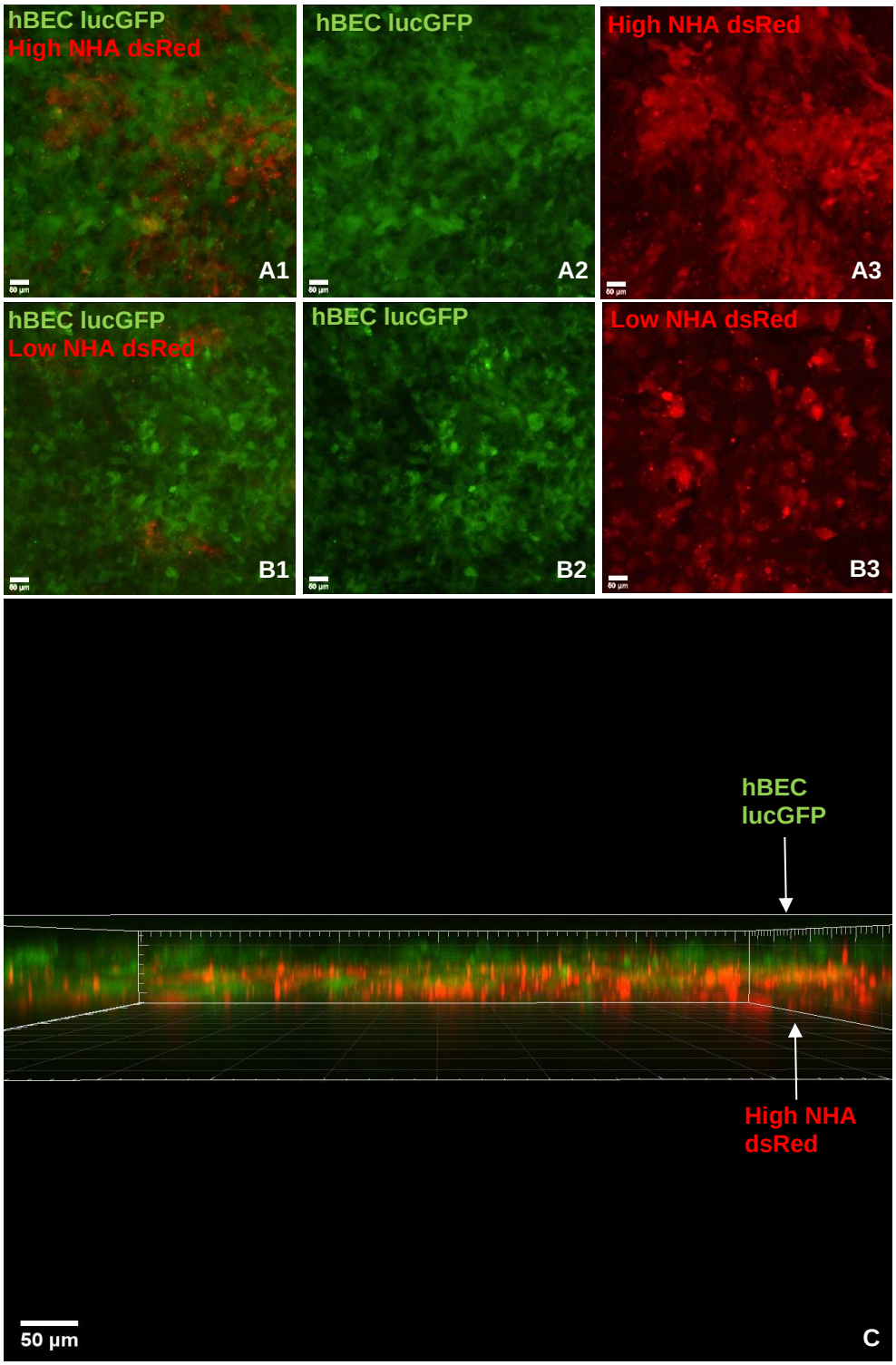

Figure 4.15 Confocal visualization of barrier models hBEC lucGFP + High NHA dsRed (A1, A2, A3) and hBEC lucGFP + Low NHA dsRed (B1, B2, B3). Images captured on 20x objective in the X-Y plane. Confocal visualization of hBEC lucGFP + high NHA dsRed in the X-Z plane (C).

Scale bar: 50 µm

Confocal visualization of hBEC lucGFP and NHA dsRed (both high and low) barriers (**Figure 4.15**) revealed the formation of confluent layer of hBEC lucGFP on the apical region of the transwell membrane and the formation of confluent layer of NHA dsRed (both high and low) on the basal region of the transwell. hBEC lucGFP exhibited geometrical direction of propagation, characteristic of endothelial monolayer formation. NHA dsRed presented as a dense cell population with overlapping cell growth. The positions of both cell layers were visibly distinguishable on confocal X-Z images and validated the ability of hBEC lucGFP and NHA dsRed to form strong barriers in cooperation with each other.

4.6 Transmigration of H1_DL2 across BBB Model can be Evaluated at a Range of Cell Seeding Densities

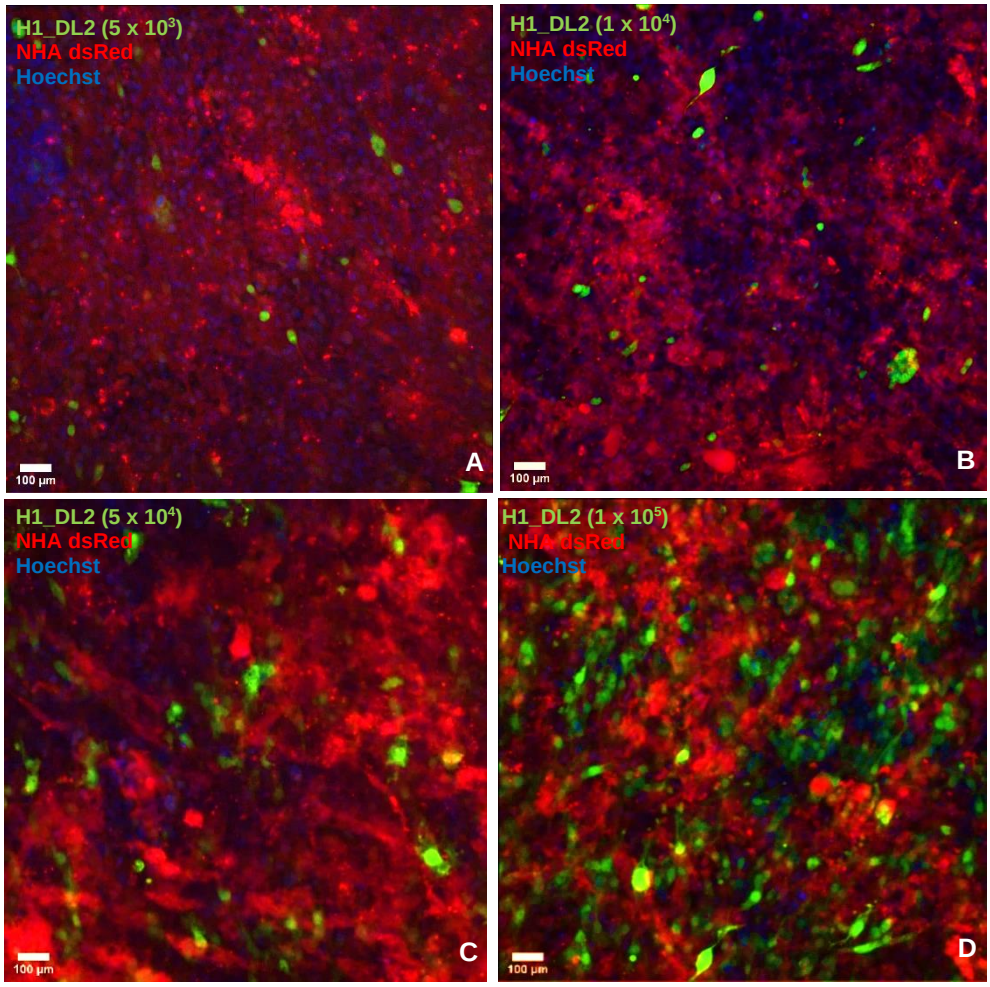

Figure 4.16 Confocal visualization of transmigrated H1_DL2 seeding densities across the BBB

model. *A indicates transmigrated H1_DL2 cells of an initial seeding density of 5 x 10^3. B indicates transmigrated H1_DL2 cells of an initial seeding density of 1 x 10^4. C indicates transmigrated H1_DL2 cells of an initial seeding density of 5 x 10^4. D indicates transmigrated H1_DL2 cells of an initial seeding density of 1 x 10^5.* Images captured on 10x objective. Scale bar: 100 µm

Analyses of the images revealed visual evidence of an increasing number of migrated H1_DL2 cells across the BBB model with increasing seeding densities. At the lowest seeded density of H1_DL2 (5 x 10^3), transmigrated H1_DL2 cells appeared as small green specks against the NHA dsRed cells present on the basal region of the BBB model barrier. At higher cell densities (1 x 10^4 and 5 x 10^4), H1_DL2 cells appeared as larger clumps of green, possibly indicating transmigration of groups of MBM cells using the same route across the BBB model. At the highest seeded density (1 x 10^5 H1_DL2 cells), transmigrated H1_DL2 cells had spread across the basal region of the barrier and were difficult to evaluate quantitatively. Unfortunately, due to coronavirus-related time constraints, the number of transmigrated H1_DL2 cells across the BBB model could not be quantified and evaluated across the selected H1_DL2 seeded densities. However, it was still evident that the BBB model could be used to evaluate the transmigratory capacity of H1_DL2 cells across the BBB at a seeding density range of 5 x 10^3 – 5 x 10^4 cells.

5. Discussion

Brain metastases remain to be a frequently daunting unmet medical challenge in patients with metastatic melanoma. Regardless of breakthroughs in neuroimaging, neurosurgery, radiotherapy, targeted therapies and immunotherapies, which have revolutionized BM management over the last decade [284], survival rates of diagnosed patients continue to be measured in months [285,286]. Advances in MBM research are hindered for several reasons, including the difficulty of modeling metastatic cancer growth in the dynamic brain microenvironment and the complex nature of the disease [287]. Current treatment strategies struggle to overcome effective drug penetration across the BBB [288], protection of secondary tumors within the brain metastatic niche [154,289] and development of tumor resistance a few months post treatment [290,291]. With that in mind, there has also been a need to diverge research into investigating the distinctive characteristics of the brain in a more "systems biology" approach, to elucidate the interactions between the components of the central nervous system and how they give rise to the function and behavior of in vivo metastatic BM pathogenesis.

In this thesis, we adopt that approach to reveal, for the first time, the presence of TNT interactions between MBM and NHA, as well as the dynamic nature of these interactions in the presence of anticancer drug treatment. We reveal our findings through the establishment of an *in vitro* 3D TNT interaction model that can be used ideally from 8 to 32 hrs to study TNT interactions between MBM and NHA. Furthermore, we also established an *in vitro* 3D BBB model with high resistance and low permeability, which can be employed ideally for a period of 72 hrs for evaluating BBB migration of MBM at a seeding density range of $5 \times 10^3 – 5 \times 10^4$ cells.

5.1 H1, HA and hBEC lucGFP exhibit Distinct Morphology and Strong Fluorescent Protein Expression *in vitro*

The triangular and elongated fusiform shape of H1_DL2 **(Figure 4.1 A1, A2, A3)** resonated similarities with that obtained of melanocytes *in vivo* [292] as well as previous morphological studies conducted in our laboratory using the established brain metastasis cell line H1.

The dense multipolar epithelial morphology with low stratification of NHA dsRed **(Figure 4.1 B1, B2, B3)** indicated similarities to contemporary characterizations of visualized astrocytes *in vivo* covering distinct regions of the CNS [293]. However, it is important to note that astrocyte

morphology is highly dynamic *in vivo*, and differ in morphology and functional diversity based on their localization within the brain [294,295]. Morphological analysis of *in vitro* NHA dsRed coincided with that described by Lange and colleagues of primary astrocyte *in vitro* cultures which form a contact inhibited monolayer with epitheloid like cells lacking synaptic contact and vascular elements. Furthermore, they suggested the coculturing of astrocytes as a means of addressing the absence of a dynamic microenvironment *in vitro* while still maintaining the advantages of monotypic astrocyte cultures [296].

hBEC lucGFP cells showed spindle-shaped, elongated morphology characteristic of brain endothelial cells and non-overlapping cell growth upon formation of confluent monolayers. The qualitative results **(Figure 4.1 C1, C2, C3)** supported past studies which used the originating cell line (hCMEC/D3) to produce cell-based assays mimicking the human BBB *in vitro* [266,297,298]. Further, the results are in line with descriptions provided by Weksler and colleagues, who also stated that the primary advantage of using this cell line was its representation of an easily grown, transferable and stable population of human microvascular cerebral endothelial cells capable of maintaining BBB phenotypes such as expression of junctional proteins, transendothelial electric resistance and restricted paracellular permeability to substances [299].

The qualitative data obtained of all 3 cell lines individually indicated successful cell sorting of high fluorescent protein expression. It is important to mention that all cell lines were received for use in the thesis after transduction and cell sorting procedures had been completed, and future studies should consider that the transduction and cell sorting procedures could provide useful information of the characteristics of the individual cell lines.

5.2 Cell Seeding Densities of 5 x 10^3 (1:1) of H1_DL2 and NHA dsRed cells yields Well-spaced, Uniform growth distribution of Cells, optimal for 8-36 hrs of Confocal Visualization of TNTs

IncuCyte evaluation results **(Figure 4.2)** revealed that a cell seeding density of 5 x 10^3 H1_DL2 and 5 x 10^3 NHA dsRed cells (1:1 ratio) provided a suitable degree of cell confluency within the field of view, uniform distribution of cells within the coculture monolayer plane and optimal frequency of visible cellular interactions. With a focus on a TNT interaction model development,

the results indicated an optimal timepoint at 8-36 hrs for attempting to visualize TNT interactions between H1_DL2 and NHA dsRed cells if they were present. While there has been a number of coculture studies for visualization of TNT interactions between 2 different cell populations [300–312], very little has been published to explain for selection of cell seeding densities in studies. Civita and colleagues justified the use of various coculture ratios of glioblastoma to astrocyte cells in their study to evaluate if both cell populations could grow together at 95% viability to establish direct contact [304]. In contrast, our analysis supports the protocol established by Abounit and colleagues, who identified optimal confluency of cells as a key parameter to achieve good conditions for TNT formation and stated that high or low confluence of cells could impair TNT formations [278]. The results also suggested an increasing frequency of visible cytoplasmic interactions between both cell populations within the established timepoint range (8-36 hrs), after which, cell populations grew too close to each other to visibly identify interactions. This was important for development of the TNT interaction model due to the 2 models of TNT interaction described in **Section 1.10**. Sowinski and colleagues identified the formation of TNT interactions between T cells after at least 4 mins of direct contact [272], while Staufer and colleagues identified passive TNT formation during protease mediated dense cell singularization [313]. Both studies suggested the possibility of passive TNT generation during cell dislodgement, which reinforced the importance for optimal frequency of visible cellular interactions in the TNT model.

5.3 H1_DL2 and NHA dsRed initiate Homotypic and Heterotypic TNT Interactions in Coculture

As observed in **Figure 4.3**, TNTs emerging from NHA dsRed cells could clearly be seen travelling over the underlying H1_DL2 cells in the substratum to form 3 heterotypic interactions with surrounding H1_DL2 cell types. This unique feature of TNTs was first identified by Rustom and colleagues in the rat pheochromocytoma (PC12) cell line [203], which distinguishes them from other discovered cellular protrusions such as cytonemes [314], streamers [315] and nanopodia [316]. Width measurements indicated confirmation of the identity of TNTs visualized, with all widths measured less than 1 μm. These results highlighted a key criterion distinguishing TNTs from intercellular bridges (widths > 1 μm) observed in cell cultures. Homotypic and heterotypic TNT interactions visualized demonstrated membrane continuity between connected cells. However, the identification of these TNT interactions as being open ended or close ended could not be

determined via confocal visualization, prompting the need for more sophisticated imaging techniques and TNT specific markers to improve TNT morphology visualization. Okafo and colleagues utilized scanning electron microscopy (SEM) techniques to obtain higher detection and resolution images of TNT mediated long range gap junctional communication in HIV infection [317], while Sartori-Rupp and colleagues utilized correlative light- and cryo-electron microscopy approaches to distinguish the cytoskeletal structural identity of TNTs from filopodia [318]. As observed in **Figure 4.4**, formation of TNT "clusters" was also detected in coculture visualization during the 24th hr of the study but were not included in the quantification since they were not seen to connect two or more cells. Interestingly, these TNT "clusters" were not detected among complete TNT interactions, and existing literature review does not provide much evidence of this phenomenon. It could be hypothesized that these clusters extend out of TNT initiating cells and disintegrate when a single TNT meets a target cell. Furthermore, the recent identification of "iTNTs", or TNTs composed of several individual tunneling nanotubes, by Korenkova and colleagues [319] could suggest an explanation for formation of these clusters. Nevertheless, the use of more sophisticated imaging techniques as well as time lapse imaging is warranted to provide more accurate identification and function of these structures. Schiller and colleagues also utilized fixation techniques to preserve the formation of TNTs by the transmembrane MHC class III protein leukocyte specific transcript 1 (LST1) [320]. The use of fixation techniques is highly debated in existing literature [217,278], owing to the fragility of TNT formations especially for *in vivo* tissue fixation. This promotes the need for improved *in vitro* model developments and suggested the introduction of gentle fixation techniques in future studies. Morphological alterations in H1_DL2 were detected in the 33rd hour of the TNT interaction study **(Figure 4.5)**. While this result may indicate the start of possible cell senescence, an alternate outcome was also suggested by Connor and colleagues, who showed that cancer cell-endothelial intercellular transport alters the phenotype of the recipient cells [321]. However, this could not be further investigated within the timeframe of the study.

The formation of homotypic TNT interactions was visualized in H1_DL2 in the 8th, 24th and 33rd hrs of the experiment. This indicated an initiation of intercellular conversation and the possible transfer of cellular cargo within the tumor cell population of the study. While further experiments are required to identify the "messages" being delivered among tumor cells, previous studies have demonstrated a correlation between tumor cell ability to form homotypic TNT interactions and a promotion of their aggressive cancer phenotype [322]. Thayanithy and colleagues identified the

transfer of oncogenic miRNAs via TNTs between malignant ovarian tumor cells and their less metastatic counterparts [323]. Furthermore, Osswald and colleagues also demonstrated a correlation between extended TNT interconnectivity among metastatic glioma cells and their poorer therapeutic response to radiotherapy [324]. Ady and colleagues demonstrated a correlation between TNT interaction within malignant mesothelioma cells and a promotion in the expression of genes related to the disease invasion and metastasis [325]. The formation of homotypic TNT interactions among varying histological grades of bladder cancer cells has also been demonstrated by Lu and colleagues to induce TNT mediated transfer of miRNA from most aggressive to least aggressive cells and promote cancer proliferation and motility [326]. Building on existing evidence, it could be hypothesized that homotypic TNT interactions between H1_DL2 cells could be a means of promoting MBM metastasis, treatment resistance, proliferation, and invasion.

The formation of heterotypic TNT interactions was also visualized between H1_DL2 and NHA dsRed 8th, 24th and 33rd hrs of the experiment. This indicated a simultaneous and possibly synchronous cellular communication between tumor cells and astrocytes within the coculture. While further experiments are required to elucidate the true nature of these conversations and the cellular cargoes transported between the two cell populations, previous studies have demonstrated the ability of TNT interactions between tumor and TME cells to induce the metastatic and invasive phenotype of the cancer. Hanna and colleagues demonstrated similar activity in *in vitro* cocultures of breast cancer cells and macrophages, where TNT mediated contacts from TME cells promoted the acquisition of invasive phenotypes in breast cancer in dependence of epidermal growth factor-epidermal growth factor receptor (EGF-EGFR) pathway [327]. Studies carried out by Pasquier and colleagues have also identified the transfer of mitochondria between TME endothelial and breast cancer cells via TNTs to possibly restore tumorigenic potential in cancer cells lacking mitochondrial DNA [328]. Finally, similar studies carried out by Errede and colleagues identified the formation of TNTs evoked by endothelial cells and pericytes in the TME to promote vascularization and angiogenic potential in human glioblastoma cells [302]. Therefore, based on existing evidence, it could be hypothesized that heterotypic TNT interactions between H1_DL2 and NHA dsRed cells could be a means of promoting MBM proliferation, invasiveness, metastasis and angiogenic ability.

5.3.1 NHA dsRed initiates higher relative percentage of homotypic and heterotypic TNT interactions in untreated H1_DL2 and NHA dsRed cocultures

Quantification results revealed a higher percentage of homotypic and heterotypic TNT interactions initiating from NHA dsRed cells across all 3 timepoints of the study, compared to H1_DL2 **(Figure 4.6)**. The results indicated that majority of MBM tumorigenicity was directed by TNT interactions initiating from NHA dsRed during the established timepoints of the study. Similar results were identified by Zhang and Zhang, who quantified a higher percentage of TNT initiations from rat primary astrocytes compared to glioma cells in coculture studies [329]. As discussed previously, TNT interactions between tumor cells and components of the TME can induce metastatic and invasive phenotypes of cancer through the transport of mitochondria, miRNAs, and other substances via TNT interactions. Wang and colleagues reported the induction of TNTs in astrocytes which were dependent on p53, EGFR, Akt, PI3K and mTOR activations, and stated the possibility of TNT formations being a characteristic feature of cells dealing with cellular stress and reducing self-metastatic development [330]. It is also interesting to mention that studies have revealed a synergistic cooperation between TNTs and exosomes. Thayanithy and colleagues demonstrated the induced enhancement of TNT formation in human mesothelioma cells by exogenous tumor exosomes [331]. Therefore, it could also be hypothesized that homotypic and heterotypic TNT interactions between H1_DL2 and NHA dsRed could also be dictated and guided by potent chemotactic exosome stimuli released by MBM to promote pathway dysregulations. Homotypic interactions between NHA dsRed cells could indicate a possible transfer of healthy mitochondria and mRNA to damaged or dying NHA dsRed cells, to maintain TME stability. Furthermore, cancer cells are recognized to influence cells in the TME to promote pathways that support their growth and development [217]. Polak and colleagues reported a signal from leukemia cells in acute lymphoblastoma to bone marrow cells resulting in the release of tumor survival promoting cytokines [332]. This could also indicate a deeper degree of MBM manipulation of the TME, through the promotion of intercellular mitochondria and miRNA distribution among NHA dsRed cells in the TME to sustain tumor proliferation, angiogenesis, and growth. The experiments provide a new insight into the relationship between MBM and the TME, and the relation of the outcome in sustaining MBM development and maintenance. However, whether TNT mediated interplay between MBM and NHA dsRed results in a net decrease or increase of tumor metastatic potential is a possibility that requires further investigation. The associated fragility of TNT interactions, which limits their lifetimes to minutes [195,201], should be taken into account in future quantification studies. While our quantification experiment was conducted twice, a further trial followed by statistical analyses (such as a t-test) is also necessary. Furthermore, the

generalizability of our results is limited by the efficiency of manually counting TNTs within the selected fields of view. The utilization of software for automated counting of TNTs, such as that developed by Hodneland and colleagues for the identification of TNT formations in PC12 cells [333], could improve the accuracy of quantification results in future studies.

5.4 H1_DL2 initiates Higher Frequency of Homotypic and Heterotypic TNT Interactions at Increasing Vemurafenib Concentrations

Confocal visualization revealed a higher frequency of homotypic and heterotypic TNT interactions initiating from H1_DL2 at increasing vemurafenib concentrations across all 3 timepoints of the study. This frequency was most pronounced across 0.8 – 1.5 μM vemurafenib drug exposure (**Figures 4.8, 4.9, 4.10**). The results indicated that TNT interactions initiated by MBM cells were more prevalent upon exposure to anticancer drug treatment in the TME microenvironment and demonstrated a correlation between increasing TNT formation in MBM and rising vemurafenib concentrations. Recently, Zoetemelk and colleagues also reported similar results, by describing an enhancement of TNT formation in colorectal cancer cells with increasing vemurafenib concentration. They concluded that this rise in TNT formations was associated with increasing therapy resistance [334]. Interestingly, 40 – 60% of metastatic colorectal cancer cases are associated with BRAF mutations [335]. Our results coincide with several studies reporting the formation of more TNTs by tumor cells in an adaptive response to therapeutic stress [217,336]. Filippova and Nabors recently reported the formation of homotypic and heterotypic TNT formations by glioma cells to promote tumor heterogeneity and survival against treatment resistance[337]. Civita and colleagues reported TNT formation between astrocytes and glioblastoma cells to be crucial in mediating tumor chemo resistance, and provided a means of transfer of cellular contents between cells under stress [304]. Based on existing evidence, it can be speculated that MBM cells could utilize TNT formations to transfer undamaged mitochondria, useful substances, or energy between cell populations in the TME to promote tumorigenesis and survival. Furthermore, Wang and Gerdes reported the use of TNT based intercellular communication by PC12 cells to prevent tumor apoptosis through the delivery of mitochondria and the dispersal of cytotoxic factors [203]. Altered morphology of H1_DL2 cells was also visualized at increasing vemurafenib concentrations **(Figures 4.7, 4.8, 4.9, 4.10)**. This analysis supports the theory that anticancer drugs induce morphological changes in target tumor cells [338–341]. Dratkiewicz and colleagues identified similar

results in vemurafenib resistant melanoma cell lines, with resistant cells being more spread out, displaying a spindle-like appearance, and presenting highly pronounced stress fibers compared to parental cell lines. Furthermore, they suggested cell spreading characteristics to be associated with alterations in focal adhesion protein levels in treated melanoma cells [342]. A recent study by Tabolacci and colleagues confirmed that BRAF inhibitor resistant cells presented a more aggressive phenotype opposed to parental cell lines, with higher production of interleukin-8, vascular-endothelial growth factor (VEGF), interferon-γ, CD147/basigin, and metalloproteinase 2 (MMP-2) [343]. Based on existing evidence, it can be speculated that MBM cell lines develop altered morphology in response to vemurafenib treatment in the process of cellular cytoskeletal reprogramming which favors their proliferation, survival, and invasiveness. Confocal visualization of the TNT model upon exposure to 0.8-1.5 µM vemurafenib **(Figures 4.8, 4.9, 4.10)** showed reduced cell density of H1_DL2 cells and large amounts of floating cell debris and non-adherent cells. These results suggest a reduction in H1_DL2 proliferation capacity as well as exhibition of cell senescence in response to increasing vemurafenib concentrations. In line with existing research, previous studies have revealed BRAF mutated cell lines to express dependent and heterogenous phenotypes in response to BRAF inhibitors such as vemurafenib, dabrafenib and trametinib nearing the IC50 concentrations of these cell lines [344–346]. Fallahi-Sichani and colleagues reported initial cell growth arrest consistent with MAPK proliferation activity and a rise in apoptosis in 40-60% of BRAF mutated melanoma cells responding to BRAF inhibitor treatment. Furthermore, they identified a subpopulation of treated cells to overcome drug mediated cell cycle arrest and exhibit decelerated cell division opposed to drug "naïve" cells [345]. Frick and colleagues and Hata and colleagues further reported a reduction in maximal drug effect on MBM cells exhibiting such drug adapted slow cycling characteristics, and suggested this behavior to contribute to development of genetically distinct drug resistant clones [347,348]. Based on this existing research evidence and our obtained results, it can be hypothesized that BRAF inhibitor resistant MBM cell lines coordinate their adaptive responses with TNT coordination between TME cells such as astrocytes to promote treatment resistance and cell survival.

5.4.1 H1_DL2 initiates increasing relative percentage of homotypic and heterotypic TNT interactions at increasing drug concentrations across all 3 timepoints of the study.

Quantification results revealed a higher percentage of homotypic and heterotypic TNT interactions initiating from H1_DL2 at increasing drug concentrations across all 3 timepoints of the study

(Figure 4.12). In line with the results discussed in **Section 5.4**, this indicated further evidence that TNT interactions initiated by MBM cells increased upon exposure to anticancer drug treatment in the TME microenvironment and demonstrated a correlation between increasing TNT formation in MBM and rising vemurafenib concentrations. Similar quantification results were obtained in a recent study by Valdebenito and colleagues, who evaluated the number of TNTs induced in glioblastoma cells in response to chemotherapeutic drug temozolomide. They found a sharp percentage increase in the number of TNTs induced in treated glioblastoma in a time dependent manner, resonating with our results in MBM cell line. The shift in prevailing relative percentage of homotypic and heterotypic TNT interactions from NHA dsRed to H1_DL2 was most pronounced in the 0.8 – 1.5 µM vemurafenib concentration range, indicating a shift in H1_DL2 behavior in coordination with NHA dsRed nearing vemurafenib concentrations presenting IC50 values in H1 monoviability studies previously conducted in our lab (with reported IC50 of 0.87 µM). In line with existing research evidence, these results support our previously mentioned hypothesis of an adaptive response promoted by BRAF inhibitor resistant MBM cell lines to maintain their tumorigenic potential and drug resistance development during anticancer treatment strategies. Furthermore, they promote studies repurposing existing drugs towards TNT inhibition and investigating TNT inhibitors as a novel class of cancer therapeutics [349]. While our quantification experiment was conducted twice, a further trial followed by statistical analyses (such as a t-test) is also necessary.

5.5 hBEC lucGFP and High Seeding Density of NHA dsRed forms Acceptable BBB Model for a period of 48 hrs

Our seeded barrier composed of hBEC lucGFP and high NHA dsRed exhibited the highest TEER values (about 50 Ohms.cm^2) over the period of 14 days **(Figures 4.13A, 4.13B)**. The TEER of the barrier remained relatively consistent from Day 8 to Day 10 of the study, which indicated its optimal use as an acceptable BBB model for 48 hrs. Our functional data results also indicated that majority of the resistance provided by the hBEC lucGFP and high NHA dsRed barrier were due to hBEC lucGFP proliferation on the transwell membranes and supported existing research evidence of astrocyte layers possessing low electrical resistance [350]. In contrast, Aasen and colleagues utilized similar techniques with 75000 hCMEC/D3 cells and 2500 human brain astrocyte cells (SC-1800) to prepare in vitro BBB model with a maximum TEER resistance of

around 28 Ohms.cm^2 [266]. The range of TEER values exhibited by model barriers utilizing different seeding densities of NHA dsRed suggested that our BBB model could be easily regulated, and barriers of higher resistance could be produced using higher seeding densities of hBEC lucGFP and NHA dsRed than those used in our study. This modifiable parameter indicated the usability of our BBB model to generate barriers possessing resistances close to that expected of the in vivo BBB (about 2000 Ohms.cm^2) [351]. However, it is important to note that the sophisticated physiological conditions of the *in vivo* BBB possesses several properties (such as circulatory flow and shear stress) that are complex to precisely reproduce *in vitro* [352,353]. The utilization of astrocytes to promote TEER in both contact and non-contact *in vitro* coculture barrier models with endothelial cell cultures has been demonstrated in numerous studies, involving murine, porcine and human cells [354–358]. Studies conducted by Abbott reported the capability of astrocytes to release humoral agents such as glutamate, adenosine triphosphate (ATP), taurine, tumor necrosis factor alpha (TNFα) and interleukin 1β IL-1β to modulate the junctional regulation of the BBB and function in barrier induction and maintenance over short time periods [180]. In contrast, the introduction of triple culture systems utilizing human and rat endothelial cells, astrocytes and pericytes have demonstrated higher TEER values than corresponding endothelial cell/astrocyte BBB models [354,359,360], and suggest a promising avenue of improvement in our currently established BBB model.

Our established BBB model composed of hBEC lucGFP and high NHA dsRed also exhibited the lowest FITC permeability on both days of dye permeability evaluation **(Figure 4.14)**, which provided further functional evidence of model barrier tightness and integrity. The use of FITC extravasation in determining the permeability of in vitro BBB models is supported in various published protocols [361,362]. Both TEER and FITC evaluation suggest the use of our established model as a standard system for estimating MBM proliferation and pathogenesis across BBB, as well as transport parameters of drug delivery into CNS. Furthermore, the use of peptides, such as K16ApoE, which promote BBB permeability and consequently, improved drug delivery in targeted MBM treatment could be further investigated [266] using this model.

5.5.1 hBEC lucGFP and NHA dsRed form confluent monolayers on apical and basal regions of the transwell membrane

Confocal visualization of hBEC lucGFP and NHA dsRed (both high and low) barriers **(Figure 4.15)** in both X-Y and X-Z planes validated the ability of hBEC lucGFP and NHA dsRed to form

strong barriers in cooperation with each other. Our localization analysis indicated the capability of both cell populations to form coordinated confluent spread on both apical and basal regions of the transwell membrane. Czupalla and colleagues suggested the integration of expression analysis techniques (via qRT-PCR and Western blotting) to promote confidence in functional data and to monitor gene expression of barrier related proteins such as ZO-1 and occludin [363]. Furthermore, the use of immunocytochemistry techniques to implement immunofluorescence staining of junctional proteins cadherin, ZO-1, claudin and actin could provide a higher degree of localization information for BBB phenotype in future studies [185,364,365].

5.6 Transmigration of H1_DL2 can be Evaluated at a Range of Cell Seeding Densities across Established in vitro BBB Model

Confocal analyses revealed localization evidence of an increasing number of transmigrated H1_DL2 cells across our *in vitro* BBB model with increasing seeding densities **(Figure 4.16)**. Our results also revealed H1_DL2 clumping upon barrier transmigration at higher seeded densities (1 x 10^4 and 5 x 10^4 cells) and indicated collective utilization of transmigratory routes across the BBB by MBM. Similar results were obtained by Fazakas and colleagues, who suggested that transmigrated melanoma cells attracted other melanoma cells to migrate across endothelial cell layers at the same site. They further reported the ability of melanoma cells to initiate disruption of inter-endothelial junctions and migrate via paracellular pathways across the BBB [185]. Dratkiewicz and colleagues also reported a more aggressive migratory and invasive phenotype in vemurafenib resistant cell lines compared to their parental counterparts [342]. While our initial plan was to quantify the number of transmigrated H1_DL2 cells across the BBB model to evaluate this characteristic, due to coronavirus-related time constraints, we were unable to do so. Furthermore, confocal images of transmigrated H1_DL2 at 1x10^5 seeded densities revealed formation of continuous layer of H1_DL2 cells across basolateral region of barrier that was difficult to quantify, indicating the optimal use of our established BBB model for evaluating transmigration of low seeded densities of H1_DL2. The integration of expression analysis techniques in future studies could provide further information of the factors and molecules involved in the transmigration process [366,367], as well as utilization of more sophisticated microscopy techniques to evaluate contact between endothelial cells and astrocytes in the BBB model [368].

5.7 Future Perspectives

The use of targeted therapies has provided transformative evidence in the treatment of MBM as well as improved patient survival outcomes. However, the lack of therapies equally effective against extracranial and cranial diseases has called for refined therapeutic strategies that account for both the biology of the brain microenvironment and the melanoma metastatic cascade. The urge for reduced needs of experimental animals and lower costs have called for the development of *in vitro* models for use prior or parallel with *in vivo* models. The emergence of 3D *in vitro* models which incorporate patient derived tissues/cells and allow longitudinal measurements to mimic the TME, have bridged the divide between oversimplified 2D systems and unrepresentative animal models. Our established 3D *in vitro* TNT interaction and BBB models have provided novel information and deeper understanding of MBM interactions with the TME. The next logical step would be refining these models to better represent the complexities of the *in vivo* environment and to integrate techniques (as previously discussed) into these models to better identify spatial and temporal tumor interactions with system cells, as well as identify molecular players responsible for orchestrating these interactions. Identifying the processes by which MBM cells communicate with components of the BME to avoid therapeutic elimination will expose new vulnerabilities and pave the way for more effective treatment strategies. Till date, the identification of TNTs is based on their morphological characteristics, and the morphological diversity of these structures has instituted ambiguity to the nomenclature and literature review of these structures. The unification of established terminology for TNTs is of dire need, and the maturation of methods for studying homotypic and heterotypic TNT interactions initiated by MBM and their role in the pathogenesis of the disease could significantly lead the next generation of novel MBM prognostic markers and provide novel targets for cancer therapy. The identification of TNT specific biomarkers could aid in understanding the cargo being distributed between MBM and the BME, as well as provide vital information on cell signaling pathway dysregulation mechanisms. Furthermore, the development of small molecule inhibitors which target specific upregulated proteins involved in MBM invasion and migration across the BBB could turn the tide against the aggressive phenotype developed by MBM, especially those which are BRAF inhibitor resistant. We eagerly anticipate the extent to which these 3D *in vitro* models develop soon, and their incorporation as mainstream cancer evaluation systems in the biomedical and pharmaceutical industries.

References

(1) Carr, S.; Smith, C.; Wernberg, J. Epidemiology and Risk F a c t o r s o f Me l a n o m a Melanoma Carcinogen Ultraviolet Radiation Indoor Tanning Prevention. *Surg. Clin. NA* **2020**, *100* (1), 1–12. https://doi.org/10.1016/j.suc.2019.09.005.

(2) Duncan, L. M. D. The Classification of Cutaneous Melanoma. *Hematology/Oncology Clinics of North America*. Elsevier June 1, 2009, pp 501–513. https://doi.org/10.1016/j.hoc.2009.03.013.

(3) Sivamani, R. K.; Crane, L. A.; Dellavalle, R. P. The Benefits and Risks of Ultraviolet Tanning and Its Alternatives: The Role of Prudent Sun Exposure. *Dermatologic Clinics*. April 2009, pp 149–154. https://doi.org/10.1016/j.det.2008.11.008.

(4) [Figure, Schematic representation of normal skin...] - PDQ Cancer Information Summaries - NCBI Bookshelf https://www.ncbi.nlm.nih.gov/books/NBK66034/figure/CDR0000062917__343/ (accessed Mar 14, 2021).

(5) Rigel, D. S.; Carucci, J. A. Malignant Melanoma: Prevention, Early Detection, and Treatment in the 21st Century. *CA. Cancer J. Clin.* **2000**, *50* (4), 215–236. https://doi.org/10.3322/canjclin.50.4.215.

(6) Desmond, R. A.; Soong, S. jaw. Epidemiology of Malignant Melanoma. *Surgical Clinics of North America*. February 2003, pp 1–29. https://doi.org/10.1016/S0039-6109(02)00092-0.

(7) Erdei, E.; Torres, S. M. A New Understanding in the Epidemiology of Melanoma. *Expert Review of Anticancer Therapy*. November 2010, pp 1811–1823. https://doi.org/10.1586/era.10.170.

(8) 2020 MELANOMA SKIN CANCER REPORT | Melanoma UK https://www.melanomauk.org.uk/2020-melanoma-skin-cancer-report (accessed Jan 28, 2021).

(9) Bray, F.; Ferlay, J.; Soerjomataram, I.; Siegel, R. L.; Torre, L. A.; Jemal, A. Global Cancer Statistics 2018: GLOBOCAN Estimates of Incidence and Mortality Worldwide for 36 Cancers in 185 Countries. *CA. Cancer J. Clin.* **2018**, *68* (6), 394–424. https://doi.org/10.3322/caac.21492.

(10) Cancer Registry of Norway. Cancer in Norway 2019 - Cancer Incidence, Mortality, Survival and Prevalence in Norway. *Cancer Regist. Norw.* **2020**.

(11) Sloan, A. E.; Nock, C. J.; Einstein, D. B. Diagnosis and Treatment of Melanoma Brain Metastasis: A Literature Review. *Cancer Control*. H. Lee Moffitt Cancer Center and Research Institute 2009, pp 248–255. https://doi.org/10.1177/107327480901600307.

(12) Langer, C. J.; Mehta, M. P. Current Management of Brain Metastases, with a Focus on Systemic Options. *Journal of Clinical Oncology*. 2005, pp 6207–6219. https://doi.org/10.1200/JCO.2005.03.145.

(13) Zhang, D.; Wang, Z.; Shang, D.; Yu, J.; Yuan, S. Incidence and Prognosis of Brain Metastases in Cutaneous Melanoma Patients: A Population-Based Study. *Melanoma Res.* **2019**, *29* (1), 77–84. https://doi.org/10.1097/CMR.0000000000000538.

(14) Boniol, M.; Autier, P.; Boyle, P.; Gandini, S. Cutaneous Melanoma Attributable to Sunbed Use: Systematic Review and Meta-Analysis. *BMJ* **2012**, *345* (7877). https://doi.org/10.1136/bmj.e4757.

(15) Ghiasvand, R.; Rueegg, C. S.; Weiderpass, E.; Green, A. C.; Lund, E.; Veierød, M. B.

Indoor Tanning and Melanoma Risk: Long-Term Evidence From a Prospective Population-Based Cohort Study. *Am. J. Epidemiol.* **2017**, *185* (3), 147–156. https://doi.org/10.1093/aje/kww148.

(16) Le Clair, M. Z.; Cockburn, M. G. Tanning Bed Use and Melanoma: Establishing Risk and Improving Prevention Interventions. *Preventive Medicine Reports*. Elsevier Inc. June 1, 2016, pp 139–144. https://doi.org/10.1016/j.pmedr.2015.11.016.

(17) Reimann, J.; McWhirter, J. E.; Papadopoulos, A.; Dewey, C. A Systematic Review of Compliance with Indoor Tanning Legislation. *BMC Public Health*. BioMed Central Ltd. October 4, 2018, p 1096. https://doi.org/10.1186/s12889-018-5994-4.

(18) Wangari-Talbot, J.; Chen, S. Genetics of Melanoma. *Frontiers in Genetics*. Frontiers Media SA 2013. https://doi.org/10.3389/fgene.2012.00330.

(19) Potrony, M.; Badenas, C.; Aguilera, P.; Puig-Butille, J. A.; Carrera, C.; Malvehy, J.; Puig, S. Update in Genetic Susceptibility in Melanoma. *Annals of Translational Medicine*. AME Publishing Company September 1, 2015, p 210. https://doi.org/10.3978/j.issn.2305-5839.2015.08.11.

(20) Ribero, S.; Longo, C.; Glass, D.; Nathan, P.; Bataille, V. What Is New in Melanoma Genetics and Treatment? *Dermatology* **2016**, *232* (3), 259–264. https://doi.org/10.1159/000445767.

(21) Watson, M.; Holman, D. M.; Maguire-Eisen, M. Ultraviolet Radiation Exposure and Its Impact on Skin Cancer Risk. *Seminars in Oncology Nursing*. W.B. Saunders August 1, 2016, pp 241–254. https://doi.org/10.1016/j.soncn.2016.05.005.

(22) Sample, A.; He, Y. Y. Mechanisms and Prevention of UV-Induced Melanoma. *Photodermatology Photoimmunology and Photomedicine*. Blackwell Publishing Ltd January 1, 2018, pp 13–24. https://doi.org/10.1111/phpp.12329.

(23) Savoye, I.; Olsen, C. M.; Whiteman, D. C.; Bijon, A.; Wald, L.; Dartois, L.; Clavel-Chapelon, F.; Boutron-Ruault, M. C.; Kvaskoff, M. Patterns of Ultraviolet Radiation Exposure and Skin Cancer Risk: The E3N-SunExp Study. *J. Epidemiol.* **2018**, *28* (1), 27–33. https://doi.org/10.2188/jea.JE20160166.

(24) Rossi, M.; Pellegrini, C.; Cardelli, L.; Ciciarelli, V.; di Nardo, L.; Fargnoli, M. C. Familial Melanoma: Diagnostic and Management Implications. *Dermatol. Pract. Concept.* **2019**, *9* (1), 10–16. https://doi.org/10.5826/dpc.0901a03.

(25) Dębniak, T. Familial Malignant Melanoma - Overview. *Hered. Cancer Clin. Pract.* **2004**, *2* (3), 123. https://doi.org/10.1186/1897-4287-2-3-123.

(26) Systemic Medications Linked to an Increased Risk for Skin Malignancy | MDedge Dermatology https://www.mdedge.com/dermatology/article/211646/melanoma/systemic-medications-linked-increased-risk-skin-malignancy?sso=true (accessed Mar 9, 2021).

(27) Tchernev, G.; Temelkova, I. Drug-Induced Melanoma: Irbesartan Induced Cutaneous Melanoma! First Description in the World Literature! *Open Access Maced. J. Med. Sci.* **2019**, *7* (1), 114–116. https://doi.org/10.3889/oamjms.2019.042.

(28) Wich, L. G.; Ma, M. W.; Price, L. S.; Sidash, S.; Berman, R. S.; Pavlick, A. C.; Miller, G.; Sarpel, U.; Goldberg, J. D.; Osman, I. Impact of Socioeconomic Status and Sociodemographic Factors on Melanoma Presentation among Ethnic Minorities. *J. Community Health* **2011**, *36* (3), 461–468. https://doi.org/10.1007/s10900-010-9328-4.

(29) Reyes-Ortiz, C. A.; Goodwin, J. S.; Freeman, J. L.; Kuo, Y. F. Socioeconomic Status and Survival in Older Patients with Melanoma. *J. Am. Geriatr. Soc.* **2006**, *54* (11), 1758–1764.

https://doi.org/10.1111/j.1532-5415.2006.00943.x.

(30) Salvaggio, C.; Han, S. W.; Martires, K.; Robinson, E.; Madankumar, R.; Gumaste, P.; Polsky, D.; Stein, J.; Berman, R.; Shapiro, R.; et al. Impact of Socioeconomic Status and Ethnicity on Melanoma Presentation and Recurrence in Caucasian Patients. *Oncology* **2016**, *90* (2), 79–87. https://doi.org/10.1159/000441524.

(31) Falcone, L. M.; Zeidler-Erdely, P. C. Skin Cancer and Welding. *Clinical and Experimental Dermatology*. Blackwell Publishing Ltd March 1, 2019, pp 130–134. https://doi.org/10.1111/ced.13783.

(32) Heltoft, K. N.; Slagor, R. M.; Agner, T.; Bonde, J. P. Metal Arc Welding and the Risk of Skin Cancer. *Int. Arch. Occup. Environ. Health* **2017**, *90* (8), 873–881. https://doi.org/10.1007/s00420-017-1248-5.

(33) Dixon, A. J.; Dixon, B. F. Ultraviolet Radiation from Welding and Possible Risk of Skin and Ocular Malignancy. *Med. J. Aust.* **2004**, *181* (3), 155–157. https://doi.org/10.5694/j.1326-5377.2004.tb06207.x.

(34) Goldstein, A. M.; Tucker, M. A. Dysplastic Nevi and Melanoma. *Cancer Epidemiol. Biomarkers Prev.* **2013**, *22* (4), 528–532. https://doi.org/10.1158/1055-9965.EPI-12-1346.

(35) Roh, M. R.; Eliades, P.; Gupta, S.; Tsao, H. Genetics of Melanocytic Nevi. *Pigment Cell and Melanoma Research*. Blackwell Publishing Ltd November 1, 2015, pp 661–672. https://doi.org/10.1111/pcmr.12412.

(36) Damsky, W. E.; Bosenberg, M. Melanocytic Nevi and Melanoma: Unraveling a Complex Relationship. *Oncogene*. Nature Publishing Group October 19, 2017, pp 5771–5792. https://doi.org/10.1038/onc.2017.189.

(37) Sondermeijer, L.; Lamboo, L. G. E.; de Waal, A. C.; Galesloot, T. E.; Kiemeney, L. A. L. M.; van Rossum, M.; Aben, K. H. Cigarette Smoking and the Risk of Cutaneous Melanoma: A Case-Control Study. *Dermatology* **2020**, *236* (3), 228–236. https://doi.org/10.1159/000502129.

(38) Kessides, M. C.; Wheless, L.; Hoffman-Bolton, J.; Clipp, S.; Alani, R. M.; Alberg, A. J. Cigarette Smoking and Malignant Melanoma: A Case-Control Study. *J. Am. Acad. Dermatol.* **2011**, *64* (1), 84–90. https://doi.org/10.1016/j.jaad.2010.01.041.

(39) Song, F.; Qureshi, A. A.; Gao, X.; Li, T.; Han, J. Smoking and Risk of Skin Cancer: A Prospective Analysis and a Meta-Analysis. *Int. J. Epidemiol.* **2012**, *41* (6), 1694–1705. https://doi.org/10.1093/ije/dys146.

(40) Ward-Peterson, M.; Acuña, J. M.; Alkhalifah, M. K.; Nasiri, A. M.; Al-Akeel, E. S.; Alkhaldi, T. M.; Dawari, S. A.; Aldaham, S. A. Association between Race/Ethnicity and Survival of Melanoma Patients in the United States over 3 Decades. *Med. (United States)* **2016**, *95* (17). https://doi.org/10.1097/MD.0000000000003315.

(41) Gupta, A. K.; Bharadwaj, M.; Mehrotra, R. Skin Cancer Concerns in People of Color: Risk Factors and Prevention. *Asian Pacific Journal of Cancer Prevention*. Asian Pacific Organization for Cancer Prevention 2016, pp 6157–6164. https://doi.org/10.22034/APJCP.2016.17.12.6157.

(42) Wang, Y.; Zhao, Y.; Ma, S. Racial Differences in Six Major Subtypes of Melanoma: Descriptive Epidemiology. *BMC Cancer* **2016**, *16* (1), 691. https://doi.org/10.1186/s12885-016-2747-6.

(43) Amaro-Ortiz, A.; Yan, B.; D'Orazio, J. A. Ultraviolet Radiation, Aging and the Skin: Prevention of Damage by Topical CAMP Manipulation. *Molecules*. Molecular Diversity

Preservation International 2014, pp 6202–6219. https://doi.org/10.3390/molecules19056202.

(44) Tas, F.; Erturk, K. Patient Age and Cutaneous Malignant Melanoma: Elderly Patients Are Likely to Have More Aggressive Histological Features and Poorer Survival. *Mol. Clin. Oncol.* **2017**, *7* (6), 1083. https://doi.org/10.3892/mco.2017.1439.

(45) Fleming, N. H.; Tian, J.; Vega-Saenz de Miera, E.; Gold, H.; Darvishian, F.; Pavlick, A. C.; Berman, R. S.; Shapiro, R. L.; Polsky, D.; Osman, I. Impact of Age on the Management of Primary Melanoma Patients. *Oncology* **2013**, *85* (3), 173–181. https://doi.org/10.1159/000351499.

(46) Chen, J.; Shih, J.; Tran, A.; Mullane, A.; Thomas, C.; Aydin, N.; Misra, S. Gender-Based Differences and Barriers in Skin Protection Behaviors in Melanoma Survivors. *J. Skin Cancer* **2016**, *2016*. https://doi.org/10.1155/2016/3874572.

(47) Joosse, A.; De Vries, E.; Eckel, R.; Nijsten, T.; Eggermont, A. M. M.; Hölzel, D.; Coebergh, J. W. W.; Engel, J. Gender Differences in Melanoma Survival: Female Patients Have a Decreased Risk of Metastasis. *J. Invest. Dermatol.* **2011**, *131* (3), 719–726. https://doi.org/10.1038/jid.2010.354.

(48) Morgese, F.; Sampaolesi, C.; Torniai, M.; Conti, A.; Ranallo, N.; Giacchetti, A.; Serresi, S.; Onofri, A.; Burattini, M.; Ricotti, G.; et al. Gender Differences and Outcomes in Melanoma Patients. *Oncol. Ther.* **2020**, *8* (1), 103–114. https://doi.org/10.1007/s40487-020-00109-1.

(49) Erdei, E.; Torres, S. M. A New Understanding in the Epidemiology of Melanoma. *Expert Review of Anticancer Therapy*. NIH Public Access November 2010, pp 1811–1823. https://doi.org/10.1586/era.10.170.

(50) O'Shea, S. J.; Rogers, Z.; Warburton, F.; Ramirez, A. J.; Newton-Bishop, J. A.; Forbes, L. J. L. Which Symptoms Are Linked to a Delayed Presentation among Melanoma Patients? A Retrospective Study. *BMC Cancer* **2017**, *17* (1), 5. https://doi.org/10.1186/s12885-016-2978-6.

(51) Crossed Signokić, M. D.; Badovinac, D.; Petrič, M.; Trotovšek, B. An Unusual Presentation of Metastatic Malignant Melanoma Causing Jejuno-Jejunal Intussusception: A Case Report. *J. Med. Case Rep.* **2018**, *12* (1), 337. https://doi.org/10.1186/s13256-018-1887-5.

(52) Kubica, A. W.; Brewer, J. D. Melanoma in Immunosuppressed Patients. *Mayo Clinic Proceedings*. Elsevier Ltd 2012, pp 991–1003. https://doi.org/10.1016/j.mayocp.2012.04.018.

(53) Passarelli, A.; Mannavola, F.; Stucci, L. S.; Tucci, M.; Silvestris, F. Immune System and Melanoma Biology: A Balance between Immunosurveillance and Immune Escape. *Oncotarget*. Impact Journals LLC 2017, pp 106132–106142. https://doi.org/10.18632/oncotarget.22190.

(54) Austin, J.; Wright, F. C.; Cheng, S. Y.; Sutradhar, R.; Baxter, N. N.; Look Hong, N. J. Outcomes of Immunosuppressed Patients Who Develop Melanoma: A Population-Based Propensity-Matched Cohort Study. *Ann. Surg. Oncol.* **2020**, *27* (8), 2927–2948. https://doi.org/10.1245/s10434-020-08265-4.

(55) D'Orazio, J.; Jarrett, S.; Amaro-Ortiz, A.; Scott, T. UV Radiation and the Skin. *International Journal of Molecular Sciences*. MDPI AG 2013, pp 12222–12248. https://doi.org/10.3390/ijms140612222.

(56) Anna, B.; Blazej, Z.; Jacqueline, G.; Andrew, C. J.; Jeffrey, R.; Andrzej, S. Mechanism of

UV-Related Carcinogenesis and Its Contribution to Nevi/Melanoma. *Expert Rev. Dermatol.* **2007**, *2* (4), 451–469.

(57) Bandarchi, B.; Ma, L.; Navab, R.; Seth, A.; Rasty, G. From Melanocyte to Metastatic Malignant Melanoma. *Dermatology Research and Practice*. Hindawi Publishing Corporation 2010. https://doi.org/10.1155/2010/583748.

(58) Wu, S.; Cho, E.; Li, W. Q.; Weinstock, M. A.; Han, J.; Qureshi, A. A. History of Severe Sunburn and Risk of Skin Cancer among Women and Men in 2 Prospective Cohort Studies. *Am. J. Epidemiol.* **2016**, *183* (9), 824–833. https://doi.org/10.1093/aje/kwv282.

(59) Aase, A.; Bentham, G. The Geography of Malignant Melanoma in the Nordic Countries: The Implications of Stratospheric Ozone Depletion. *Geogr. Ann. Ser. B.* **1994**, *76* (2), 129. https://doi.org/10.2307/490595.

(60) Mark Elwood, J.; Jopson, J. Melanoma and Sun Exposure: An Overview of Published Studies. *Int. J. Cancer* **1997**, *73* (2), 198–203. https://doi.org/10.1002/(SICI)1097-0215(19971009)73:2<198::AID-IJC6>3.0.CO;2-R.

(61) Melanoma Treatment (PDQ®)–Patient Version - National Cancer Institute https://www.cancer.gov/types/skin/patient/melanoma-treatment-pdq (accessed Mar 9, 2021).

(62) Gandini, S.; Sera, F.; Cattaruzza, M. S.; Pasquini, P.; Abeni, D.; Boyle, P.; Melchi, C. F. Meta-Analysis of Risk Factors for Cutaneous Melanoma: I. Common and Atypical Naevi. *Eur. J. Cancer* **2005**, *41* (1), 28–44. https://doi.org/10.1016/j.ejca.2004.10.015.

(63) Hawryluk, E. B.; Tsao, H. Melanoma: Clinical Features and Genomic Insights. *Cold Spring Harb. Perspect. Med.* **2014**, *4* (9). https://doi.org/10.1101/cshperspect.a015388.

(64) Bandarchi, B.; Jabbari, C. A.; Vedadi, A.; Navab, R. Molecular Biology of Normal Melanocytes and Melanoma Cells. *Journal of Clinical Pathology*. J Clin Pathol August 2013, pp 644–648. https://doi.org/10.1136/jclinpath-2013-201471.

(65) Elder, D. E.; Bastian, B. C.; Cree, I. A.; Massi, D.; Scolyer, R. A. The 2018 World Health Organization Classification of Cutaneous, Mucosal, and Uveal Melanoma Detailed Analysis of 9 Distinct Subtypes Defined by Their Evolutionary Pathway. *Archives of Pathology and Laboratory Medicine*. College of American Pathologists April 1, 2020, pp 500–522. https://doi.org/10.5858/arpa.2019-0561-RA.

(66) Pan, Y.; Adler, N. R.; Wolfe, R.; McLean, C. A.; Kelly, J. W. Nodular Melanoma Is Less Likely than Superficial Spreading Melanoma to Be Histologically Associated with a Naevus. *Med. J. Aust.* **2017**, *207* (8), 333–338. https://doi.org/10.5694/mja17.00232.

(67) Cancer Grade Vs. Cancer Stage | MD Anderson Cancer Center https://www.mdanderson.org/patients-family/diagnosis-treatment/a-new-diagnosis/cancer-grade-vs--cancer-stage.html (accessed Mar 14, 2021).

(68) Gress, D. M.; Edge, S. B.; Greene, F. L.; Washington, M. K.; Asare, E. A.; Brierley, J. D.; Byrd, D. R.; Compton, C. C.; Jessup, J. M.; Winchester, D. P.; et al. Principles of Cancer Staging. In *AJCC Cancer Staging Manual*; Springer International Publishing, 2017; pp 3–30. https://doi.org/10.1007/978-3-319-40618-3_1.

(69) Zbytek, B.; Carlson, J. A.; Granese, J.; Ross, J.; Mihm, M.; Slominski, A. Current Concepts of Metastasis in Melanoma. *Expert Review of Dermatology*. NIH Public Access October 2008, pp 569–585. https://doi.org/10.1586/17469872.3.5.569.

(70) Curiel-Lewandrowski, C.; Chen, S. C.; Swetter, S. M. Screening and Prevention Measures for Melanoma: Is There a Survival Advantage? *Curr. Oncol. Rep.* **2012**, *14* (5), 458–467.

https://doi.org/10.1007/s11912-012-0256-6.
(71) Shaikh, W. R.; Dusza, S. W.; Weinstock, M. A.; Oliveria, S. A.; Geller, A. C.; Halpern, A. C. Melanoma Thickness and Survival Trends in the United States, 1989-2009. *Journal of the National Cancer Institute*. Oxford University Press January 1, 2016, p 294. https://doi.org/10.1093/jnci/djv294.
(72) Stages of Melanoma - AIM at Melanoma Foundation https://www.aimatmelanoma.org/stages-of-melanoma/ (accessed Mar 14, 2021).
(73) Sandru, A.; Voinea, S.; Panaitescu, E.; Blidaru, A. Survival Rates of Patients with Metastatic Malignant Melanoma. *J. Med. Life* **2014**, *7* (4), 572–576.
(74) Ward, W. H.; Lambreton, F.; Goel, N.; Yu, J. Q.; Farma, J. M. Clinical Presentation and Staging of Melanoma. In *Cutaneous Melanoma: Etiology and Therapy*; Codon Publications, 2017; pp 79–89. https://doi.org/10.15586/codon.cutaneousmelanoma.2017.ch6.
(75) Ali, S. A.; Naaz, I. Biochemical Aspects of Mammalian Melanocytes and the Emerging Role of Melanocyte Stem Cells in Dermatological Therapies. *Int. J. Health Sci. (Qassim).* **2018**, *12* (1), 69–76.
(76) Brenner, M.; Hearing, V. J. The Protective Role of Melanin against UV Damage in Human Skin. *Photochemistry and Photobiology*. NIH Public Access May 2008, pp 539–549. https://doi.org/10.1111/j.1751-1097.2007.00226.x.
(77) Solano, F. Photoprotection and Skin Pigmentation: Melanin-Related Molecules and Some Other New Agents Obtained from Natural Sources. *Molecules*. MDPI AG 2020. https://doi.org/10.3390/molecules25071537.
(78) Kim, D. S.; Park, S. H.; Kwon, S. B.; Joo, Y. H.; Youn, S. W.; Sohn, U. D.; Park, K. C. Temperature Regulates Melanin Synthesis in Melanocytes. *Arch. Pharm. Res.* **2003**, *26* (10), 840–845. https://doi.org/10.1007/BF02980030.
(79) BUSTAMANTE, J.; BREDESTON, L.; MALANGA, G.; MORDOH, J. Role of Melanin as a Scavenger of Active Oxygen Species. *Pigment Cell Res.* **1993**, *6* (5), 348–353. https://doi.org/10.1111/j.1600-0749.1993.tb00612.x.
(80) Darwiche, N. Epigenetic Mechanisms and the Hallmarks of Cancer: An Intimate Affair. *Am. J. Cancer Res.* **2020**, *10* (7), 1954–1978.
(81) Gajewski, T. F. Molecular Profiling of Melanoma and the Evolution of Patient-Specific Therapy. *Semin. Oncol.* **2011**, *38* (2), 236–242. https://doi.org/10.1053/j.seminoncol.2011.01.004.
(82) Lawrence, M. S.; Stojanov, P.; Polak, P.; Kryukov, G. V.; Cibulskis, K.; Sivachenko, A.; Carter, S. L.; Stewart, C.; Mermel, C. H.; Roberts, S. A.; et al. Mutational Heterogeneity in Cancer and the Search for New Cancer-Associated Genes. *Nature* **2013**, *499* (7457), 214–218. https://doi.org/10.1038/nature12213.
(83) Davis, E. J.; Johnson, D. B.; Sosman, J. A.; Chandra, S. Melanoma: What Do All the Mutations Mean? *Cancer*. John Wiley and Sons Inc. September 1, 2018, pp 3490–3499. https://doi.org/10.1002/cncr.31345.
(84) Miaczynska, M. Effects of Membrane Trafficking on Signaling by Receptor Tyrosine Kinases. *Cold Spring Harb. Perspect. Biol.* **2013**, *5* (11), 9035–9036. https://doi.org/10.1101/cshperspect.a009035.
(85) Paluncic, J.; Kovacevic, Z.; Jansson, P. J.; Kalinowski, D.; Merlot, A. M.; Huang, M. L. H.; Lok, H. C.; Sahni, S.; Lane, D. J. R.; Richardson, D. R. Roads to Melanoma: Key Pathways and Emerging Players in Melanoma Progression and Oncogenic Signaling. *Biochimica et*

Biophysica Acta - Molecular Cell Research. Elsevier B.V. April 1, 2016, pp 770–784. https://doi.org/10.1016/j.bbamcr.2016.01.025.

(86) Flaherty, K. T.; Puzanov, I.; Kim, K. B.; Ribas, A.; McArthur, G. A.; Sosman, J. A.; O'Dwyer, P. J.; Lee, R. J.; Grippo, J. F.; Nolop, K.; et al. Inhibition of Mutated, Activated BRAF in Metastatic Melanoma. *N. Engl. J. Med.* **2010**, *363* (9), 809–819. https://doi.org/10.1056/NEJMoa1002011.

(87) Holderfield, M.; Deuker, M. M.; McCormick, F.; McMahon, M. Targeting RAF Kinases for Cancer Therapy: BRAF-Mutated Melanoma and Beyond. *Nature Reviews Cancer*. Nature Publishing Group 2014, pp 455–467. https://doi.org/10.1038/nrc3760.

(88) Lokhandwala, P. M.; Tseng, L. H.; Rodriguez, E.; Zheng, G.; Pallavajjalla, A.; Gocke, C. D.; Eshleman, J. R.; Lin, M. T. Clinical Mutational Profiling and Categorization of BRAF Mutations in Melanomas Using next Generation Sequencing. *BMC Cancer* **2019**, *19* (1), 665. https://doi.org/10.1186/s12885-019-5864-1.

(89) McCubrey, J. A.; Steelman, L. S.; Abrams, S. L.; Lee, J. T.; Chang, F.; Bertrand, F. E.; Navolanic, P. M.; Terrian, D. M.; Franklin, R. A.; D'Assoro, A. B.; et al. Roles of the RAF/MEK/ERK and PI3K/PTEN/AKT Pathways in Malignant Transformation and Drug Resistance. *Adv. Enzyme Regul.* **2006**, *46* (1), 249–279. https://doi.org/10.1016/j.advenzreg.2006.01.004.

(90) Pollock, P. M.; Harper, U. L.; Hansen, K. S.; Yudt, L. M.; Stark, M.; Robbins, C. M.; Moses, T. Y.; Hostetter, G.; Wagner, U.; Kakareka, J.; et al. High Frequency of BRAF Mutations in Nevi. *Nat. Genet.* **2003**, *33* (1), 19–20. https://doi.org/10.1038/ng1054.

(91) Dhillon, A. S.; Hagan, S.; Rath, O.; Kolch, W. MAP Kinase Signalling Pathways in Cancer. *Oncogene*. Oncogene May 14, 2007, pp 3279–3290. https://doi.org/10.1038/sj.onc.1210421.

(92) Zuber, J.; Tchernitsa, O. I.; Hinzmann, B.; Schmitz, A. C.; Grips, M.; Hellriegel, M.; Sers, C.; Rosenthal, A.; Schäfer, R. A Genome-Wide Survey of RAS Transformation Targets. *Nat. Genet.* **2000**, *24* (2), 144–152. https://doi.org/10.1038/72799.

(93) Davies, H.; Bignell, G. R.; Cox, C.; Stephens, P.; Edkins, S.; Clegg, S.; Teague, J.; Woffendin, H.; Garnett, M. J.; Bottomley, W.; et al. Mutations of the BRAF Gene in Human Cancer. *Nature* **2002**, *417* (6892), 949–954. https://doi.org/10.1038/nature00766.

(94) Kelleher, F. C.; McArthur, G. A. Targeting NRAS in Melanoma. *Cancer Journal*. Cancer J March 2012, pp 132–136. https://doi.org/10.1097/PPO.0b013e31824ba4df.

(95) Burd, C. E.; Liu, W.; Huynh, M. V.; Waqas, M. A.; Gillahan, J. E.; Clark, K. S.; Fu, K.; Martin, B. L.; Jeck, W. R.; Souroullas, G. P.; et al. Mutation-Specific RAS Oncogenicity Explains NRAS Codon 61 Selection in Melanoma. *Cancer Discov.* **2014**, *4* (12), 1418–1429. https://doi.org/10.1158/2159-8290.CD-14-0729.

(96) Houben, R.; Becker, J. C.; Kappel, A.; Terheyden, P.; Bröcker, E. B.; Goettz, R.; Rapp, U. R. Constitutive Activation of the Ras-Raf Signaling Pathway in Metastatic Melanoma Is Associated with Poor Prognosis. *J. Carcinog.* **2004**, *3*. https://doi.org/10.1186/1477-3163-3-6.

(97) Liu, Y.; Sheikh, M. S. Melanoma: Molecular Pathogenesis and Therapeutic Management. *Mol. Cell. Pharmacol.* **2014**, *6* (3), 31–44. https://doi.org/10.4255/mcpharmacol.14.03.

(98) Adler, N. R.; Haydon, A.; McLean, C. A.; Kelly, J. W.; Mar, V. J. Metastatic Pathways in Patients with Cutaneous Melanoma. *Pigment Cell and Melanoma Research*. Blackwell Publishing Ltd January 1, 2017, pp 13–27. https://doi.org/10.1111/pcmr.12544.

(99) Hodis, E.; Watson, I. R.; Kryukov, G. V.; Arold, S. T.; Imielinski, M.; Theurillat, J. P.; Nickerson, E.; Auclair, D.; Li, L.; Place, C.; et al. A Landscape of Driver Mutations in

Melanoma. *Cell* **2012**, *150* (2), 251–263. https://doi.org/10.1016/j.cell.2012.06.024.
(100) Dantonio, P. M.; Klein, M. O.; Freire, M. R. V. B.; Araujo, C. N.; Chiacetti, A. C.; Correa, R. G. Exploring Major Signaling Cascades in Melanomagenesis: A Rationale Route for Targetted Skin Cancer Therapy. *Bioscience Reports*. Portland Press Ltd October 2, 2018, p 20180511. https://doi.org/10.1042/BSR20180511.
(101) Chamcheu, J. C.; Roy, T.; Uddin, M. B.; Banang-Mbeumi, S.; Chamcheu, R. C. N.; Walker, A. L.; Liu, Y. Y.; Huang, S. Role and Therapeutic Targeting of the PI3K/Akt/MTOR Signaling Pathway in Skin Cancer: A Review of Current Status and Future Trends on Natural and Synthetic Agents Therapy. *Cells*. NLM (Medline) July 31, 2019. https://doi.org/10.3390/cells8080803.
(102) Krasilnikov, M.; Adler, V.; Fuchs, S. Y.; Dong, Z.; Haimovitz-Friedman, A.; Herlyn, M.; Ronai, Z. Contribution of Phosphatidylinositol 3-Kinase to Radiation Resistance in Human Melanoma Cells. *Mol. Carcinog.* **1999**, *24* (1), 64–69. https://doi.org/10.1002/(SICI)1098-2744(199901)24:1<64::AID-MC9>3.0.CO;2-2.
(103) Campbell, P. M.; Der, C. J. Oncogenic Ras and Its Role in Tumor Cell Invasion and Metastasis. *Seminars in Cancer Biology*. Academic Press 2004, pp 105–114. https://doi.org/10.1016/j.semcancer.2003.09.015.
(104) Tamura, M.; Gu, J.; Danen, E. H. J.; Takino, T.; Miyamoto, S.; Yamada, K. M. PTEN Interactions with Focal Adhesion Kinase and Suppression of the Extracellular Matrix-Dependent Phosphatidylinositol 3-Kinase/Akt Cell Survival Pathway. *J. Biol. Chem.* **1999**, *274* (29), 20693–20703. https://doi.org/10.1074/jbc.274.29.20693.
(105) Celebi, J. T.; Shendrik, I.; Silvers, D. N.; Peacocke, M. Identification of PTEN Mutations in Metastatic Melanoma Specimens. *J. Med. Genet.* **2000**, *37* (9), 653–657. https://doi.org/10.1136/jmg.37.9.653.
(106) Wu, H.; Goel, V.; Haluska, F. G. PTEN Signaling Pathways in Melanoma. *Oncogene*. Nature Publishing Group May 19, 2003, pp 3113–3122. https://doi.org/10.1038/sj.onc.1206451.
(107) Curtin, J. A.; Stark, M. S.; Pinkel, D.; Hayward, N. K.; Bastian, B. C. PI3-Kinase Subunits Are Infrequent Somatic Targets in Melanoma [5]. *Journal of Investigative Dermatology*. Springer Nature July 2006, pp 1660–1663. https://doi.org/10.1038/sj.jid.5700311.
(108) Omholt, K.; Kröckel, D.; Ringborg, U.; Hansson, J. Mutations of PIK3CA Are Rare in Cutaneous Melanoma. *Melanoma Res.* **2006**, *16* (2), 197–200. https://doi.org/10.1097/01.cmr.0000200488.77970.e3.
(109) Davies, M. A. The Role of the PI3K-AKT Pathway in Melanoma. *Cancer Journal*. Cancer J March 2012, pp 142–147. https://doi.org/10.1097/PPO.0b013e31824d448c.
(110) Tsao, H.; Zhang, X.; Benoit, E.; Haluska, F. G. Identification of PTEN/MMAC1 Alterations in Uncultured Melanomas and Melanoma Cell Lines. *Oncogene* **1998**, *16* (26), 3397–3402. https://doi.org/10.1038/sj.onc.1201881.
(111) Fecher, L. A.; Cummings, S. D.; Keefe, M. J.; Alani, R. M. Toward a Molecular Classification of Melanoma. *Journal of Clinical Oncology*. J Clin Oncol April 20, 2007, pp 1606–1620. https://doi.org/10.1200/JCO.2006.06.0442.
(112) Komiya, Y.; Habas, R. Wnt Signal Transduction Pathways. *Organogenesis*. Landes Bioscience 2008, pp 68–75. https://doi.org/10.4161/org.4.2.5851.
(113) Mosimann, C.; Hausmann, G.; Basler, K. β-Catenin Hits Chromatin: Regulation of Wnt Target Gene Activation. *Nature Reviews Molecular Cell Biology*. Nat Rev Mol Cell Biol

April 2009, pp 276–286. https://doi.org/10.1038/nrm2654.
(114) Shang, S.; Hua, F.; Hu, Z. W. The Regulation of β-Catenin Activity and Function in Cancer: Therapeutic Opportunities. *Oncotarget*. Impact Journals LLC 2017, pp 33972–33989. https://doi.org/10.18632/oncotarget.15687.
(115) Kim, W. K.; Kwon, Y.; Jang, M.; Park, M.; Kim, J.; Cho, S.; Jang, D. G.; Lee, W. Bin; Jung, S. H.; Choi, H. J.; et al. β-Catenin Activation down-Regulates Cell-Cell Junction-Related Genes and Induces Epithelial-to-Mesenchymal Transition in Colorectal Cancers. *Sci. Rep.* **2019**, *9* (1), 1–15. https://doi.org/10.1038/s41598-019-54890-9.
(116) Ploper, D.; De Robertis, E. M. The MITF Family of Transcription Factors: Role in Endolysosomal Biogenesis, Wnt Signaling, and Oncogenesis. *Pharmacol. Res.* **2015**, *99*, 36–43. https://doi.org/10.1016/j.phrs.2015.04.006.
(117) Logan, C. Y.; Nusse, R. The Wnt Signaling Pathway in Development and Disease. *Annual Review of Cell and Developmental Biology*. Annu Rev Cell Dev Biol 2004, pp 781–810. https://doi.org/10.1146/annurev.cellbio.20.010403.113126.
(118) Richardson, A.; Kovacevic, Z.; Richardson, D. R. Iron Chelation: Inhibition of Key Signaling Pathways in the Induction of the Epithelial Mesenchymal Transition in Pancreatic Cancer and Other Tumors. *Crit. Rev. Oncog.* **2013**, *18* (5), 409–434. https://doi.org/10.1615/CritRevOncog.2013007921.
(119) Kulikova ; A, K. V. V; Kibardin, P. *Wnt Signaling PathWay and Its Significance for Melanoma Development Ligands and Receptors of Wnt Signaling Pathway*; 2012; Vol. 1.
(120) Delmas, V.; Beermann, F.; Martinozzi, S.; Carreira, S.; Ackermann, J.; Kumasaka, M.; Denat, L.; Goodall, J.; Luciani, F.; Viros, A.; et al. β-Catenin Induces Immortalization of Melanocytes by Suppressing P16INK4a Expression and Cooperates with N-Ras in Melanoma Development. *Genes Dev.* **2007**, *21* (22), 2923–2935. https://doi.org/10.1101/gad.450107.
(121) Webster, M. R.; Weeraratna, A. T. A Wnt-Er Migration: The Confusing Role of β-Catenin in Melanoma Metastasis. *Science Signaling*. Sci Signal March 26, 2013. https://doi.org/10.1126/scisignal.2004114.
(122) Grossmann, A. H.; Yoo, J. H.; Clancy, J.; Sorensen, L. K.; Sedgwick, A.; Tong, Z.; Ostanin, K.; Rogers, A.; Grossmann, K. F.; Tripp, S. R.; et al. The Small GTPase ARF6 Stimulates β-Catenin Transcriptional Activity during WNT5A-Mediated Melanoma Invasion and Metastasis. *Sci. Signal.* **2013**, *6* (265). https://doi.org/10.1126/scisignal.2003398.
(123) Mikels, A. J.; Nusse, R. Purified Wnt5a Protein Activates or Inhibits β-Catenin-TCF Signaling Depending on Receptor Context. *PLoS Biol.* **2006**, *4* (4), 570–582. https://doi.org/10.1371/journal.pbio.0040115.
(124) Hayward, N. K.; Wilmott, J. S.; Waddell, N.; Johansson, P. A.; Field, M. A.; Nones, K.; Patch, A. M.; Kakavand, H.; Alexandrov, L. B.; Burke, H.; et al. Whole-Genome Landscapes of Major Melanoma Subtypes. *Nature* **2017**, *545* (7653), 175–180. https://doi.org/10.1038/nature22071.
(125) Mar, V. J.; Wong, S. Q.; Li, J.; Scolyer, R. A.; McLean, C.; Papenfuss, A. T.; Tothill, R. W.; Kakavand, H.; Mann, G. J.; Thompson, J. F.; et al. BRAF/NRAS Wild-Type Melanomas Have a High Mutation Load Correlating with Histologic and Molecular Signatures of UV Damage. *Clin. Cancer Res.* **2013**, *19* (17), 4589–4598. https://doi.org/10.1158/1078-0432.CCR-13-0398.
(126) Akbani, R.; Akdemir, K. C.; Aksoy, B. A.; Albert, M.; Ally, A.; Amin, S. B.; Arachchi, H.;

Arora, A.; Auman, J. T.; Ayala, B.; et al. Genomic Classification of Cutaneous Melanoma. *Cell* **2015**, *161* (7), 1681–1696. https://doi.org/10.1016/j.cell.2015.05.044.

(127) Scheffzek, K.; Welti, S. Neurofibromin: Protein Domains and Functional Characteristics. In *Neurofibromatosis Type 1: Molecular and Cellular Biology*; Springer-Verlag Berlin Heidelberg, 2013; pp 305–326. https://doi.org/10.1007/978-3-642-32864-0_20.

(128) Kiuru, M.; Busam, K. J. The NF1 Gene in Tumor Syndromes and Melanoma. *Laboratory Investigation*. Nature Publishing Group February 1, 2017, pp 146–157. https://doi.org/10.1038/labinvest.2016.142.

(129) Gibney, G. T.; Smalley, K. S. M. An Unholy Alliance: Cooperation between BRAF and NF1 in Melanoma Development and BRAF Inhibitor Resistance. *Cancer Discov.* **2013**, *3* (3), 260–263. https://doi.org/10.1158/2159-8290.CD-13-0017.

(130) Güllülü, Ö.; Hehlgans, S.; Rödel, C.; Fokas, E.; Rödel, F. Tumor Suppressor Protein P53 and Inhibitor of Apoptosis Proteins in Colorectal Cancer—a Promising Signaling Network for Therapeutic Interventions. *Cancers (Basel).* **2021**, *13* (4), 1–22. https://doi.org/10.3390/cancers13040624.

(131) Rivlin, N.; Brosh, R.; Oren, M.; Rotter, V. Mutations in the P53 Tumor Suppressor Gene: Important Milestones at the Various Steps of Tumorigenesis. *Genes and Cancer*. Impact Journals, LLC April 2011, pp 466–474. https://doi.org/10.1177/1947601911408889.

(132) Blandino, G.; Di Agostino, S. New Therapeutic Strategies to Treat Human Cancers Expressing Mutant P53 Proteins. *Journal of Experimental and Clinical Cancer Research*. BioMed Central Ltd. February 15, 2018, pp 1–13. https://doi.org/10.1186/s13046-018-0705-7.

(133) Martincorena, I.; Campbell, P. J. Somatic Mutation in Cancer and Normal Cells. *Science*. American Association for the Advancement of Science September 25, 2015, pp 1483–1489. https://doi.org/10.1126/science.aab4082.

(134) Albino, A. P.; Vidal, M. J.; Mc Nutt, N. S.; Shea, C. R.; Prieto, V. G.; Nanus, D. M.; Palmer, J. M.; Hayward, N. K. Mutation and Expression of the P53 Gene in Human Malignant Melanoma. *Melanoma Res.* **1994**, *4* (1), 35–45. https://doi.org/10.1097/00008390-199402000-00006.

(135) O'Connor, D. P.; Kay, E. W.; Leader, M.; Murphy, G. M.; Atkins, G. J.; Mabruk, M. J. E. M. F. Altered P53 Expression in Benign and Malignant Skin Lesions from Renal Transplant Recipients and Immunocompetent Patients with Skin Cancer: Correlation with Human Papillomaviruses? *Diagnostic Mol. Pathol.* **2001**, *10* (3), 190–199. https://doi.org/10.1097/00019606-200109000-00007.

(136) Houben, R.; Hesbacher, S.; Schmid, C. P.; Kauczok, C. S.; Flohr, U.; Haferkamp, S.; Müller, C. S. L.; Schrama, D.; Wischhusen, J.; Becker, J. C. High-Level Expression of Wild-Type P53 in Melanoma Cells Is Frequently Associated with Inactivity in P53 Reporter Gene Assays. *PLoS One* **2011**, *6* (7). https://doi.org/10.1371/journal.pone.0022096.

(137) Muro, S. Alterations in Cellular Processes Involving Vesicular Trafficking and Implications in Drug Delivery. *Biomimetics*. MDPI Multidisciplinary Digital Publishing Institute September 1, 2018. https://doi.org/10.3390/biomimetics3030019.

(138) Demirsoy, S.; Martin, S.; Maes, H.; Agostinis, P. Adapt, Recycle, and Move on: Proteostasis and Trafficking Mechanisms in Melanoma. *Frontiers in Oncology*. Frontiers Media S.A. November 15, 2016, p 1. https://doi.org/10.3389/fonc.2016.00240.

(139) Brennan, K.; Martin, K.; FitzGerald, S. P.; O'Sullivan, J.; Wu, Y.; Blanco, A.; Richardson,

C.; Mc Gee, M. M. A Comparison of Methods for the Isolation and Separation of Extracellular Vesicles from Protein and Lipid Particles in Human Serum. *Sci. Rep.* **2020**, *10* (1). https://doi.org/10.1038/s41598-020-57497-7.

(140) Raposo, G.; Stoorvogel, W. Extracellular Vesicles: Exosomes, Microvesicles, and Friends. *Journal of Cell Biology*. The Rockefeller University Press February 2013, pp 373–383. https://doi.org/10.1083/jcb.201211138.

(141) Zhang, Y.; Liu, Y.; Liu, H.; Tang, W. H. Exosomes: Biogenesis, Biologic Function and Clinical Potential. *Cell and Bioscience*. BioMed Central February 15, 2019. https://doi.org/10.1186/s13578-019-0282-2.

(142) Liu, J.; Fukunaga-Kalabis, M.; Li, L.; Herlyn, M. Developmental Pathways Activated in Melanocytes and Melanoma. *Archives of Biochemistry and Biophysics*. Academic Press Inc. December 15, 2014, pp 13–21. https://doi.org/10.1016/j.abb.2014.07.023.

(143) Thomas, A. J.; Erickson, C. A. The Making of a Melanocyte: The Specification of Melanoblasts from the Neural Crest. *Pigment Cell and Melanoma Research*. Pigment Cell Melanoma Res December 2008, pp 598–610. https://doi.org/10.1111/j.1755-148X.2008.00506.x.

(144) Mouret, S.; Philippe, C.; Gracia-Chantegrel, J.; Banyasz, A.; Karpati, S.; Markovitsi, D.; Douki, T. UVA-Induced Cyclobutane Pyrimidine Dimers in DNA: A Direct Photochemical Mechanism? *Org. Biomol. Chem.* **2010**, *8* (7), 1706–1711. https://doi.org/10.1039/b924712b.

(145) Hanahan, D.; Weinberg, R. A. The Hallmarks of Cancer. *Cell*. Cell January 7, 2000, pp 57–70. https://doi.org/10.1016/S0092-8674(00)81683-9.

(146) Nieder, C.; Thamm, R.; Astner, S. T.; Molls, M. Disease Presentation and Treatment Outcome in Very Young Patients with Brain Metastases from Lung Cancer. *Onkologie* **2008**, *31* (6), 305–308. https://doi.org/10.1159/000129621.

(147) Redmer, T. Deciphering Mechanisms of Brain Metastasis in Melanoma - the Gist of the Matter. *Molecular Cancer*. BioMed Central Ltd. July 27, 2018. https://doi.org/10.1186/s12943-018-0854-5.

(148) Aasen, S. N.; Parajuli, H.; Hoang, T.; Feng, Z.; Stokke, K.; Wang, J.; Roy, K.; Bjerkvig, R.; Knappskog, S.; Thorsen, F. Effective Treatment of Metastatic Melanoma by Combining Mapk and Pi3k Signaling Pathway Inhibitors. *Int. J. Mol. Sci.* **2019**, *20* (17), 1–19. https://doi.org/10.3390/ijms20174235.

(149) Hapach, L. A.; Mosier, J. A.; Wang, W.; Reinhart-King, C. A. Engineered Models to Parse Apart the Metastatic Cascade. *npj Precis. Oncol.* **2019**, *3* (1), 1–8. https://doi.org/10.1038/s41698-019-0092-3.

(150) Hanahan, D.; Weinberg, R. A. Hallmarks of Cancer: The next Generation. *Cell*. Cell March 4, 2011, pp 646–674. https://doi.org/10.1016/j.cell.2011.02.013.

(151) Tsai, J. H.; Yang, J. Epithelial-Mesenchymal Plasticity in Carcinoma Metastasis. *Genes and Development*. Genes Dev October 15, 2013, pp 2192–2206. https://doi.org/10.1101/gad.225334.113.

(152) Wilson, R. B. Hypoxia, Cytokines and Stromal Recruitment: Parallels between Pathophysiology of Encapsulating Peritoneal Sclerosis, Endometriosis and Peritoneal Metastasis. *Pleura and Peritoneum*. Walter de Gruyter GmbH 2018. https://doi.org/10.1515/pp-2018-0103.

(153) Guo, W.; Giancotti, F. G. Integrin Signalling during Tumour Progression. *Nature Reviews*

Molecular Cell Biology. Nat Rev Mol Cell Biol October 2004, pp 816–826. https://doi.org/10.1038/nrm1490.

(154) Wrobel, J. K.; Toborek, M. Blood–Brain Barrier Remodeling during Brain Metastasis Formation. *Molecular Medicine*. Uninversity of Michigan 2016, pp 32–40. https://doi.org/10.2119/molmed.2015.00207.

(155) Seano, G.; Jain, R. K. Vessel Co-Option in Glioblastoma: Emerging Insights and Opportunities. *Angiogenesis*. Springer February 1, 2020, pp 9–16. https://doi.org/10.1007/s10456-019-09691-z.

(156) Gong, X.; Hou, Z.; Endsley, M. P.; Gronseth, E. I.; Rarick, K. R.; Jorns, J. M.; Yang, Q.; Du, Z.; Yan, K.; Bordas, M. L.; et al. Interaction of Tumor Cells and Astrocytes Promotes Breast Cancer Brain Metastases through TGF-B2/ANGPTL4 Axes. *npj Precis. Oncol.* **2019**, *3* (1), 1–9. https://doi.org/10.1038/s41698-019-0094-1.

(157) Ju, R. J.; Stehbens, S. J.; Haass, N. K. The Role of Melanoma Cell-Stroma Interaction in Cell Motility, Invasion, and Metastasis. *Frontiers in Medicine*. Frontiers Media S.A. 2018, p 307. https://doi.org/10.3389/fmed.2018.00307.

(158) Paget, S. THE DISTRIBUTION OF SECONDARY GROWTHS IN CANCER OF THE BREAST. *Lancet* **1889**, *133* (3421), 571–573. https://doi.org/10.1016/S0140-6736(00)49915-0.

(159) McConnell, H. L.; Kersch, C. N.; Woltjer, R. L.; Neuwelt, E. A. The Translational Significance of the Neurovascular Unit. *Journal of Biological Chemistry*. American Society for Biochemistry and Molecular Biology Inc. January 20, 2017, pp 762–770. https://doi.org/10.1074/jbc.R116.760215.

(160) Sofroniew, M. V; Vinters, H. V. Astrocytes: Biology and Pathology. **2009**. https://doi.org/10.1007/s00401-009-0619-8.

(161) Wolburg, H.; Noell, S.; Mack, A.; Wolburg-Buchholz, K.; Fallier-Becker, P. Brain Endothelial Cells and the Glio-Vascular Complex. *Cell and Tissue Research*. Springer January 16, 2009, pp 75–96. https://doi.org/10.1007/s00441-008-0658-9.

(162) Fidler, I. J.; Yano, S.; Zhang, R. D.; Fujimaki, T.; Bucana, C. D. The Seed and Soil Hypothesis: Vascularisation and Brain Metastases. *Lancet Oncology*. Lancet Publishing Group 2002, pp 53–57. https://doi.org/10.1016/S1470-2045(01)00622-2.

(163) Daphu, I.; Sundstrøm, T.; Horn, S.; Huszthy, P. C.; Niclou, S. P.; Sakariassen, P.; Immervoll, H.; Miletic, H.; Bjerkvig, R.; Thorsen, F. In Vivo Animal Models for Studying Brain Metastasis: Value and Limitations. *Clin. Exp. Metastasis* **2013**, *30* (5), 695–710. https://doi.org/10.1007/s10585-013-9566-9.

(164) Liu, Y.; Cao, X. Characteristics and Significance of the Pre-Metastatic Niche. *Cancer Cell*. Cell Press November 14, 2016, pp 668–681. https://doi.org/10.1016/j.ccell.2016.09.011.

(165) Izraely, S.; Witz, I. P. <scp>Site-specific</Scp> Metastasis: A Cooperation between Cancer Cells and the Metastatic Microenvironment. *Int. J. Cancer* **2020**, ijc.33247. https://doi.org/10.1002/ijc.33247.

(166) Liu, Y.; Carson-Walter, E. B.; Cooper, A.; Winans, B. N.; Johnson, M. D.; Walter, K. A. Vascular Gene Expression Patterns Are Conserved in Primary and Metastatic Brain Tumors. *J. Neurooncol.* **2010**, *99* (1), 13–24. https://doi.org/10.1007/s11060-009-0105-0.

(167) Harper, J.; Moses, M. A. Molecular Regulation of Tumor Angiogenesis: Mechanisms and Therapeutic Implications. *EXS*. EXS 2006, pp 223–268. https://doi.org/10.1007/3-7643-7378-4_10.

(168) Yekula, A.; Yekula, A.; Muralidharan, K.; Kang, K.; Carter, B. S.; Balaj, L. Extracellular

Vesicles in Glioblastoma Tumor Microenvironment. *Frontiers in Immunology*. Frontiers Media S.A. January 21, 2020, p 3137. https://doi.org/10.3389/fimmu.2019.03137.

(169) Placone, A. L.; Quiñones-Hinojosa, A.; Searson, P. C. The Role of Astrocytes in the Progression of Brain Cancer: Complicating the Picture of the Tumor Microenvironment. *Tumor Biology*. Springer Netherlands January 1, 2016, pp 61–69. https://doi.org/10.1007/s13277-015-4242-0.

(170) Weber, G. F.; Ashkar, S. Molecular Mechanisms of Tumor Dissemination in Primary and Metastatic Brain Cancers. *Brain Res. Bull.* **2000**, *53* (4), 421–424. https://doi.org/10.1016/S0361-9230(00)00379-8.

(171) Da Mesquita, S.; Louveau, A.; Vaccari, A.; Smirnov, I.; Cornelison, R. C.; Kingsmore, K. M.; Contarino, C.; Onengut-Gumuscu, S.; Farber, E.; Raper, D.; et al. Functional Aspects of Meningeal Lymphatics in Ageing and Alzheimer's Disease. *Nature* **2018**, *560* (7717), 185–191. https://doi.org/10.1038/s41586-018-0368-8.

(172) Arshad, F.; Wang, L.; Sy, C.; Avraham, S.; Avraham, H. K. Blood-Brain Barrier Integrity and Breast Cancer Metastasis to the Brain. *Patholog. Res. Int.* **2011**, *2011*, 1–12. https://doi.org/10.4061/2011/920509.

(173) Feustel, S. M.; Meissner, M.; Liesenfeld, O. Toxoplasma Gondii and the Blood-Brain Barrier. *Virulence*. Taylor and Francis Inc. 2012, pp 182–192. https://doi.org/10.4161/viru.19004.

(174) Daneman, R.; Prat, A. The Blood–Brain Barrier. *Cold Spring Harb. Perspect. Biol.* **2015**, *7* (1). https://doi.org/10.1101/cshperspect.a020412.

(175) Dotiwala, A. K.; McCausland, C.; Samra, N. S. *Anatomy, Head and Neck, Blood Brain Barrier*; StatPearls Publishing, 2020.

(176) Pardridge, W. M. The Blood-Brain Barrier: Bottleneck in Brain Drug Development. *NeuroRx* **2005**, *2* (1), 3–14. https://doi.org/10.1602/neurorx.2.1.3.

(177) Stolp, H. B.; Dziegielewska, K. M. Review: Role of Developmental Inflammation and Blood-Brain Barrier Dysfunction in Neurodevelopmental and Neurodegenerative Diseases. *Neuropathol. Appl. Neurobiol.* **2009**, *35* (2), 132–146. https://doi.org/10.1111/j.1365-2990.2008.01005.x.

(178) Neuwelt, E.; Abbott, N. J.; Abrey, L.; Banks, W. A.; Blakley, B.; Davis, T.; Engelhardt, B.; Grammas, P.; Nedergaard, M.; Nutt, J.; et al. Strategies to Advance Translational Research into Brain Barriers. *The Lancet Neurology*. Lancet Neurol January 2008, pp 84–96. https://doi.org/10.1016/S1474-4422(07)70326-5.

(179) CRONE, C. The Permeability of Brain Capillaries to Non-Electrolytes. *Acta Physiol. Scand.* **1965**, *64* (4), 407–417. https://doi.org/10.1111/j.1748-1716.1965.tb04198.x.

(180) Abbott, N. J.; Rönnbäck, L.; Hansson, E. Astrocyte-Endothelial Interactions at the Blood-Brain Barrier. *Nature Reviews Neuroscience*. Nature Publishing Group January 2006, pp 41–53. https://doi.org/10.1038/nrn1824.

(181) Luissint, A. C.; Artus, C.; Glacial, F.; Ganeshamoorthy, K.; Couraud, P. O. Tight Junctions at the Blood Brain Barrier: Physiological Architecture and Disease-Associated Dysregulation. *Fluids and Barriers of the CNS*. Fluids Barriers CNS November 9, 2012. https://doi.org/10.1186/2045-8118-9-23.

(182) Janzer, R. C.; Raff, M. C. Astrocytes Induce Blood-Brain Barrier Properties in Endothelial Cells. *Nature* **1987**, *325* (6101), 253–257. https://doi.org/10.1038/325253a0.

(183) Sarkaria, J. N.; Hu, L. S.; Parney, I. F.; Pafundi, D. H.; Brinkmann, D. H.; Laack, N. N.;

Giannini, C.; Burns, T. C.; Kizilbash, S. H.; Laramy, J. K.; et al. Is the Blood-Brain Barrier Really Disrupted in All Glioblastomas? A Critical Assessment of Existing Clinical Data. *Neuro. Oncol.* **2018**, *20* (2), 184–191. https://doi.org/10.1093/neuonc/nox175.

(184) Arvanitis, C. D.; Ferraro, G. B.; Jain, R. K. The Blood–Brain Barrier and Blood–Tumour Barrier in Brain Tumours and Metastases. *Nature Reviews Cancer*. Nature Research January 1, 2020, pp 26–41. https://doi.org/10.1038/s41568-019-0205-x.

(185) Fazakas, C.; Wilhelm, I.; Nagyoszi, P.; Farkas, A. E.; Haskó, J.; Molnár, J.; Bauer, H.; Bauer, H. C.; Ayaydin, F.; Dung, N. T. K.; et al. Transmigration of Melanoma Cells through the Blood-Brain Barrier: Role of Endothelial Tight Junctions and Melanoma-Released Serine Proteases. *PLoS One* **2011**, *6* (6). https://doi.org/10.1371/journal.pone.0020758.

(186) Puré, E.; Blomberg, R. Pro-Tumorigenic Roles of Fibroblast Activation Protein in Cancer: Back to the Basics. *Oncogene*. Nature Publishing Group August 9, 2018, pp 4343–4357. https://doi.org/10.1038/s41388-018-0275-3.

(187) Mentlein, R.; Hattermann, K.; Hemion, C.; Jungbluth, A. A.; Held-Feindt, J. Expression and Role of the Cell Surface Protease Seprase/Fibroblast Activation Protein-α (FAP-α) in Astroglial Tumors. *Biol. Chem.* **2011**, *392* (3), 199–207. https://doi.org/10.1515/BC.2010.119.

(188) Azad, T. D.; Pan, J.; Connolly, I. D.; Remington, A.; Wilso n, C. M.; Grant, G. A. Therapeutic Strategies to Improve Drug Delivery across the Blood-Brain Barrier. *Neurosurg. Focus* **2015**, *38* (3), E9. https://doi.org/10.3171/2014.12.FOCUS14758.

(189) Haumann, R.; Videira, J. C.; Kaspers, G. J. L.; van Vuurden, D. G.; Hulleman, E. Overview of Current Drug Delivery Methods Across the Blood–Brain Barrier for the Treatment of Primary Brain Tumors. *CNS Drugs*. Adis November 1, 2020, pp 1121–1131. https://doi.org/10.1007/s40263-020-00766-w.

(190) Dong, X. Current Strategies for Brain Drug Delivery. *Theranostics*. Ivyspring International Publisher 2018, pp 1481–1493. https://doi.org/10.7150/thno.21254.

(191) MM Patel, B. P. Crossing the Blood–Brain Barrier: Recent Advances in Drug Delivery to the Brain. *CNS Drugs* **2017**, *31* (2), 109–133.

(192) Fan, J.; Yang, J.; Jiang, Z. Prediction of Central Nervous System Side Effects Through Drug Permeability to Blood-Brain Barrier and Recommendation Algorithm. *J. Comput. Biol.* **2018**, *25* (4), 435–443. https://doi.org/10.1089/cmb.2017.0149.

(193) Shawkat, H.; Westwood, M.-M.; Mortimer, A. Mannitol: A Review of Its Clinical Uses. *Contin. Educ. Anaesth. Crit. Care Pain* **2012**, *12* (2), 82–85. https://doi.org/10.1093/bjaceaccp/mkr063.

(194) Dupont, M.; Souriant, S.; Lugo-Villarino, G.; Maridonneau-Parini, I.; Vérollet, C. Tunneling Nanotubes: Intimate Communication between Myeloid Cells. *Frontiers in Immunology*. Frontiers Media S.A. January 25, 2018, p 25. https://doi.org/10.3389/fimmu.2018.00043.

(195) Gerdes, H. H.; Rustom, A.; Wang, X. Tunneling Nanotubes, an Emerging Intercellular Communication Route in Development. *Mech. Dev.* **2013**, *130* (6–8), 381–387. https://doi.org/10.1016/j.mod.2012.11.006.

(196) Rustom, A. The Missing Link: Does Tunnelling Nanotube-Based Supercellularity Provide a New Understanding of Chronic and Lifestyle Diseases? *Open Biology*. Royal Society of London June 1, 2016. https://doi.org/10.1098/rsob.160057.

(197) McCoy-Simandle, K.; Hanna, S. J.; Cox, D. Exosomes and Nanotubes: Control of Immune

Cell Communication. *International Journal of Biochemistry and Cell Biology*. Elsevier Ltd February 1, 2016, pp 44–54. https://doi.org/10.1016/j.biocel.2015.12.006.

(198) Venkatesh, V. S.; Lou, E. Tunneling Nanotubes: A Bridge for Heterogeneity in Glioblastoma and a New Therapeutic Target? *Cancer Rep.* **2019**, *2* (6), e1185. https://doi.org/10.1002/cnr2.1185.

(199) Lou, E.; Fujisawa, S.; Morozov, A.; Barlas, A.; Romin, Y.; Dogan, Y.; Gholami, S.; Moreira, A. L.; Manova-Todorova, K.; Moore, M. A. S. Tunneling Nanotubes Provide a Unique Conduit for Intercellular Transfer of Cellular Contents in Human Malignant Pleural Mesothelioma. *PLoS One* **2012**, *7* (3), e33093. https://doi.org/10.1371/journal.pone.0033093.

(200) Omsland, M.; Bruserud, Ø.; Gjertsen, B. T.; Andresen, V. Tunneling Nanotube (TNT) Formation Is Downregulated by Cytarabine and NF-KB Inhibition in Acute Myeloid Leukemia (AML). *Oncotarget* **2017**, *8* (5), 7946–7963. https://doi.org/10.18632/oncotarget.13853.

(201) Austefjord, M. W.; Gerdes, H. H.; Wang, X. Tunneling Nanotubes: Diversity in Morphology and Structure. *Commun. Integr. Biol.* **2014**, *7* (2). https://doi.org/10.4161/cib.27934.

(202) Wang, X.; Veruki, M. L.; Bukoreshtliev, N. V.; Hartveit, E.; Gerdes, H. H. Animal Cells Connected by Nanotubes Can Be Electrically Coupled through Interposed Gap-Junction Channels. *Proc. Natl. Acad. Sci. U. S. A.* **2010**, *107* (40), 17194–17199. https://doi.org/10.1073/pnas.1006785107.

(203) Rustom, A.; Saffrich, R.; Markovic, I.; Walther, P.; Gerdes, H. H. Nanotubular Highways for Intercellular Organelle Transport. *Science (80-.).* **2004**, *303* (5660), 1007–1010. https://doi.org/10.1126/science.1093133.

(204) Lou, E. A Ticket to Ride: The Implications of Direct Intercellular Communication via Tunneling Nanotubes in Peritoneal and Other Invasive Malignancies. *Front. Oncol.* **2020**, *10*, 559548. https://doi.org/10.3389/fonc.2020.559548.

(205) Ariazi, J.; Benowitz, A.; De Biasi, V.; Den Boer, M. L.; Cherqui, S.; Cui, H.; Douillet, N.; Eugenin, E. A.; Favre, D.; Goodman, S.; et al. Tunneling Nanotubes and Gap Junctions–Their Role in Long-Range Intercellular Communication during Development, Health, and Disease Conditions. *Frontiers in Molecular Neuroscience*. Frontiers Media S.A. October 17, 2017. https://doi.org/10.3389/fnmol.2017.00333.

(206) Eugenin, E. A.; Gaskill, P. J.; Berman, J. W. Tunneling Nanotubes (TNT) Are Induced by HIV-Infection of Macrophages: A Potential Mechanism for Intercellular HIV Trafficking. *Cell. Immunol.* **2009**, *254* (2), 142–148. https://doi.org/10.1016/j.cellimm.2008.08.005.

(207) Cselenyák, A.; Pankotai, E.; Horváth, E. M.; Kiss, L.; Lacza, Z. Mesenchymal Stem Cells Rescue Cardiomyoblasts from Cell Death in an in Vitro Ischemia Model via Direct Cell-to-Cell Connections. *BMC Cell Biol.* **2010**, *11*. https://doi.org/10.1186/1471-2121-11-29.

(208) Gousset, K.; Schiff, E.; Langevin, C.; Marijanovic, Z.; Caputo, A.; Browman, D. T.; Chenouard, N.; de Chaumont, F.; Martino, A.; Enninga, J.; et al. Prions Hijack Tunnelling Nanotubes for Intercellular Spread. *Nat. Cell Biol.* **2009**, *11* (3), 328–336. https://doi.org/10.1038/ncb1841.

(209) Hase, K.; Kimura, S.; Takatsu, H.; Ohmae, M.; Kawano, S.; Kitamura, H.; Ito, M.; Watarai, H.; Hazelett, C. C.; Yeaman, C.; et al. M-Sec Promotes Membrane Nanotube Formation by Interacting with Ral and the Exocyst Complex. *Nat. Cell Biol.* **2009**, *11* (12), 1427–1432. https://doi.org/10.1038/ncb1990.

(210) Salter, R. D.; Watkins, S. C. Dynamic Properties of Antigen Uptake and Communication between Dendritic Cells. *Immunologic Research*. Humana Press 2006, pp 211–220. https://doi.org/10.1385/IR:36:1:211.

(211) Rudnicka, D.; Feldmann, J.; Porrot, F.; Wietgrefe, S.; Guadagnini, S.; Prévost, M.-C.; Estaquier, J.; Haase, A. T.; Sol-Foulon, N.; Schwartz, O. Simultaneous Cell-to-Cell Transmission of Human Immunodeficiency Virus to Multiple Targets through Polysynapses. *J. Virol.* **2009**, *83* (12), 6234–6246. https://doi.org/10.1128/jvi.00282-09.

(212) Galkina, S. I.; Stadnichuk, V. I.; Molotkovsky, J. G.; Romanova, J. M.; Sud'ina, G. F.; Klein, T. Microbial Alkaloid Staurosporine Induces Formation of Nanometer-Wide Membrane Tubular Extensions (Cytonemes, Membrane Tethers) in Human Neutrophils. *Cell Adhes. Migr.* **2010**, *4* (1), 32–38. https://doi.org/10.4161/cam.4.1.10314.

(213) Koyanagi, M.; Brandes, R. P.; Haendeler, J.; Zeiher, A. M.; Dimmeler, S. Cell-to-Cell Connection of Endothelial Progenitor Cells with Cardiac Myocytes by Nanotubes: A Novel Mechanism for Cell Fate Changes? *Circ. Res.* **2005**, *96* (10), 1039–1041. https://doi.org/10.1161/01.RES.0000168650.23479.0c.

(214) Gurke, S.; Barroso, J. F. V.; Hodneland, E.; Bukoreshtliev, N. V.; Schlicker, O.; Gerdes, H. H. Tunneling Nanotube (TNT)-like Structures Facilitate a Constitutive, Actomyosin-Dependent Exchange of Endocytic Organelles between Normal Rat Kidney Cells. *Exp. Cell Res.* **2008**, *314* (20), 3669–3683. https://doi.org/10.1016/j.yexcr.2008.08.022.

(215) Gerdes, H. H.; Carvalho, R. N. Intercellular Transfer Mediated by Tunneling Nanotubes. *Current Opinion in Cell Biology*. Curr Opin Cell Biol August 2008, pp 470–475. https://doi.org/10.1016/j.ceb.2008.03.005.

(216) Sisakhtnezhad, S.; Khosravi, L. Emerging Physiological and Pathological Implications of Tunneling Nanotubes Formation between Cells. *European Journal of Cell Biology*. Elsevier GmbH October 1, 2015, pp 429–443. https://doi.org/10.1016/j.ejcb.2015.06.010.

(217) Roehlecke, C.; Schmidt, M. H. H. Tunneling Nanotubes and Tumor Microtubes in Cancer. *Cancers*. MDPI AG April 1, 2020, p 857. https://doi.org/10.3390/cancers12040857.

(218) Osswald, M.; Jung, E.; Sahm, F.; Solecki, G.; Venkataramani, V.; Blaes, J.; Weil, S.; Horstmann, H.; Wiestler, B.; Syed, M.; et al. Brain Tumour Cells Interconnect to a Functional and Resistant Network. *Nature* **2015**, *528* (7580), 93–98. https://doi.org/10.1038/nature16071.

(219) Matejka, N.; Reindl, J. Perspectives of Cellular Communication through Tunneling Nanotubes in Cancer Cells and the Connection to Radiation Effects. *Radiation Oncology*. BioMed Central Ltd. December 3, 2019, pp 1–11. https://doi.org/10.1186/s13014-019-1416-8.

(220) Desir, S.; O'Hare, P.; Vogel, R. I.; Sperduto, W.; Sarkari, A.; Dickson, E. L.; Wong, P.; Nelson, A. C.; Fong, Y.; Steer, C. J.; et al. Chemotherapy-Induced Tunneling Nanotubes Mediate Intercellular Drug Efflux in Pancreatic Cancer. *Sci. Rep.* **2018**, *8* (1), 9484. https://doi.org/10.1038/s41598-018-27649-x.

(221) Veranič, P.; Lokar, M.; Schütz, G. J.; Weghuber, J.; Wieser, S.; Hägerstrand, H.; Kralj-Iglič, V.; Iglič, A. Different Types of Cell-to-Cell Connections Mediated by Nanotubular Structures. *Biophys. J.* **2008**, *95* (9), 4416–4425. https://doi.org/10.1529/biophysj.108.131375.

(222) Ady, J. W.; Desir, S.; Thayanithy, V.; Vogel, R. I.; Moreira, A. L.; Downey, R. J.; Fong, Y.; Manova-Todorova, K.; Moore, M. A. S.; Lou, E. Intercellular Communication in Malignant Pleural Mesothelioma: Properties of Tunneling Nanotubes. *Front. Physiol.*

2014, *5*. https://doi.org/10.3389/fphys.2014.00400.

(223) Pasquier, J.; Guerrouahen, B. S.; Al Thawadi, H.; Ghiabi, P.; Maleki, M.; Abu-Kaoud, N.; Jacob, A.; Mirshahi, M.; Galas, L.; Rafii, S.; et al. Preferential Transfer of Mitochondria from Endothelial to Cancer Cells through Tunneling Nanotubes Modulates Chemoresistance. *J. Transl. Med.* **2013**, *11* (1). https://doi.org/10.1186/1479-5876-11-94.

(224) Desir, S.; O'Hare, P.; Vogel, R. I.; Sperduto, W.; Sarkari, A.; Dickson, E. L.; Wong, P.; Nelson, A. C.; Fong, Y.; Steer, C. J.; et al. Chemotherapy-Induced Tunneling Nanotubes Mediate Intercellular Drug Efflux in Pancreatic Cancer. *Sci. Rep.* **2018**, *8* (1), 9484. https://doi.org/10.1038/s41598-018-27649-x.

(225) Reichert, D.; Scheinpflug, J.; Karbanová, J.; Freund, D.; Bornhäuser, M.; Corbeil, D. Tunneling Nanotubes Mediate the Transfer of Stem Cell Marker CD133 between Hematopoietic Progenitor Cells. *Exp. Hematol.* **2016**, *44* (11), 1092-1112.e2. https://doi.org/10.1016/j.exphem.2016.07.006.

(226) Dieriks, B. V.; Park, T. I. H.; Fourie, C.; Faull, R. L. M.; Dragunow, M.; Curtis, M. A. α-Synuclein Transfer through Tunneling Nanotubes Occurs in SH-SY5Y Cells and Primary Brain Pericytes from Parkinson's Disease Patients. *Sci. Rep.* **2017**, *7*. https://doi.org/10.1038/srep42984.

(227) Ljubojevic, N.; Henderson, J. M.; Zurzolo, C. The Ways of Actin: Why Tunneling Nanotubes Are Unique Cell Protrusions. *Trends in Cell Biology*. Elsevier Ltd February 1, 2021, pp 130–142. https://doi.org/10.1016/j.tcb.2020.11.008.

(228) Castro, M. A. A.; Grieneisen, V. A.; De Almeida, R. M. C. Disruption and de Novo Formation of Nanotubular Membrane Extensions in SW620 Colon Carcinoma Cell Line during Cell Division. *Cell Biol. Int.* **2005**, *29* (11), 929–931. https://doi.org/10.1016/j.cellbi.2005.05.013.

(229) Lonser, R. R.; Song, D. K.; Klapper, J.; Hagan, M.; Auh, S.; Kerr, P. B.; Citrin, D. E.; Heiss, J. D.; Camphausen, K.; Rosenberg, S. A. Surgical Management of Melanoma Brain Metastases in Patients Treated with Immunotherapy: Clinical Article. *J. Neurosurg.* **2011**, *115* (1), 30–36. https://doi.org/10.3171/2011.3.JNS091107.

(230) Hatiboglu, M. A.; Wildrick, D. M.; Sawaya, R. The Role of Surgical Resection in Patients with Brain Metastases. *Ecancermedicalscience* **2013**, *7* (1). https://doi.org/10.3332/ecancer.2013.308.

(231) Glitza Oliva, I.; Tawbi, H.; Davies, M. A. Melanoma Brain Metastases: Current Areas of Investigation and Future Directions. *Cancer Journal (United States)*. Lippincott Williams and Wilkins January 1, 2017, pp 68–74. https://doi.org/10.1097/PPO.0000000000000237.

(232) Goyal, S.; Silk, A. W.; Tian, S.; Mehnert, J.; Danish, S.; Ranjan, S.; Kaufman, H. L. Clinical Management of Multiple Melanoma Brain Metastases a Systematic Review. *JAMA Oncology*. American Medical Association August 1, 2015, pp 668–676. https://doi.org/10.1001/jamaoncol.2015.1206.

(233) Mizuno, T.; Takada, K.; Hasegawa, T.; Yoshida, T.; Murotani, K.; Kobayashi, H.; Sakurai, T.; Yamashita, Y.; Akazawa, N.; Kojima, E. Comparison between Stereotactic Radiosurgery and Whole-brain Radiotherapy for 10-20 Brain Metastases from Non-small Cell Lung Cancer. *Mol. Clin. Oncol.* **2019**, *10* (5), 560–566. https://doi.org/10.3892/mco.2019.1830.

(234) Kalialis, L. V.; Drzewiecki, K. T.; Klyver, H. Spontaneous Regression of Metastases from Melanoma: Review of the Literature. *Melanoma Research*. Melanoma Res October 2009, pp

275–282. https://doi.org/10.1097/CMR.0b013e32832eabd5.
(235) Weiner, L. M.; Surana, R.; Wang, S. Monoclonal Antibodies: Versatile Platforms for Cancer Immunotherapy. *Nature Reviews Immunology*. NIH Public Access May 2010, pp 317–327. https://doi.org/10.1038/nri2744.
(236) Yu, Z.; Si, L. Immunotherapy of Patients with Metastatic Melanoma. *Chinese Clin. Oncol.* **2017**, *6* (2), 1–9. https://doi.org/10.21037/cco.2017.04.01.
(237) Tsai, K. K.; Zarzoso, I.; Daud, A. I. PD-1 and PD-L1 Antibodies for Melanoma. *Hum. Vaccines Immunother.* **2014**, *10* (11), 3111–3116. https://doi.org/10.4161/21645515.2014.983409.
(238) Glitza Oliva, I.; Tawbi, H.; Davies, M. A. Melanoma Brain Metastases: Current Areas of Investigation and Future Directions. *Cancer Journal (United States)*. Lippincott Williams and Wilkins January 1, 2017, pp 68–74. https://doi.org/10.1097/PPO.0000000000000237.
(239) Sanchez, J. N.; Wang, T.; Cohen, M. S. BRAF and MEK Inhibitors: Use and Resistance in BRAF-Mutated Cancers. *Drugs*. Springer International Publishing April 1, 2018, pp 549–566. https://doi.org/10.1007/s40265-018-0884-8.
(240) Chapman, P. B.; Hauschild, A.; Robert, C.; Haanen, J. B.; Ascierto, P.; Larkin, J.; Dummer, R.; Garbe, C.; Testori, A.; Maio, M.; et al. Improved Survival with Vemurafenib in Melanoma with BRAF V600E Mutation. *N. Engl. J. Med.* **2011**, *364* (26), 2507–2516. https://doi.org/10.1056/NEJMoa1103782.
(241) Röck, R.; Mayrhofer, J. E.; Torres-Quesada, O.; Enzler, F.; Raffeiner, A.; Raffeiner, P.; Feichtner, A.; Huber, R. G.; Koide, S.; Taylor, S. S.; et al. BRAF Inhibitors Promote Intermediate BRAF(V600E) Conformations and Binary Interactions with Activated RAS. *Sci. Adv.* **2019**, *5* (8), eaav8463. https://doi.org/10.1126/sciadv.aav8463.
(242) Pascale, F.; Dummer, R.; Ascierto, P. A.; Gogas, H. J.; Arance, A.; Mandala, M.; Liszkay, G.; Garbe, C.; Schadendorf, D.; Krajsova, I.; et al. 【COLUMBUS試験】 BRAF変異切除不能悪性黒色腫に対する一次/二次治療としてのエンコラフェニブ+ビニメチニブ vs ベムラフェニブのランダム化比較第III相試験. *Lancet Oncol* **2018**, *19* (2013), 603–618. https://doi.org/10.1016/S1470-2045(18)30142-6.
(243) Daphu, I.; Horn, S.; Stieber, D.; Varughese, J. K.; Spriet, E.; Dale, H. A.; Skaftnesmo, K. O.; Bjerkvig, R.; Thorsen, F. In Vitro Treatment of Melanoma Brain Metastasis by Simultaneously Targeting the MAPK and PI3K Signaling Pathways. *Int. J. Mol. Sci.* **2014**, *15* (5), 8773–8794. https://doi.org/10.3390/ijms15058773.
(244) Mittapalli, R. K.; Vaidhyanathan, S.; Dudek, A. Z.; Elmquist, W. F. Mechanisms Limiting Distribution of the Threonine-Protein Kinase B-RaF V600E Inhibitor Dabrafenib to the Brain: Implications for the Treatment of Melanoma Brain Metastases. *J. Pharmacol. Exp. Ther.* **2013**, *344* (3), 655–664. https://doi.org/10.1124/jpet.112.201475.
(245) Wilmott, J. S.; Long, G. V.; Howle, J. R.; Haydu, L. E.; Sharma, R. N.; Thompson, J. F.; Kefford, R. F.; Hersey, P.; Scolyer, R. A. Selective BRAF Inhibitors Induce Marked T-Cell Infiltration into Human Metastatic Melanoma. *Clin. Cancer Res.* **2012**, *18* (5), 1386–1394. https://doi.org/10.1158/1078-0432.CCR-11-2479.
(246) Torres-Collado, A. X.; Knott, J.; Jazirehi, A. R. Reversal of Resistance in Targeted Therapy of Metastatic Melanoma: Lessons Learned from Vemurafenib (BRAFV600E-Specific Inhibitor). *Cancers*. MDPI AG June 1, 2018. https://doi.org/10.3390/cancers10060157.
(247) Zubrilov, I.; Sagi-Assif, O.; Izraely, S.; Meshel, T.; Ben-Menahem, S.; Ginat, R.; Pasmanik-Chor, M.; Nahmias, C.; Couraud, P. O.; Hoon, D. S. B.; et al. Vemurafenib Resistance

Selects for Highly Malignant Brain and Lung-Metastasizing Melanoma Cells. *Cancer Lett.* **2015**, *361* (1), 86–96. https://doi.org/10.1016/j.canlet.2015.02.041.

(248) Livingstone, E.; Zimmer, L.; Piel, S.; Schadendorf, D. PLX4032: Does It Keep Its Promise for Metastatic Melanoma Treatment? *Expert Opin. Investig. Drugs* **2010**, *19* (11), 1439–1449. https://doi.org/10.1517/13543784.2010.527945.

(249) Molnár, E.; Garay, T.; Donia, M.; Baranyi, M.; Rittler, D.; Berger, W.; Tímár, J.; Grusch, M.; Hegedűs, B. Long-Term Vemurafenib Exposure Induced Alterations of Cell Phenotypes in Melanoma: Increased Cell Migration and Its Association with EGFR Expression. *Int. J. Mol. Sci.* **2019**, *20* (18), 4484. https://doi.org/10.3390/ijms20184484.

(250) Gutzmer, R.; Stroyakovskiy, D.; Gogas, H.; Robert, C.; Lewis, K.; Protsenko, S.; Pereira, R. P.; Eigentler, T.; Rutkowski, P.; Demidov, L.; et al. Atezolizumab, Vemurafenib, and Cobimetinib as First-Line Treatment for Unresectable Advanced BRAFV600 Mutation-Positive Melanoma (IMspire150): Primary Analysis of the Randomised, Double-Blind, Placebo-Controlled, Phase 3 Trial. *Lancet* **2020**, *395* (10240), 1835–1844. https://doi.org/10.1016/S0140-6736(20)30934-X.

(251) Welsh, S. J.; Rizos, H.; Scolyer, R. A.; Long, G. V. Resistance to Combination BRAF and MEK Inhibition in Metastatic Melanoma: Where to Next? *European Journal of Cancer*. Elsevier Ltd July 1, 2016, pp 76–85. https://doi.org/10.1016/j.ejca.2016.04.005.

(252) Martin-Algarra, S.; Hinshelwood, R.; Mesnage, S.; Cebon, J.; Ferrucci, P. F.; Aglietta, M.; Neyns, B.; Chiarion-Sileni, V.; Lindsay, C. R.; Del Vecchio, M.; et al. Effectiveness of Dabrafenib in the Treatment of Patients with BRAF V600–Mutated Metastatic Melanoma in a Named Patient Program. *Melanoma Res.* **2019**, *29* (5), 527–532. https://doi.org/10.1097/CMR.0000000000000608.

(253) Trinh, V. A.; Davis, J. E.; Anderson, J. E.; Kim, K. B. Dabrafenib Therapy for Advanced Melanoma. *Annals of Pharmacotherapy*. Harvey Whitney Books Company 2014, pp 519–529. https://doi.org/10.1177/1060028013513009.

(254) Robert, C.; Grob, J. J.; Stroyakovskiy, D.; Karaszewska, B.; Hauschild, A.; Levchenko, E.; Chiarion Sileni, V.; Schachter, J.; Garbe, C.; Bondarenko, I.; et al. Five-Year Outcomes with Dabrafenib plus Trametinib in Metastatic Melanoma. *N. Engl. J. Med.* **2019**, *381* (7), 626–636. https://doi.org/10.1056/nejmoa1904059.

(255) Vultur, A.; Villanueva, J.; Herlyn, M. Targeting BRAF in Advanced Melanoma: A First Step toward Manageable Disease. *Clin. Cancer Res.* **2011**, *17* (7), 1658–1663. https://doi.org/10.1158/1078-0432.CCR-10-0174.

(256) Cox, A. D.; Der, C. J. The RAF Inhibitor Paradox Revisited. *Cancer Cell*. NIH Public Access February 14, 2012, pp 147–149. https://doi.org/10.1016/j.ccr.2012.01.017.

(257) Tanda, E. T.; Vanni, I.; Boutros, A.; Andreotti, V.; Bruno, W.; Ghiorzo, P.; Spagnolo, F. Current State of Target Treatment in BRAF Mutated Melanoma. *Front. Mol. Biosci.* **2020**, *7*, 154. https://doi.org/10.3389/fmolb.2020.00154.

(258) Chapman, P. B.; Robert, C.; Larkin, J.; Haanen, J. B.; Ribas, A.; Hogg, D.; Hamid, O.; Ascierto, P. A.; Testori, A.; Lorigan, P. C.; et al. Vemurafenib in Patients with BRAFV600 Mutation-Positive Metastatic Melanoma: Final Overall Survival Results of the Randomized BRIM-3 Study. *Ann. Oncol.* **2017**, *28* (10), 2581–2587. https://doi.org/10.1093/annonc/mdx339.

(259) GA, M.; PB, C.; C, R.; J, L.; JB, H.; R, D.; A, R.; D, H.; O, H.; PA, A.; et al. Safety and Efficacy of Vemurafenib in BRAF(V600E) and BRAF(V600K) Mutation-Positive

Melanoma (BRIM-3): Extended Follow-up of a Phase 3, Randomised, Open-Label Study. *Lancet. Oncol.* **2014**, *15* (3). https://doi.org/10.1016/S1470-2045(14)70012-9.

(260) Hauschild, A.; Grob, J. J.; Demidov, L. V.; Jouary, T.; Gutzmer, R.; Millward, M.; Rutkowski, P.; Blank, C. U.; Miller, W. H.; Kaempgen, E.; et al. Dabrafenib in BRAF-Mutated Metastatic Melanoma: A Multicentre, Open-Label, Phase 3 Randomised Controlled Trial. *Lancet* **2012**, *380* (9839), 358–365. https://doi.org/10.1016/S0140-6736(12)60868-X.

(261) Latimer, N. R.; Abrams, K. R.; Amonkar, M. M.; Stapelkamp, C.; Swann, R. S. Adjusting for the Confounding Effects of Treatment Switching—The BREAK-3 Trial: Dabrafenib Versus Dacarbazine. *Oncologist* **2015**, *20* (7), 798–805. https://doi.org/10.1634/theoncologist.2014-0429.

(262) Robert, C.; Karaszewska, B.; Schachter, J.; Rutkowski, P.; Mackiewicz, A.; Stroiakovski, D.; Lichinitser, M.; Dummer, R.; Grange, F.; Mortier, L.; et al. Improved Overall Survival in Melanoma with Combined Dabrafenib and Trametinib. *N. Engl. J. Med.* **2015**, *372* (1), 30–39. https://doi.org/10.1056/nejmoa1412690.

(263) Cobimetinib/Vemurafenib OS Benefit Sustained at 5 Years in BRAF+ Melanoma https://www.onclive.com/view/cobimetinib-vemurafenib-os-benefit-sustained-at-5-years-in-braf-positive-melanoma (accessed Mar 14, 2021).

(264) Ascierto, P. A.; Dummer, R.; Gogas, H. J.; Flaherty, K. T.; Arance, A.; Mandala, M.; Liszkay, G.; Garbe, C.; Schadendorf, D.; Krajsova, I.; et al. Update on Tolerability and Overall Survival in COLUMBUS: Landmark Analysis of a Randomised Phase 3 Trial of Encorafenib plus Binimetinib vs Vemurafenib or Encorafenib in Patients with BRAF V600–Mutant Melanoma. *Eur. J. Cancer* **2020**, *126*, 33–44. https://doi.org/10.1016/j.ejca.2019.11.016.

(265) Bischof, K.; Knappskog, S.; Hjelle, S. M.; Stefansson, I.; Woie, K.; Salvesen, H. B.; Gjertsen, B. T.; Bjorge, L. Influence of P53 Isoform Expression on Survival in High-Grade Serous Ovarian Cancers. *Sci. Rep.* **2019**, *9* (1). https://doi.org/10.1038/s41598-019-41706-z.

(266) Aasen, S. N.; Espedal, H.; Holte, C. F.; Keunen, O.; Karlsen, T. V.; Tenstad, O.; Maherally, Z.; Miletic, H.; Hoang, T.; Eikeland, A. V.; et al. Improved Drug Delivery to Brain Metastases by Peptide-Mediated Permeabilization of the Blood–Brain Barrier. *Mol. Cancer Ther.* **2019**, *18* (11), 2171–2181. https://doi.org/10.1158/1535-7163.MCT-19-0160.

(267) Mega, A.; Hartmark Nilsen, M.; Leiss, L. W.; Tobin, N. P.; Miletic, H.; Sleire, L.; Strell, C.; Nelander, S.; Krona, C.; Hägerstrand, D.; et al. Astrocytes Enhance Glioblastoma Growth. *Glia* **2020**, *68* (2), 316–327. https://doi.org/10.1002/glia.23718.

(268) Salimi-Jeda, A.; Badrzadeh, F.; Esghaei, M.; Abdoli, A. The Role of Telomerase and Viruses Interaction in Cancer Development, and Telomerase-Dependent Therapeutic Approaches. *Cancer Treatment and Research Communications*. Elsevier Ltd January 1, 2021, p 100323. https://doi.org/10.1016/j.ctarc.2021.100323.

(269) Blood-Brain Barrier hCMEC/D3 Cell Line | SCC066 https://www.merckmillipore.com/NO/en/product/Blood-Brain-Barrier-hCMEC-D3-Cell-Line,MM_NF-SCC066 (accessed Mar 19, 2021).

(270) Abounit, S.; Zurzolo, C. Wiring through Tunneling Nanotubes - from Electrical Signals to Organelle Transfer. *J. Cell Sci.* **2012**, *125* (5), 1089–1098. https://doi.org/10.1242/jcs.083279.

(271) Wittig, D.; Wang, X.; Walter, C.; Gerdes, H. H.; Funk, R. H. W.; Roehlecke, C. Multi-Level Communication of Human Retinal Pigment Epithelial Cells via Tunneling Nanotubes.

PLoS One **2012**, *7* (3). https://doi.org/10.1371/journal.pone.0033195.

(272) Sowinski, S.; Jolly, C.; Berninghausen, O.; Purbhoo, M. A.; Chauveau, A.; Köhler, K.; Oddos, S.; Eissmann, P.; Brodsky, F. M.; Hopkins, C.; et al. Membrane Nanotubes Physically Connect T Cells over Long Distances Presenting a Novel Route for HIV-1 Transmission. *Nat. Cell Biol.* **2008**, *10* (2), 211–219. https://doi.org/10.1038/ncb1682.

(273) Hase, K.; Kimura, S.; Takatsu, H.; Ohmae, M.; Kawano, S.; Kitamura, H.; Ito, M.; Watarai, H.; Hazelett, C. C.; Yeaman, C.; et al. M-Sec Promotes Membrane Nanotube Formation by Interacting with Ral and the Exocyst Complex. *Nat. Cell Biol.* **2009**, *11* (12), 1427–1432. https://doi.org/10.1038/ncb1990.

(274) Wang, X.; Veruki, M. L.; Bukoreshtliev, N. V.; Hartveit, E.; Gerdes, H. H. Animal Cells Connected by Nanotubes Can Be Electrically Coupled through Interposed Gap-Junction Channels. *Proc. Natl. Acad. Sci. U. S. A.* **2010**, *107* (40), 17194–17199. https://doi.org/10.1073/pnas.1006785107.

(275) He, K.; Luo, W.; Zhang, Y.; Liu, F.; Liu, D.; Xu, L.; Qin, L.; Xiong, C.; Lu, Z.; Fang, X.; et al. Intercellular Transportation of Quantum Dots Mediated by Membrane Nanotubes. *ACS Nano* **2010**, *4* (6), 3015–3022. https://doi.org/10.1021/nn1002198.

(276) Wang, Z. G.; Liu, S. L.; Tian, Z. Q.; Zhang, Z. L.; Tang, H. W.; Pang, D. W. Myosin-Driven Intercellular Transportation of Wheat Germ Agglutinin Mediated by Membrane Nanotubes between Human Lung Cancer Cells. *ACS Nano* **2012**, *6* (11), 10033–10041. https://doi.org/10.1021/nn303729r.

(277) Önfelt, B.; Nedvetzki, S.; Benninger, R. K. P.; Purbhoo, M. A.; Sowinski, S.; Hume, A. N.; Seabra, M. C.; Neil, M. A. A.; French, P. M. W.; Davis, D. M. Structurally Distinct Membrane Nanotubes between Human Macrophages Support Long-Distance Vesicular Traffic or Surfing of Bacteria. *J. Immunol.* **2006**, *177* (12), 8476–8483. https://doi.org/10.4049/jimmunol.177.12.8476.

(278) Abounit, S.; Delage, E.; Zurzolo, C. Identification and Characterization of Tunneling Nanotubes for Intercellular Trafficking. *Curr. Protoc. Cell Biol.* **2015**, *2015* (June), 12.10.1-12.10.21. https://doi.org/10.1002/0471143030.cb1210s67.

(279) Stone, N. L.; England, T. J.; O'Sullivan, S. E. A Novel Transwell Blood Brain Barrier Model Using Primary Human Cells. *Front. Cell. Neurosci.* **2019**, *13*, 230. https://doi.org/10.3389/fncel.2019.00230.

(280) Fibronectin Coating Protocol | Fibronectin Coating Solution | Sigma-Aldrich https://www.sigmaaldrich.com/technical-documents/articles/biofiles/fibronectin-product-protocols.html (accessed Apr 21, 2021).

(281) Bischoff, I.; Hornburger, M. C.; Mayer, B. A.; Beyerle, A.; Wegener, J.; Fürst, R. Pitfalls in Assessing Microvascular Endothelial Barrier Function: Impedance-Based Devices versus the Classic Macromolecular Tracer Assay. *Sci. Rep.* **2016**, *6* (1), 1–11. https://doi.org/10.1038/srep23671.

(282) Thomas, A.; Wang, S.; Sohrabi, S.; Orr, C.; He, R.; Shi, W.; Liu, Y. *Characterization of Vascular Permeability Using a Biomimetic Microfluidic Blood Vessel Model*.

(283) Treps, L.; Perret, R.; Edmond, S.; Ricard, D.; Gavard, J. Glioblastoma Stem-like Cells Secrete the pro-Angiogenic VEGF-A Factor in Extracellular Vesicles. *J. Extracell. Vesicles* **2017**, *6* (1), 1359479. https://doi.org/10.1080/20013078.2017.1359479.

(284) Shonka, N.; Venur, V. A.; Ahluwalia, M. S. Targeted Treatment of Brain Metastases. *Curr. Neurol. Neurosci. Rep.* **2017**, *17* (4). https://doi.org/10.1007/s11910-017-0741-2.

(285) Zakrzewski, J.; Geraghty, L. N.; Rose, A. E.; Christos, P. J.; Mazumdar, M.; Polsky, D.; Shapiro, R.; Berman, R.; Darvishian, F.; Hernando, E.; et al. Clinical Variables and Primary Tumor Characteristics Predictive of the Development of Melanoma Brain Metastases and Post-Brain Metastases Survival. *Cancer* **2011**, *117* (8), 1711–1720. https://doi.org/10.1002/cncr.25643.

(286) Tio, M.; Wang, X.; Carlino, M. S.; Shivalingam, B.; Fogarty, G. B.; Guminski, A. D.; Lo, S.; Hong, A. M.; Menzies, A. M.; Long, G. V. Survival and Prognostic Factors for Patients with Melanoma Brain Metastases in the Era of Modern Systemic Therapy. *Pigment Cell Melanoma Res.* **2018**, *31* (4), 509–515. https://doi.org/10.1111/pcmr.12682.

(287) Lowery, F. J.; Yu, D. Brain Metastasis: Unique Challenges and Open Opportunities. *Biochimica et Biophysica Acta - Reviews on Cancer*. Elsevier B.V. January 1, 2017, pp 49–57. https://doi.org/10.1016/j.bbcan.2016.12.001.

(288) Kim, M.; Kizilbash, S. H.; Laramy, J. K.; Gampa, G.; Parrish, K. E.; Sarkaria, J. N.; Elmquist, W. F. Barriers to Effective Drug Treatment for Brain Metastases: A Multifactorial Problem in the Delivery of Precision Medicine. *Pharmaceutical Research*. Springer New York LLC September 1, 2018, p 177. https://doi.org/10.1007/s11095-018-2455-9.

(289) Schulz, M.; Salamero-Boix, A.; Niesel, K.; Alekseeva, T.; Sevenich, L. Microenvironmental Regulation of Tumor Progression and Therapeutic Response in Brain Metastasis. *Frontiers in immunology*. NLM (Medline) 2019, p 1713. https://doi.org/10.3389/fimmu.2019.01713.

(290) Franchino, F.; Rudà, R.; Soffietti, R. Mechanisms and Therapy for Cancer Metastasis to the Brain. *Frontiers in Oncology*. Frontiers Media S.A. May 24, 2018, p 1. https://doi.org/10.3389/fonc.2018.00161.

(291) Becco, P.; Gallo, S.; Poletto, S.; Frascione, M. P. M.; Crotto, L.; Zaccagna, A.; Paruzzo, L.; Caravelli, D.; Carnevale-Schianca, F.; Aglietta, M. Melanoma Brain Metastases in the Era of Target Therapies: An Overview. *Cancers*. MDPI AG June 1, 2020, pp 1–20. https://doi.org/10.3390/cancers12061640.

(292) Busam, K. J.; Charles, C.; Lee, G.; Halpern, A. C. Morphologic Features of Melanocytes, Pigmented Keratinocytes, and Melanophages by in Vivo Confocal Scanning Laser Microscopy. *Mod. Pathol.* **2001**, *14* (9), 862–868. https://doi.org/10.1038/modpathol.3880402.

(293) Schiweck, J.; Eickholt, B. J.; Murk, K. Important Shapeshifter: Mechanisms Allowing Astrocytes to Respond to the Changing Nervous System during Development, Injury and Disease. *Frontiers in Cellular Neuroscience*. Frontiers Media S.A. August 21, 2018. https://doi.org/10.3389/fncel.2018.00261.

(294) Schousboe, A.; Divac, I. Differences in Glutamate Uptake in Astrocytes Cultured from Different Brain Regions. *Brain Res.* **1979**, *177* (2), 407–409. https://doi.org/10.1016/0006-8993(79)90795-9.

(295) Westergaard, N.; Sonnewald, U.; Unsgård, G.; Peng, L.; Hertz, L.; Schousboe, A. Uptake, Release, and Metabolism of Citrate in Neurons and Astrocytes in Primary Cultures. *J. Neurochem.* **1994**, *62* (5), 1727–1733. https://doi.org/10.1046/j.1471-4159.1994.62051727.x.

(296) Lange, S. C.; Bak, L. K.; Waagepetersen, H. S.; Schousboe, A.; Norenberg, M. D. Primary Cultures of Astrocytes: Their Value in Understanding Astrocytes in Health and Disease. *Neurochemical Research*. NIH Public Access November 2012, pp 2569–2588. https://doi.org/10.1007/s11064-012-0868-0.

(297) Llombart, V.; García-Berrocoso, T.; Bech-Serra, J. J.; Simats, A.; Bustamante, A.; Giralt, D.; Reverter-Branchat, G.; Canals, F.; Hernández-Guillamon, M.; Montaner, J. Characterization of Secretomes from a Human Blood Brain Barrier Endothelial Cells In-Vitro Model after Ischemia by Stable Isotope Labeling with Aminoacids in Cell Culture (SILAC). *J. Proteomics* **2016**, *133*, 100–112. https://doi.org/10.1016/j.jprot.2015.12.011.

(298) Maggioli, E.; McArthur, S.; Mauro, C.; Kieswich, J.; Kusters, D. H. M.; Reutelingsperger, C. P. M.; Yaqoob, M.; Solito, E. Estrogen Protects the Blood–Brain Barrier from Inflammation-Induced Disruption and Increased Lymphocyte Trafficking. *Brain. Behav. Immun.* **2016**, *51*, 212–222. https://doi.org/10.1016/j.bbi.2015.08.020.

(299) Weksler, B.; Romero, I. A.; Couraud, P. O. The HCMEC/D3 Cell Line as a Model of the Human Blood Brain Barrier. *Fluids and Barriers of the CNS*. BioMed Central March 26, 2013, p 16. https://doi.org/10.1186/2045-8118-10-16.

(300) Zhang, L.; Zhang, Y. Tunneling Nanotubes between Rat Primary Astrocytes and C6 Glioma Cells Alter Proliferation Potential of Glioma Cells. *Neurosci Bull* **2015**, *31* (3), 371–378. https://doi.org/10.1007/s12264-014-1522-4.

(301) Yang, N.; Yan, T.; Zhu, H.; Liang, X.; Leiss, L.; Sakariassen, P. Ø.; Skaftnesmo, K. O.; Huang, B.; Costea, D. E.; Enger, P. Ø.; et al. A Co-Culture Model with Brain Tumor-Specific Bioluminescence Demonstrates Astrocyte-Induced Drug Resistance in Glioblastoma. *J. Transl. Med.* **2014**, *12* (1), 1–9. https://doi.org/10.1186/s12967-014-0278-y.

(302) Errede, M.; Mangieri, D.; Longo, G.; Girolamo, F.; De Trizio, I.; Vimercati, A.; Serio, G.; Frei, K.; Perris, R.; Virgintino, D. Tunneling Nanotubes Evoke Pericyte/Endothelial Communication during Normal and Tumoral Angiogenesis. *Fluids Barriers CNS* **2018**, *15* (1). https://doi.org/10.1186/s12987-018-0114-5.

(303) Weng, Z.; Zhang, B.; Tsilioni, I.; Theoharides, T. C. Nanotube Formation: A Rapid Form of "Alarm Signaling"? *Clin. Ther.* **2016**, *38* (5), 1066–1072. https://doi.org/10.1016/j.clinthera.2016.02.030.

(304) Civita, P.; Leite, D. M.; Pilkington, G. J. Pre-Clinical Drug Testing in 2D and 3D Human In Vitro Models of Glioblastoma Incorporating Non-Neoplastic Astrocytes: Tunneling Nano Tubules and Mitochondrial Transfer Modulates Cell Behavior and Therapeutic Respons. **2019**. https://doi.org/10.3390/ijms20236017.

(305) Cselenyák, A.; Pankotai, E.; Horváth, E. M.; Kiss, L.; Lacza, Z. Mesenchymal Stem Cells Rescue Cardiomyoblasts from Cell Death in an in Vitro Ischemia Model via Direct Cell-to-Cell Connections. *BMC Cell Biol.* **2010**, *11*, 29. https://doi.org/10.1186/1471-2121-11-29.

(306) Kolba, M. D.; Dudka, W.; Zaręba-Kozioł, M.; Kominek, A.; Ronchi, P.; Turos, L.; Chroscicki, P.; Wlodarczyk, J.; Schwab, Y.; Klejman, A.; et al. Tunneling Nanotube-Mediated Intercellular Vesicle and Protein Transfer in the Stroma-Provided Imatinib Resistance in Chronic Myeloid Leukemia Cells. *Cell Death Dis.* **2019**, *10* (11), 1–16. https://doi.org/10.1038/s41419-019-2045-8.

(307) Liu, K.; Ji, K.; Guo, L.; Wu, W.; Lu, H.; Shan, P.; Yan, C. Mesenchymal Stem Cells Rescue Injured Endothelial Cells in an in Vitro Ischemia-Reperfusion Model via Tunneling Nanotube like Structure-Mediated Mitochondrial Transfer. *Microvasc. Res.* **2014**, *92*, 10–18. https://doi.org/10.1016/j.mvr.2014.01.008.

(308) Thayanithy, V.; Dickson, E. L.; Steer, C.; Subramanian, S.; Lou, E. Tumor-Stromal Cross Talk: Direct Cell-to-Cell Transfer of Oncogenic MicroRNAs via Tunneling Nanotubes. *Transl. Res.* **2014**, *164* (5), 359–365. https://doi.org/10.1016/j.trsl.2014.05.011.

(309) Xu, W.; Santini, P. A.; Sullivan, J. S.; He, B.; Shan, M.; Ball, S. C.; Dyer, W. B.; Ketas, T. J.; Chadburn, A.; Cohen-Gould, L.; et al. HIV-1 Evades Virus-Specific IgG2 and IgA Responses by Targeting Systemic and Intestinal B Cells via Long-Range Intercellular Conduits. *Nat. Immunol.* **2009**, *10* (9), 1008–1017. https://doi.org/10.1038/ni.1753.

(310) Campana, S.; De Pasquale, C.; Carrega, P.; Ferlazzo, G.; Bonaccorsi, I. Cross-Dressing: An Alternative Mechanism for Antigen Presentation. *Immunology Letters*. Elsevier B.V. December 1, 2015, pp 349–354. https://doi.org/10.1016/j.imlet.2015.11.002.

(311) Naphade, S.; Sharma, J.; Gaide Chevronnay, H. P.; Shook, M. A.; Yeagy, B. A.; Rocca, C. J.; Ur, S. N.; Lau, A. J.; Courtoy, P. J.; Cherqui, S. Brief Reports: Lysosomal Cross-Correction by Hematopoietic Stem Cell-Derived Macrophages via Tunneling Nanotubes. *Stem Cells* **2015**, *33* (1), 301–309. https://doi.org/10.1002/stem.1835.

(312) Jackson, M. V.; Morrison, T. J.; Doherty, D. F.; McAuley, D. F.; Matthay, M. A.; Kissenpfennig, A.; O'Kane, C. M.; Krasnodembskaya, A. D. Mitochondrial Transfer via Tunneling Nanotubes Is an Important Mechanism by Which Mesenchymal Stem Cells Enhance Macrophage Phagocytosis in the In Vitro and In Vivo Models of ARDS. *Stem Cells* **2016**, *34* (8), 2210–2223. https://doi.org/10.1002/stem.2372.

(313) Staufer, O.; Hernandez B., J. E.; Rustom, A. Protease-Resistant Cell Meshworks: An Indication of Membrane Nanotube-Based Syncytia Formation. *Exp. Cell Res.* **2018**, *372* (2), 85–91. https://doi.org/10.1016/j.yexcr.2018.09.012.

(314) Hsiung, F.; Ramirez-Weber, F. A.; David Iwaki, D.; Kornberg, T. B. Dependence of Drosophila Wing Imaginal Disc Cytonemes on Decapentaplegic. *Nature* **2005**, *437* (7058), 560–563. https://doi.org/10.1038/nature03951.

(315) Beum, P. V.; Lindorfer, M. A.; Peek, E. M.; Stukenberg, P. T.; de Weers, M.; Beurskens, F. J.; Parren, P. W. H. I.; van de Winkel, J. G. J.; Taylor, R. P. Penetration of Antibody-Opsonized Cells by the Membrane Attack Complex of Complement Promotes Ca2+ Influx and Induces Streamers. *Eur. J. Immunol.* **2011**, *41* (8), 2436–2446. https://doi.org/10.1002/eji.201041204.

(316) Lin, C. I.; Merley, A.; Sciuto, T. E.; Li, D.; Dvorak, A. M.; Melero-Martin, J. M.; Dvorak, H. F.; Jaminet, S. C. S. TM4SF1: A New Vascular Therapeutic Target in Cancer. *Angiogenesis* **2014**, *17* (4), 897–907. https://doi.org/10.1007/s10456-014-9437-2.

(317) Okafo, G.; Prevedel, L.; Eugenin, E. Tunneling Nanotubes (TNT) Mediate Long-Range Gap Junctional Communication: Implications for HIV Cell to Cell Spread. *Sci. Rep.* **2017**, *7* (1). https://doi.org/10.1038/s41598-017-16600-1.

(318) Sartori-Rupp, A.; Cordero Cervantes, D.; Pepe, A.; Delage, E.; Gousset, K.; Corroyer-Dulmont, S.; Schmitt, C.; Krijnse-Locker, J.; Zurzolo, C. Mapping of TNTs Using Correlative Cryo-Electron Microscopy Reveals a Novel Structure. https://doi.org/10.1101/342469.

(319) Korenkova, O.; Pepe, A.; Zurzolo, C. Fine Intercellular Connections in Development: TNTs, Cytonemes, or Intercellular Bridges? *Cell Stress*. Shared Science Publishers OG February 1, 2020, pp 30–43. https://doi.org/10.15698/cst2020.02.212.

(320) Schiller, C.; Diakopoulos, K. N.; Rohwedder, I.; Kremmer, E.; Toerne, C. von; Ueffing, M.; Weidle, U. H.; Ohno, H.; Weiss, E. H. LST1 Promotes the Assembly of a Molecular Machinery Responsible for Tunneling Nanotube Formation. *J. Cell Sci.* **2013**, *126* (3), 767–777. https://doi.org/10.1242/jcs.114033.

(321) Connor, Y.; Tekleab, S.; Nandakumar, S.; Walls, C.; Tekleab, Y.; Husain, A.; Gadish, O.;

Sabbisetti, V.; Kaushik, S.; Sehrawat, S.; et al. Physical Nanoscale Conduit-Mediated Communication between Tumour Cells and the Endothelium Modulates Endothelial Phenotype. *Nat. Commun.* **2015**, *6* (1), 1–14. https://doi.org/10.1038/ncomms9671.

(322) Pinto, G.; Brou, C.; Zurzolo, C. Tunneling Nanotubes: The Fuel of Tumor Progression? *Trends in Cancer*. Cell Press October 1, 2020, pp 874–888. https://doi.org/10.1016/j.trecan.2020.04.012.

(323) Thayanithy, V.; Dickson, E. L.; Steer, C.; Subramanian, S.; Lou, E. Tumor-Stromal Cross Talk: Direct Cell-to-Cell Transfer of Oncogenic MicroRNAs via Tunneling Nanotubes. *Transl. Res.* **2014**, *164* (5), 359–365. https://doi.org/10.1016/j.trsl.2014.05.011.

(324) Osswald, M.; Jung, E.; Sahm, F.; Solecki, G.; Venkataramani, V.; Blaes, J.; Weil, S.; Horstmann, H.; Wiestler, B.; Syed, M.; et al. Brain Tumour Cells Interconnect to a Functional and Resistant Network. *Nature* **2015**, *528* (7580), 93–98. https://doi.org/10.1038/nature16071.

(325) Ady, J. W.; Desir, S.; Thayanithy, V.; Vogel, R. I.; Moreira, A. L.; Downey, R. J.; Fong, Y.; Manova-Todorova, K.; Moore, M. A. S.; Lou, E. Intercellular Communication in Malignant Pleural Mesothelioma: Properties of Tunneling Nanotubes. *Front. Physiol.* **2014**, *5*, 400. https://doi.org/10.3389/fphys.2014.00400.

(326) Lu, J. J.; Yang, W. M.; Li, F.; Zhu, W.; Chen, Z. Tunneling Nanotubes Mediated MicroRNA-155 Intercellular Transportation Promotes Bladder Cancer Cells' Invasive and Proliferative Capacity. *Int. J. Nanomedicine* **2019**, *14*, 9731–9743. https://doi.org/10.2147/IJN.S217277.

(327) Hanna, S. J.; McCoy-Simandle, K.; Leung, E.; Genna, A.; Condeelis, J.; Cox, D. Tunneling Nanotubes, a Novel Mode of Tumor Cell-Macrophage Communication in Tumor Cell Invasion. *J. Cell Sci.* **2019**, *132* (3). https://doi.org/10.1242/jcs.223321.

(328) Pasquier, J.; Guerrouahen, B. S.; Al Thawadi, H.; Ghiabi, P.; Maleki, M.; Abu-Kaoud, N.; Jacob, A.; Mirshahi, M.; Galas, L.; Rafii, S.; et al. Preferential Transfer of Mitochondria from Endothelial to Cancer Cells through Tunneling Nanotubes Modulates Chemoresistance. *J. Transl. Med.* **2013**, *11* (1), 1–14. https://doi.org/10.1186/1479-5876-11-94.

(329) Zhang, L.; Zhang, Y. Tunneling Nanotubes between Rat Primary Astrocytes and C6 Glioma Cells Alter Proliferation Potential of Glioma Cells. *Neurosci. Bull.* **2015**, *31* (3), 371–378. https://doi.org/10.1007/s12264-014-1522-4.

(330) Wang, Y.; Cui, J.; Sun, X.; Zhang, Y. Tunneling-Nanotube Development in Astrocytes Depends on P53 Activation. *Cell Death Differ.* **2011**, *18* (4), 732–742. https://doi.org/10.1038/cdd.2010.147.

(331) Thayanithy, V.; Babatunde, V.; Dickson, E. L.; Wong, P.; Oh, S.; Ke, X.; Barlas, A.; Fujisawa, S.; Romin, Y.; Moreira, A. L.; et al. Tumor Exosomes Induce Tunneling Nanotubes in Lipid Raft-Enriched Regions of Human Mesothelioma Cells. *Exp. Cell Res.* **2014**, *323* (1), 178–188. https://doi.org/10.1016/j.yexcr.2014.01.014.

(332) Polak, R.; De Rooij, B.; Pieters, R.; Den Boer, M. L. B-Cell Precursor Acute Lymphoblastic Leukemia Cells Use Tunneling Nanotubes to Orchestrate Their Microenvironment. *Blood* **2015**, *126* (21), 2404–2414. https://doi.org/10.1182/blood-2015-03-634238.

(333) Hodneland, E.; Lundervold, A.; Gurke, S.; Tai, X. C.; Rustom, A.; Gerdes, H. H. Automated Detection of Tunneling Nanotubes in 3D Images. *Cytom. Part A* **2006**, *69* (9), 961–972. https://doi.org/10.1002/cyto.a.20302.

(334) Zoetemelk, M.; Ramzy, G. M.; Rausch, M.; Koessler, T.; van Beijnum, J. R.; Weiss, A.; Mieville, V.; Piersma, S. R.; de Haas, R. R.; Delucinge-Vivier, C.; et al. Optimized Low-Dose Combinatorial Drug Treatment Boosts Selectivity and Efficacy of Colorectal Carcinoma Treatment. *Mol. Oncol.* **2020**, *14* (11), 2894–2919. https://doi.org/10.1002/1878-0261.12797.

(335) Molina-Cerrillo, J.; San Román, M.; Pozas, J.; Alonso-Gordoa, T.; Pozas, M.; Conde, E.; Rosas, M.; Grande, E.; García-Bermejo, M. L.; Carrato, A. Braf Mutated Colorectal Cancer: New Treatment Approaches. *Cancers*. MDPI AG June 1, 2020, pp 1–15. https://doi.org/10.3390/cancers12061571.

(336) Weil, S.; Osswald, M.; Solecki, G.; Grosch, J.; Jung, E.; Lemke, D.; Ratliff, M.; Hänggi, D.; Wick, W.; Winkler, F. Tumor Microtubes Convey Resistance to Surgical Lesions and Chemotherapy in Gliomas. *Neuro. Oncol.* **2017**, *19* (10), 1316–1326. https://doi.org/10.1093/neuonc/nox070.

(337) Filippova, N.; Nabors, L. B. Elavl1 Role in Cell Fusion and Tunneling Membrane Nanotube Formations with Implication to Treat Glioma Heterogeneity. *Cancers*. MDPI AG October 1, 2020, pp 1–18. https://doi.org/10.3390/cancers12103069.

(338) Brandhagen, B. A. N.; Tieszen, C. R.; Ulmer, T. M.; Tracy, M. S.; Goyeneche, A. A.; Telleria, C. M. Cytostasis and Morphological Changes Induced by Mifepristone in Human Metastatic Cancer Cells Involve Cytoskeletal Filamentous Actin Reorganization and Impairment of Cell Adhesion Dynamics. *BMC Cancer* **2013**, *13* (1), 1–15. https://doi.org/10.1186/1471-2407-13-35.

(339) Domura, R.; Sasaki, R.; Ishikawa, Y.; Okamoto, M. Cellular Morphology-Mediated Proliferation and Drug Sensitivity of Breast Cancer Cells. *J. Funct. Biomater.* **2017**, *8* (2), 18. https://doi.org/10.3390/jfb8020018.

(340) Tarhan, Y. E.; Kato, T.; Jang, M.; Haga, Y.; Ueda, K.; Nakamura, Y.; Park, J. H. Morphological Changes, Cadherin Switching, and Growth Suppression in Pancreatic Cancer by GALNT6 Knockdown. *Neoplasia (United States)* **2016**, *18* (5), 265–272. https://doi.org/10.1016/j.neo.2016.03.005.

(341) Mgbonyebi, O. P.; Russo, J.; Russo, I. H. *Roscovitine Induces Cell Death and Morphological Changes Indicative of Apoptosis in MDA-MB-231 Breast Cancer Cells 1*; 1903; Vol. 59.

(342) Dratkiewicz, E.; Simiczyjew, A.; Pietraszek-Gremplewicz, K.; Mazurkiewicz, J.; Nowak, D. Characterization of Melanoma Cell Lines Resistant to Vemurafenib and Evaluation of Their Responsiveness to EGFR-and MET-Inhibitor Treatment. *Int. J. Mol. Sci. Artic.* **2019**. https://doi.org/10.3390/ijms21010113.

(343) Tabolacci, C.; Cordella, M.; Mariotti, S.; Rossi, S.; Senatore, C.; Lintas, C.; Levati, L.; D'arcangelo, D.; Facchiano, A.; D'atri, S.; et al. Melanoma Cell Resistance to Vemurafenib Modifies Inter-Cellular Communication Signals. *Biomedicines* **2021**, *9* (1), 1–19. https://doi.org/10.3390/biomedicines9010079.

(344) Saei, A.; Eichhorn, P. J. A. Ubiquitination and Adaptive Responses to BRAF Inhibitors in Melanoma. *Molecular and Cellular Oncology*. Taylor and Francis Ltd. September 3, 2018. https://doi.org/10.1080/23723556.2018.1497862.

(345) Fallahi-Sichani, M.; Becker, V.; Izar, B.; Baker, G. J.; Lin, J.; Boswell, S. A.; Shah, P.; Rotem, A.; Garraway, L. A.; Sorger, P. K. Adaptive Resistance of Melanoma Cells to RAF Inhibition via Reversible Induction of a Slowly Dividing De-differentiated State . *Mol. Syst. Biol.* **2017**, *13* (1), 905. https://doi.org/10.15252/msb.20166796.

(346) Titz, B.; Lomova, A.; Le, A.; Hugo, W.; Kong, X.; Ten Hoeve, J.; Friedman, M.; Shi, H.; Moriceau, G.; Song, C.; et al. JUN Dependency in Distinct Early and Late BRAF Inhibition Adaptation States of Melanoma. *Cell Discov.* **2016**, *2* (1), 1–19. https://doi.org/10.1038/celldisc.2016.28.

(347) Frick, P. L.; Paudel, B. B.; Tyson, D. R.; Quaranta, V. Quantifying Heterogeneity and Dynamics of Clonal Fitness in Response to Perturbation. *J. Cell. Physiol.* **2015**, *230* (7), 1403–1412. https://doi.org/10.1002/jcp.24888.

(348) Hata, A. N.; Niederst, M. J.; Archibald, H. L.; Gomez-Caraballo, M.; Siddiqui, F. M.; Mulvey, H. E.; Maruvka, Y. E.; Ji, F.; Bhang, H. E. C.; Radhakrishna, V. K.; et al. Tumor Cells Can Follow Distinct Evolutionary Paths to Become Resistant to Epidermal Growth Factor Receptor Inhibition. *Nat. Med.* **2016**, *22* (3), 262–269. https://doi.org/10.1038/nm.4040.

(349) Sahu, P.; Jena, S. R.; Samanta, L. Tunneling Nanotubes: A Versatile Target for Cancer Therapy. *Curr. Cancer Drug Targets* **2018**, *18* (6), 514–521. https://doi.org/10.2174/1568009618666171129222637.

(350) Fletcher, N. F.; Brayden, D. J.; Brankin, B.; Worrall, S.; Callanan, J. J. Growth and Characterisation of a Cell Culture Model of the Feline Blood-Brain Barrier. *Vet. Immunol. Immunopathol.* **2006**, *109* (3–4), 233–244. https://doi.org/10.1016/j.vetimm.2005.08.025.

(351) Kuo, Y. C.; Lu, C. H. Effect of Human Astrocytes on the Characteristics of Human Brain-Microvascular Endothelial Cells in the Blood-Brain Barrier. *Colloids Surfaces B Biointerfaces* **2011**, *86* (1), 225–231. https://doi.org/10.1016/j.colsurfb.2011.04.005.

(352) Bagchi, S.; Chhibber, T.; Lahooti, B.; Verma, A.; Borse, V.; Jayant, R. D. In-Vitro Blood-Brain Barrier Models for Drug Screening and Permeation Studies: An Overview. *Drug Design, Development and Therapy*. Dove Medical Press Ltd. October 18, 2019, pp 3591–3605. https://doi.org/10.2147/DDDT.S218708.

(353) Naik, P.; Cucullo, L. In Vitro Blood-Brain Barrier Models: Current and Perspective Technologies. *Journal of Pharmaceutical Sciences*. John Wiley and Sons Inc. 2012, pp 1337–1354. https://doi.org/10.1002/jps.23022.

(354) Hatherell, K.; Couraud, P. O.; Romero, I. A.; Weksler, B.; Pilkington, G. J. Development of a Three-Dimensional, All-Human in Vitro Model of the Blood-Brain Barrier Using Mono-, Co-, and Tri-Cultivation Transwell Models. *J. Neurosci. Methods* **2011**, *199* (2), 223–229. https://doi.org/10.1016/j.jneumeth.2011.05.012.

(355) Cecchelli, R.; Dehouck, B.; Descamps, L.; Fenart, L.; Buée-Scherrer, V.; Duhem, C.; Lundquist, S.; Rentfel, M.; Torpier, G.; Dehouck, M. P. In Vitro Model for Evaluating Drug Transport across the Blood-Brain Barrier. *Advanced Drug Delivery Reviews*. Elsevier Science Publishers B.V. April 5, 1999, pp 165–178. https://doi.org/10.1016/S0169-409X(98)00083-0.

(356) Gaillard, P. J.; Voorwinden, L. H.; Nielsen, J. L.; Ivanov, A.; Atsumi, R.; Engman, H.; Ringbom, C.; De Boer, A. G.; Breimer, D. D. Establishment and Functional Characterization of an in Vitro Model of the Blood-Brain Barrier, Comprising a Co-Culture of Brain Capillary Endothelial Cells and Astrocytes. *Eur. J. Pharm. Sci.* **2001**, *12* (3), 215–222. https://doi.org/10.1016/S0928-0987(00)00123-8.

(357) Abbott, N. J.; Dolman, D. E. M.; Drndarski, S.; Fredriksson, S. M. An Improved in Vitro Blood-Brain Barrier Model: Rat Brain Endothelial Cells Co-Cultured with Astrocytes. *Methods Mol. Biol.* **2012**, *814*, 415–430. https://doi.org/10.1007/978-1-61779-452-0_28.

(358) Malina, K. C. K.; Cooper, I.; Teichberg, V. I. Closing the Gap between the In-Vivo and in-Vitro Blood-Brain Barrier Tightness. *Brain Res.* **2009**, *1284*, 12–21. https://doi.org/10.1016/j.brainres.2009.05.072.

(359) Dohgu, S.; Takata, F.; Yamauchi, A.; Nakagawa, S.; Egawa, T.; Naito, M.; Tsuruo, T.; Sawada, Y.; Niwa, M.; Kataoka, Y. Brain Pericytes Contribute to the Induction and Up-Regulation of Blood-Brain Barrier Functions through Transforming Growth Factor-β Production. *Brain Res.* **2005**, *1038* (2), 208–215. https://doi.org/10.1016/j.brainres.2005.01.027.

(360) Nakagawa, S.; Deli, M. A.; Kawaguchi, H.; Shimizudani, T.; Shimono, T.; Kittel, Á.; Tanaka, K.; Niwa, M. A New Blood-Brain Barrier Model Using Primary Rat Brain Endothelial Cells, Pericytes and Astrocytes. *Neurochem. Int.* **2009**, *54* (3–4), 253–263. https://doi.org/10.1016/j.neuint.2008.12.002.

(361) Natarajan, R.; Northrop, N.; Yamamoto, B. Fluorescein Isothiocyanate (FITC)-Dextran Extravasation as a Measure of Blood-Brain Barrier Permeability. *Curr. Protoc. Neurosci.* **2017**, *2017*, 9.58.1-9.58.15. https://doi.org/10.1002/cpns.25.

(362) Fu, B. M.; Zhao, Z.; Zhu, D. Blood-Brain Barrier (BBB) Permeability and Transport Measurement In Vitro and In Vivo; 2020. https://doi.org/10.1007/7651_2020_308.

(363) Czupalla, C. J.; Liebner, S.; Devraj, K. In Vitro Models of the Blood–Brain Barrier; 2014; pp 415–437. https://doi.org/10.1007/978-1-4939-0320-7_34.

(364) Tornavaca, O.; Chia, M.; Dufton, N.; Almagro, L. O.; Conway, D. E.; Randi, A. M.; Schwartz, M. A.; Matter, K.; Balda, M. S. ZO-1 Controls Endothelial Adherens Junctions, Cell-Cell Tension, Angiogenesis, and Barrier Formation. *J. Cell Biol.* **2015**, *208* (6), 821–838. https://doi.org/10.1083/jcb.201404140.

(365) Mossu, A.; Rosito, M.; Khire, T.; Li Chung, H.; Nishihara, H.; Gruber, I.; Luke, E.; Dehouck, L.; Sallusto, F.; Gosselet, F.; et al. A Silicon Nanomembrane Platform for the Visualization of Immune Cell Trafficking across the Human Blood–Brain Barrier under Flow. *J. Cereb. Blood Flow Metab.* **2019**, *39* (3), 395–410. https://doi.org/10.1177/0271678X18820584.

(366) Cheng, Q.; Wu, J.; Zhang, Y.; Liu, X.; Xu, N.; Zuo, F.; Xu, J. SOX4 Promotes Melanoma Cell Migration and Invasion Though the Activation of the NF-KB Signaling Pathway. *Int. J. Mol. Med.* **2017**, *40* (2), 447–453. https://doi.org/10.3892/ijmm.2017.3030.

(367) Jia, W.; Lu, R.; Martin, T. A.; Jiang, W. G. The Role of Claudin-5 in Blood-Brain Barrier (BBB) and Brain Metastases (Review). *Mol. Med. Rep.* **2014**, *9* (3), 779–785. https://doi.org/10.3892/mmr.2013.1875.

(368) Rizzo, A.; Vasco, C.; Girgenti, V.; Fugnanesi, V.; Calatozzolo, C.; Canazza, A.; Salmaggi, A.; Rivoltini, L.; Morbin, M.; Ciusani, E. Melanoma Cells Homing to the Brain: An in Vitro Model. *Biomed Res. Int.* **2015**, *2015*. https://doi.org/10.1155/2015/476069.